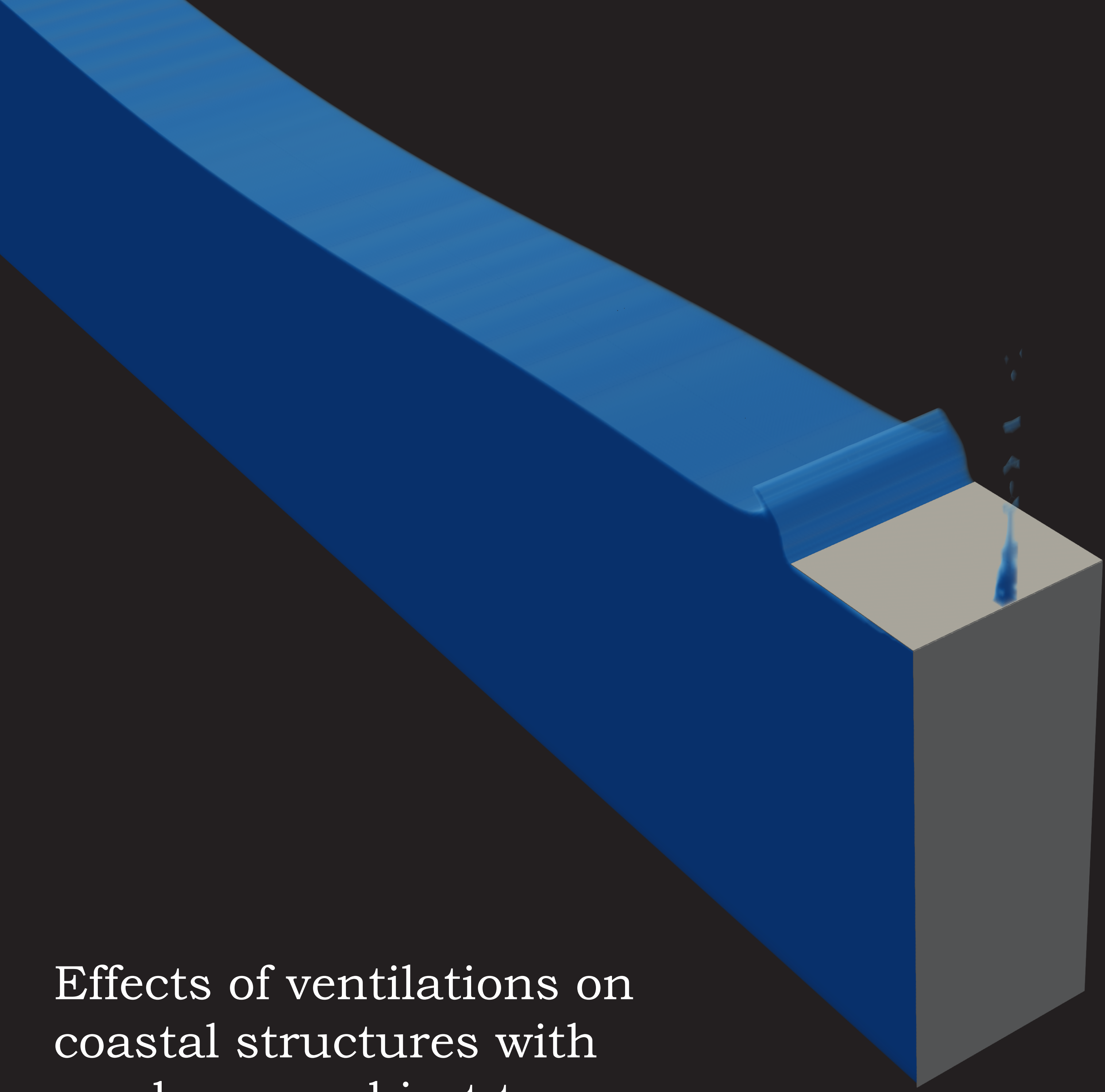

Effects of ventilations on coastal structures with overhangs subject to wave impacts

CoMEM Master Thesis

Marlon Vieira Passos

Effects of ventilations on coastal structures with overhangs subject to wave impacts

CoMEM Master Thesis

by

Marlon Vieira Passos

As a requirement to attend the degree of

Erasmus+: Erasmus Mundus Master in Coastal and Marine Engineering and Management (CoMEM)

CoMEM

Erasmus+: Erasmus Mundus Mobility Programme

Taught at the following educational institutions:

Norges Teknisk- Naturvitenskapelige Universitet (NTNU)
Trondheim, Norway

Technische Universiteit Delft (TU Delft)
Delft, The Netherlands

University of Southampton
Southampton, United Kingdom

At which the student has studied from August 2017 to July 2019

to be defended publicly on Tuesday July 18, 2019 at 11:30 AM
at the Delft University of Technology

Under supervision of:	Prof. dr. ir. W. S. J. Uijttewaal,	TU Delft
	Dr. ir. B. Hofland,	TU Delft
	Ir. E. de Almeida (daily supervisor),	TU Delft

TU Delft Delft University of Technology

Erasmus+ UNIVERSITAT POLITÈCNICA DE CATALUNYA BARCELONATECH NTNU Norwegian University of Science and Technology UNIVERSITY OF Southampton CITY UNIVERSITY OF LONDON EST 1894

The Erasmus+: Erasmus Mundus MSc in Coastal and Marine Engineering and Management is an integrated programme including mobility organized by five European partner institutions, coordinated by Norwegian University of Science and Technology (NTNU).

The joint study programme of 120 ECTS credits (two years full-time) has been obtained at two or three of the five CoMEM partner institutions:

- Norges Teknisk- Naturvitenskapelige Universitet (NTNU) Trondheim, Norway
- Technische Universiteit (TU) Delft, The Netherlands
- Universitat Politècnica de Catalunya (UPC). BarcelonaTech. Barcelona, Spain
- University of Southampton, Southampton, Great Britain
- City University London, London, Great Britain

During the first three semesters of the programme, students study at two or three different universities depending on their track of study. In the fourth and final semester an MSc project and thesis has to be completed. The two-year CoMEM programme leads to a multiple set of officially recognized MSc diploma certificates. These will be issued by the universities that have been attended by the student. The transcripts issued with the MSc Diploma Certificate of each university include grades/marks and credits for each subject.

Information regarding the CoMEM programme can be obtained from the programme coordinator:

Øivind A. Arntsen, Dr.ing.
Associate professor in Marine Civil Engineering
Department of Civil and Environmental Engineering
NTNU Norway
Mob.: +4792650455 Fax: + 4773597021
Email: oivind.arntsen@ntnu.no

CoMEM URL: https://www.ntnu.edu/studies/mscomem

Preface

The completion of this master thesis meets the final requirement for earning the Master of Science in Coastal and Marine Engineering and Management (CoMEM), in the track of Coastal Engineering. The 2-year academic program was conducted at Delft University of Technology, the Norwegian University of Science and Technology and the University of Southampton. For the entire period of study, tuition and living costs were covered by an Erasmus Mundus scholarship. This thesis is involved with the project Dynamics of Hydraulic Structures (DynaHicS) funded by the Netherlands Organisation for Scientific Research (NWO) and includes numerical modelling performed on high performance computing clusters provided by TU Delft.

I would like to express my deep gratitude to Ermano de Almeida, Bas Hofland and Wim Uijttewaal for being part of my thesis committee and providing valuable advice and insights on theoretical and practical aspects of the work, throughout several meetings along the last 5 months.

My special thanks to Ermano de Almeida for trusting me with this thesis topic, so unique and relevant in the field of coastal engineering. His continuous intense support was crucial to establish research objectives, plan and implement the methodologies which form the core of this study.

I am particularly grateful to Bas Hofland, who offered precious MATLAB codes and always dedicated time to provide constructive feedback and patiently answer my doubts during the development of this thesis. Thanks to his initiative and effort, part of this study has been sent for publication at the Coastal Structures Conference 2019.

I would also like to express my appreciation towards Øivind Arntsen, Sonja Hammer, Robert Nicholls and Madelon Burgmeijer for organizing the CoMEM program and providing guidance whenever needed.

Finally, I wish to thank my fiancée Sharon, my family and friends for all support and encouragement during the development of this thesis.

Marlon Vieira Passos
Delft, July 2019

Summary

Coastal structures with horizontal overhangs are built due to design constraints, but wave loadings substantially increase under these confined geometries. Vertical structure elements, such as steel gates, are vulnerable to damage caused by impulsive wave impacts, potentially exposing the coastal zone to flooding and erosion. Existing formulas to determine impulsive loadings in engineering practice are limited to purely vertical structures. Research has shown that openings along the surface of structures relieve wave impact pressures, but there are currently no design methods available to quantify this pressure release. The stochastic nature of impulsive impacts and uncertain influence of air adds to the problem complexity. This study aims to investigate the influence of ventilations to reduce wave impact loadings on vertical structures with horizontal overhangs, applying a theoretical pressure-impulse approach and computational fluid dynamics.

Laboratory scale experiments were conducted by de Almeida et al. (2019) to evaluate impulsive impacts from non-breaking standing waves on vertical structures with overhangs. Measurements indicate that impulsive loadings are associated with the water flow deflection during impacts caused by the exposed horizontal surface. Moreover, longer overhangs lead to higher impact pressures under the same wave conditions.

To examine wave impacts beneath a horizontal surface, Wood & Peregrine (1996) proposes the utilization of the pressure-impulse theory. Defined as the integral of non-hydrostatic wave pressures over the impact duration, the pressure-impulse is completely described theoretically by the Laplace equation. In this study, the pressure-impulse model is implemented for the experimental cases in two and three dimensions using a finite difference numerical scheme and validated against semi-analytical solutions with high accuracy. Boundary conditions are modified to include and assess the influence of venting holes on the pressure-impulse contours. To achieve the largest efficiency in the reduction of pressure-impulses, rectangular ventilations are located at the critical corner between vertical wall and overhang and spaced across the structure width.

Variation of geometrical parameters in the three-dimensional pressure-impulse model provides relationships between the release of pressure-impulses and the dimensions of the ventilations. The dimensional overhang length $\overline{L_o}$ is taken as the scaling factor in the pressure-impulse model so that the dimensionless overhang length L_o is always unitary. Since the dimensionless wall height L_y varies from 1.0 to 6.0, only cases where the overhang is equal or shorter than the vertical element are considered. The dimensionless spacing between ventilations along the overhang S ranges from 1.0 to 6.0, while the dimensionless venting hole length L_h and width W_h varies from 0.1 to 0.5. Sensitivity analysis of the venting parameters in the pressure-impulse model shows that spacing between holes exerts a much larger individual influence in the release of pressure-impulses than the length or width of the holes. Widening the venting holes is slightly more effective than increasing their lengths to decrease pressure-impulses, as the largest loadings are concentrated where the overhang edge contacts the vertical wall.

Based on the physical model dimensions, the open source CFD software OpenFOAM® is also employed to simulate standing wave impacts on structures. Three-dimensional simulations are performed with $\overline{S}/\overline{L_o} = 2.50$, $\overline{L_h}/\overline{L_o} = 0, 0.10$ for $\overline{L_y}/\overline{L_o} = 6.0$, and with $\overline{S}/\overline{L_o} = 1.25$, $\overline{L_h}/\overline{L_o} = 0, 0.05, 0.10$ for $\overline{L_y}/\overline{L_o} = 3.0$. Wave conditions are constant in every simulation, with incoming wave height $H_i = 0.06$ *m*, wave period $T = 1.30$ *s* and wave length $L_w = 2.42$ *m*. Waves are generated in the CFD model using the *waves2Foam* toolbox, in conjunction with the *OceanWave3D* utility. Convergence of the CFD model is achieved by gradually refining the mesh near the wave impact region, with spatial step of 3600 points per wave length. Validation between simulated and experimental total wave forces on the vertical wall shows very good agreement for both overhang sizes.

Separation of impulsive and quasi-static loads is performed with pressure-distribution formulas and low-pass filters to determine pressure-impulses. The results indicate that the filtering splitting method is reliable and provides impulses more similar to experiments than the pressure-distribution formulas. Calculated pressure-impulses are reduced with the inclusion of venting holes in the CFD model, even for cases where peak pressures are amplified.

Determining vertical impact velocities is required to convert dimensionless to dimensional theoretical pressure-impulses. Three distinct standing wave theories provide identical upward velocity values. Velocities were derived from surface elevation measurements at the first wave gauge away from the overhang. These derived velocities showed the best correspondence of dimensional pressure-impulses between theoretical and CFD models, with slightly lower velocities for the case of shorter overhang.

The distribution of first impact pressure-impulses along the vertical structure show similar trends among the pressure-impulse theory and CFD models. While large discrepancies are observed for predicted maximum pressure-impulses, the relative error of total impulse at wall between both models is below 16% for all main cases, and 9% on average. From both CFD and pressure-impulse model results, empirical relations are derived between relative venting area $A_h/(SL_o)$ and total impulse release R_I, where $A_h = W_h L_h$ is the total opening area. For the case of largest relative venting area (10%), the predicted release of total impulse is 25% in the CFD model and 61% in the pressure-impulse model. The assumption adopted in the theory of zero pressure-impulse at the venting position is not reproduced in CFD results, which leads to overestimation of the impact mitigation effects of ventilations using the pressure-impulse theory. This divergence in the venting boundary condition is possibly linked to the omission of convective acceleration terms in the pressure-impulse model, which describe the effect of flow acceleration with respect to space caused by the abrupt geometrical change near the venting hole. For considering the convective terms in the equations that describe the flow, the empirical relation from CFD results is recommended over pressure-impulse theory results, especially when ventilation is applied. Two main types of pressure-impulse release are found in CFD simulations of impacts with ventilations. The first is a concentrated decrease of pressure at the venting position, measured by the probe nearest to the hole. The second is a more intense and widespread release, measured both at sections through and away of the hole and mostly controlled by the spacing between ventilations.

The direct use of impulses as a design variable is proposed in the work of Chen et al. (2019). This is also endorsed in this study, due to the higher predictability potential of total impulses than peak forces demonstrated in the analysis of wave impacts. Even small decreases of total impulse due to ventilations may contribute significantly in the reduction of the design reaction force F_r. Two ventilation design methods for vertical structures with overhangs subject to wave impacts are proposed based on the research conducted in this study. The first design method employs the derived empirical relations, standing wave theories and theoretical pressure distributions to determine the total impulse affecting the structure. The second design method applies the splitting approach of measured impulsive forces with low-pass filters to calculate the total impulse, requiring numerical or physical modelling. Further research is needed to support the models with small and large scale experiments using ventilations and expand the validity range of the results.

List of Symbols

Wave Theory Parameters

H_i	Incoming wave height
T	Wave period
h_s	Water depth
a	Wave amplitude
L_w	Wave length
k	Wave number
ω	Wave angular frequency
U	Vertical wave velocity
x	Longitudinal direction
y	Tranverse direction

Physics Constants

g	Gravitational acceleration
ρ	Water density

Pressure-impulse Theory Parameters

P	Dimensionless pressure-impulse
P_{max}	Maximum dimensionless pressure-impulse at the vertical structure
$P_{max,0}$	Maximum dimensionless pressure-impulse at the vertical structure, without venting
$P_{max,vent}$	Maximum dimensionless pressure-impulse at the vertical structure, with venting
I	Total dimensionless impact impulse at the vertical structure
I_0	Total dimensionless impact impulse at the vertical structure, without venting
I_{vent}	Total dimensionless impact impulse at the vertical structure, with venting
L_o	Dimensionless length of overhang
L_y	Dimensionless height of the vertical structure
L_x	Length of computational domain
L_h	Dimensionless length of the venting hole
W_h	Dimensionless width of the venting hole
A_h	Dimensionless area of the venting hole
S	Dimensionless spacing between venting holes
W	Width of computational domain

$\bar{P}$	Dimensional pressure-impulse
$\overline{P_{max}}$	Maximum dimensional pressure-impulse at the vertical structure
$\bar{I}$	Total dimensional impact impulse at the vertical structure
$\overline{L_o}$	Dimensional length of overhang
$\overline{L_y}$	Dimensional height of the vertical structure
$\overline{L_h}$	Dimensional length of the venting hole
$\overline{W_h}$	Dimensional width of the venting hole
$\overline{A_h}$	Dimensional area of the venting hole
$\bar{S}$	Dimensional spacing between venting holes
R_P	Release of maximum pressure-impulse at the vertical structure due to venting
R_I	Release of total impact impulse at the vertical structure due to venting

Hydraulic Parameters

p	Non-hydrostatic pressure
p_{max}	Peak non-hydrostatic pressure
F_v	Impulsive vertical force
F_{vqs}	Quasi-static vertical force
F_{hqs}	Quasi-static horizontal force
$\vec{u}$	Water flow velocity vector

Impact Analysis Parameters

t	Time
t_1	Time at beginning of impact
t_2	Time at end of impact
t_r	Impact rise time
t_i	Instant of impact
Δt	Total impact duration
α_r	Ratio between impact rise time and impact duration
F	Total force on the vertical structure, per meter wide
F_p	Peak impulsive force on the vertical structure, per meter wide
$\tilde{F_p}$	Estimated peak impulsive force on the vertical structure, per meter wide
F_{qs}	Peak quasi-static force on the vertical structure, per meter wide
F_r	Total reaction force on the vertical structure, per meter wide
U_M	Measured vertical wave impact velocity
U_D	Derived vertical wave impact velocity
ω_n	Natural angular frequency of the structure

T_n	Natural period of the structure
D_f	Dynamic load factor

Other Symbols

∇	Differential operator
∇^2	Laplace operator
$\otimes$	Outer product

Contents

1

Introduction

1.1. Motivation

This thesis is motivated by the necessity to prevent damage to coastal structures with overhangs caused by extreme wave impacts. Failure cases demonstrate that impacting waves generate uplift pressures which threaten the stability of the structure. Climate change and sea level rise will probably increase the occurrence of this phenomenon. The use of ventilations is proposed to alleviate the impact pressures, but there are currently no design guidelines available. Better understanding of the effects of ventilations would potentially lead to safer and more economical solutions.

1.1.1. Background

The coastal zone represents a crucial area of socio-economic development by providing valuable subsistence resources, access to marine trade and navigation, along with recreational and cultural activities, resulting on higher population density than in non-coastal areas. Population growth is expected to further increase the demand for coastal developments in the next decades. By 2060, the global population in the low-elevation coastal zone might increase up to 122% (Neumann et al. (2015)). Moreover, studies indicate the median average of 0.72 m sea level rise until the end of the century (Nicholls et al. (2018)), and 60% expansion from 2010 to 2050 of urban areas exposed to flooding caused by storms expected to occur once every 100 years (Jongman et al. (2012)). Climate change is likely to increase the frequency and intensity of storm surges and significant wave heights. Shortage of sediment sources due to natural causes or human activities such as river damming aggravates coastal erosion. These facts highlight safety concerns against flooding and the need for resilient coastal defense structures under stronger wave loading scenarios.

Usually during storms or hurricanes, structural failure occurs if the wave loading exceeds the capacity of the structure. Figure 1.1 demonstrates damage on decks at the U.S. 90 Bridge over Biloxi Bay due to extreme vertical wave impacts after Hurricane Katrina, when storm surge level reached 6.6 m and significant wave heights were about 2.6 m (Hayatdavoodi & Ertekin (2016)). Oumeraci (1994) reviewed 17 failure cases of vertical breakwaters and concluded that predicting wave impact loads, along with dynamic soil characteristics, are the main sources of uncertainties affecting the stability of the structure.

Scientific observations of the force of the waves on maritime structures date back to the 19th century, when dynamometers were used to measure wave breaking pressures at different levels of a sea wall (Stevenson (1874)). But only in the 1930s, with the advent of electrical recording equipment, that more precise measurements became available (Bagnold (1939)), allowing peak pressures to be identified over timescales in the order of milliseconds. Also known as shock pressures, these peak pressures can reach values 220 times greater than the hydrostatic pressure (Kirkgöz (1991)).

Wave loads on coastal structures can be categorized as slowly-acting pulsating loads or short and intense impulsive loads (Kisacik et al. (2014)). Impulsive loads are approximately 20 times more intense

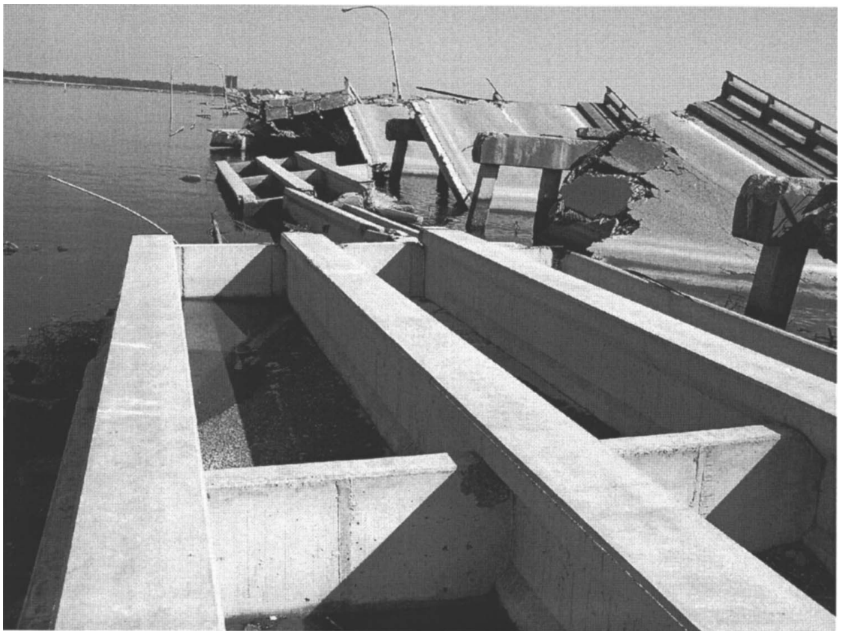

Figure 1.1: Damage on bridge decks caused by wave impacts during hurricane Katrina (Robertson et al. (2007)).

but 1000 times shorter in duration than pulsating or quasi-static loads (Cuomo et al. (2004)). Sainflou (1928) provided formulations to predict quasi-static wave loadings from standing waves using a second order Stokes theory. Engineers often apply the method proposed by Goda (1974) to predict pulsating horizontal wave forces on caisson breakwaters and the expanded method by Takahashi & Hosoyamada (1994), which introduced coefficients to estimate impulsive forces. But these popular methods fail to account for vertical impacts and, according to Cuomo et al. (2010), they both underestimate horizontal impacts for assuming they would be damped by a dynamic response of the caisson.

Several other theories have been developed to describe impulsive wave impacts on vertical structures (Oumeraci et al. (2001)). Bagnold (1939) proposes that the peak pressures are caused by the abrupt deacceleration of water mass by a thin layer of air compressed in between the wave front and the sea wall. Partenscky (1989) defines the instantaneous pressure distribution as the momentum exchange between the mass of water and the rigid structure. Cooker & Peregrine (1995) present a mathematical model to determine wave impacts on vertical walls analytically, using the pressure-impulse theory. The pressure-impulse of impacts has the advantage of being less variable than localized pressures Renzi et al. (2018). The pressure-impulse model can be adapted to several geometries, such as caisson breakwaters, vertical cylinders or flap-type energy converter (Walkden et al. (2001), Ghadirian & Bredmose (2019), Renzi et al. (2018)).

Previous research indicates that the magnitude of impulsive wave impact pressures on vertical walls is highly dependent on the wave breaker types (Kisacik et al. (2014)). Oumeraci et al. (1993) classified four main breaker types according to their temporal and spatial pressure distributions. Hull & Müller (2002) investigated wave shapes through sequential flash photography, suggesting four main breaker types: flip through, small air pocket, large air pocket and turbulent bore. The maximum pressure was found for a plunging breaker type with large air entrapment.

Wave-in-deck loads refer to loads affecting overhanging structures exposed to wave action, including decks, piers, jetties, platforms, cantilever slabs and beams (Allsop et al. (2009)). To reduce the vulnerability of such structures, the air gap approach is recommended, which consists of setting the deck above the reach of predicted wave conditions (McConnell et al. (2004)). However, sufficient deck clearance is not always possible due to practical constraints. Prediction methods for wave-deck loads have been proposed by Shih & Anastasiou (1992), Kaplan (1992), Cuomo et al. (2007), among others. Based on experimental results and statistical analysis, Shih & Anastasiou (1992) suggested a relationship between wave height, water density and acceleration of gravity to estimate maximum vertical pressures on decks. Kaplan (1992) describes the maximum vertical force on a flat plate deck structure resultant from momentum and drag force analysis, using techniques derived from ship slamming studies. Cuomo et al. (2007) reviewed and compared six of the most important prediction methods, and developed a new formula using parametric and dimensionless analysis.

1.1.2. Problem description

As discussed in the background section, knowledge about wave impact pressures on vertical coastal structures such as caisson breakwaters and horizontal coastal structures such as bridge decks and piers is well documented. However, research is still scarce regarding the case of a vertical structure combined with a projecting surface. Even though exposed horizontal elements should be avoided from a wave impact perspective, they are commonly designed in combination with sea walls and breakwaters in the form of return walls to prevent wave overtopping (Kisacik et al. (2012), van der Meer et al. (2018)), or due to other reasons. Since this particular enclosed geometry restricts dissipation of wave energy through overtopping, Kisacik et al. (2012) argues that loading conditions for the combined case (wall with overhang) are more severe than for the other isolated situations. Castellino et al. (2018) observed a significant increase of the magnitude of wave impacts on recurved sea walls when compared to vertical walls. Chen et al. (2019) mentioned the importance of developing a new design method for impulsive impacts on vertical structures with overhangs.

Openings along the horizontal element, also known as ventilations or venting holes (Hofland et al. (2019)), are proposed to promote energy dissipation and consequently release the wave impact loadings. Regarding the use of ventilations as a design tool, three main research gaps can be identified:

First, the theoretical effects of ventilations on the wave impact magnitudes are not described in the literature. Wood & Peregrine (1996) give analytic solutions to determine wave pressure-impulses on coastal structures with overhangs for infinite depth, infinitely long decks and in more general conditions. It was demonstrated that the pressure impulse is greater for shallower depths and concentrated near the landward edge of the deck. Increased shearing forces are found near the seaward edge of the deck due to strong pressure gradients. Even though ventilations are not included in the theory, their influence could be evaluated by modifying the boundary conditions of the problem.

Second, despite computational fluid dynamics already being utilized to successfully simulate wave-structure interactions (Hu et al. (2016)), there still is a need for validated numerical models of wave impacts on vertical structures that include ventilations. For instance, Huang et al. (2018) simulated wave impacts on vertical and overhanging coastal structures using OpenFOAM and validated the model using data from Robertson et al. (2013). The simulation results evaluated the effects of varying overhang lengths and bed slopes on the horizontal and vertical forces, but there was no indication of using ventilations or any other design measures to release those forces.

Third, there are no guidelines available for the utilization of ventilations in engineering design. As shown in Figure 1.2, the flood gates in the Afsluitdijk represent an example of vertical coastal structure with an overhanging horizontal slab, which requires dimensioning of ventilations. Another example is the Eastern Scheldt storm surge barrier, the largest of the Delta Works projects in the Netherlands. Research is necessary to quantify wave pressure release, reduce uncertainties and provide guidance regarding the optimal geometry, positioning and spacing of ventilations.

From the identified knowledge gaps, the problem description of this thesis can be outlined in three main points:

- **Theory:** demand for testing theoretical methods to determine pressures on vertical structures with overhangs including ventilations.
- **Modelling:** demand for validated numerical modelling to assess effects of ventilations for wave pressure release on vertical structures.
- **Design:** demand for optimized engineering design of ventilations in coastal structures.

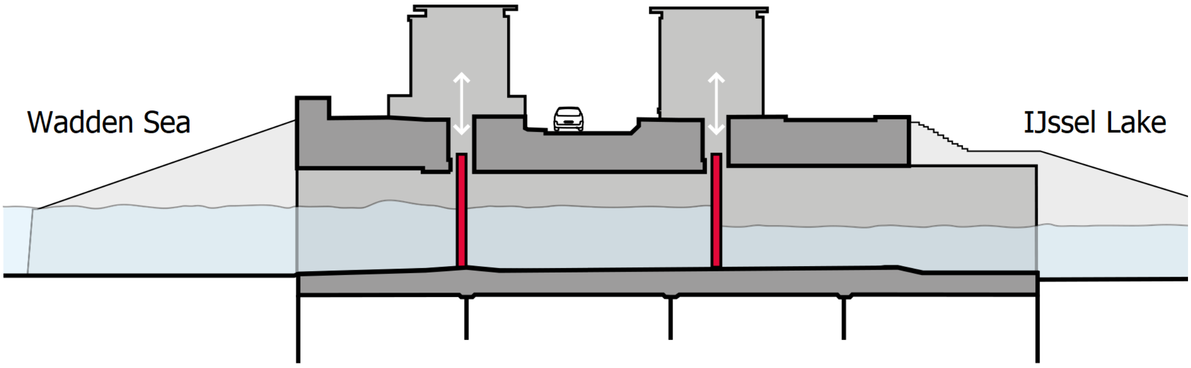

Figure 1.2: Flood gates in the Afsluitdijk (Rijkswaterstaat (2015)).

1.2. Objectives

The central objective of this thesis is to address the demands for research consequent from knowledge gaps in the literature. This is achieved by answering the following main research question and sub-questions:

Research question:

What are the effects of ventilations in the design of vertical coastal structures with overhangs described by the existing wave impact pressure-impulse theory and computational fluid dynamics

Research sub-questions:

1. **How can the pressure-impulse model be used to assess the three-dimensional effects of ventilations on overhanging coastal structures?**
2. **What is the predicted reduction of impulsive wave impact loadings on overhanging coastal structures with ventilations using computational fluid dynamics models?**
3. **How to apply the pressure-impulse model and computational fluid dynamics results in the engineering design of coastal structures with venting and subject to wave impacts?**

1.3. Methodology

In order to answer the aforementioned research questions, the thesis work is divided in three main parts, as depicted in Figure 1.3. Following the literature study, **Part I** applies a theoretical approach to assess the effects of ventilations on coastal structures with overhangs. **Part II** simulates numerically similar conditions using computational fluid dynamics. **Part III** comprises analysis and validation of the performed modelling, discussion and application in engineering design.

- **Part I:** addresses research sub-question 1.
- **Part II:** addresses research sub-question 2.
- **Part III:** addresses research sub-question 3.

Part I employs the pressure-impulse method for wave impacts on horizontal surfaces from Wood & Peregrine (1996) for boundary conditions including and excluding ventilations. The theory is applied for problems in two and three dimensions.

Part II utilizes the software OpenFOAM coupled with waves2Foam to predict the influence of ventilations on wave impacts for similar cases. The numerical model is validated with experimental tests

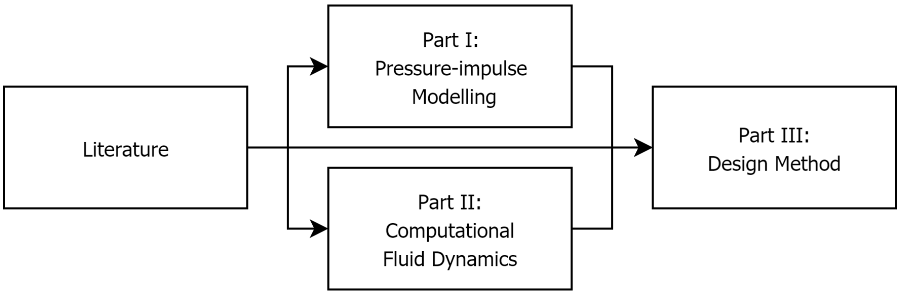

Figure 1.3: Main thesis parts and methodology.

conducted in the Fluid Mechanics Laboratory from TU Delft, as depicted in Figure 1.4 (de Almeida et al. (2019)).

In **Part III**, the resulting wave loads from theoretical and computational fluid dynamics models are compared for validation. Processing, analysis and engineering design implications are also treated.

Completing all three main parts of this thesis addresses every research sub-question and consequently assures that the main research question is answered.

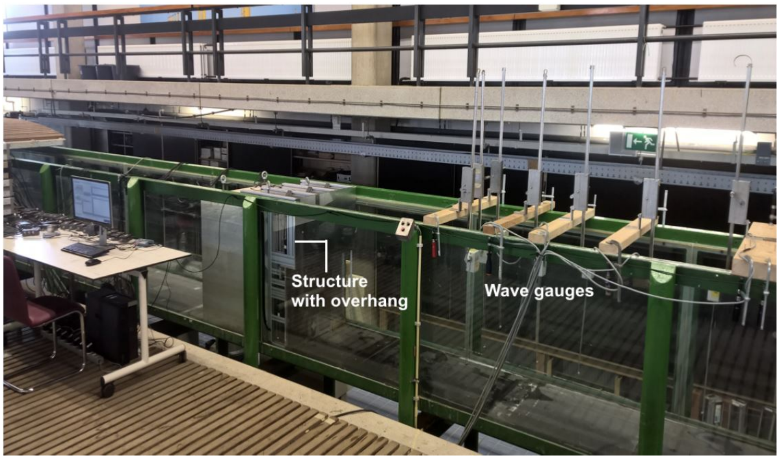

Figure 1.4: Wave flume used for physical experiments (de Almeida et al. (2019)).

1.4. Structure

The structure of this thesis is organized after the methodology defined in the previous section, as illustrated in Figure 1.5.

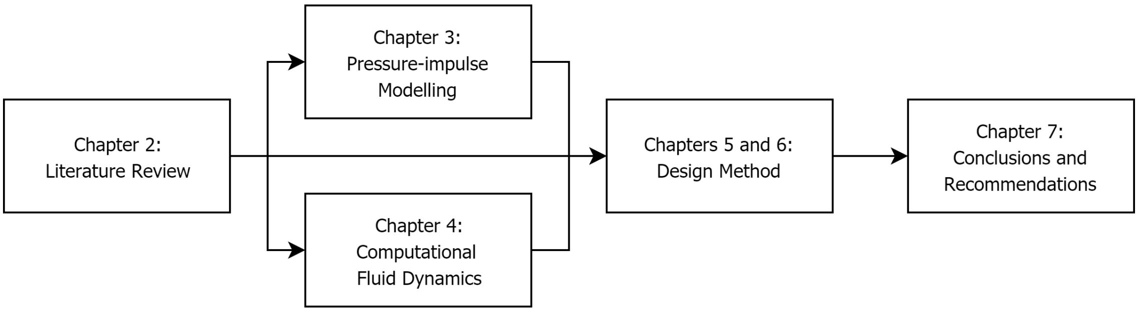

Figure 1.5: Thesis structure and chapters.

The content of each chapter is briefly outlined as follows:

- **Chapter 2 - Literature review:** introduces the theoretical concepts related to the prediction of wave impact pressures on vertical coastal structures with overhangs.
- **Chapter 3 - Pressure-impulse modelling:** applies the available model from literature describing wave impacts on vertical structures with overhangs to assess the effects of ventilations.
- **Chapter 4 - Computational fluid dynamics:** sets up and simulates numerically wave impacts on structures excluding and including ventilations using OpenFOAM.
- **Chapter 5 - Analysis and validation:** processing and comparison of the main results involved in the performed theoretical and numerical models.
- **Chapter 6 - Discussion:** evaluates the validity and applicability of the models for engineering design and discuss main findings and limitations.
- **Chapter 7 - Conclusions and recommendations:** summarizes main conclusions of the thesis and suggests topics for future investigation.

2

Literature review

The main concepts and theories considered for the evaluation of ventilations to relieve wave impact pressures on vertical structures with overhangs are summarised in this chapter. It includes the most important methods and design aspects to assess pulsating and impulsive wave impacts on vertical walls and overview of present research concerning wave loadings on vertical structures with overhangs. The application of the pressure-impulse theory and the required estimation of wave velocity is then discussed.

2.1. Vertical structures

Vertical structures in coastal engineering are represented mainly by sea defence structures such as seawalls, caisson breakwaters and storm surge barriers. Wave loadings, the predominant load for these structures, are classified as pulsating (quasi-static) or impulsive loads. The following sub-sections presents the definition and common estimation methods for both loading classifications. Moreover, conventional design practices for vertical structures are outlined.

2.1.1. Pulsating wave loadings

Pulsating or quasi-static wave loadings are characterized by slow pressure variations at a wall, resulting from large period waves. The size of the wave period is much greater than the natural structural oscillation period, the pressures vary almost in phase with the wave elevation and there is no air entrapment phenomenon (Kisacik (2012)). The order of magnitude of the quasi-static loading duration is usually between 0.25 to 0.5 times the wave period T, presenting forces as a function of the incoming wave height (McConnell et al. (2004)). Due to the large period involved, pressures are considered to be static in design calculations.

Pulsating wave loadings on vertical structures are typically associated in the literature with broken, standing or upward-deflected waves Oumeraci et al. (2001). Assuming a standing wave scenario with full reflection at wall, the simplest way of determining the quasi-static pressure distribution $p(y)$ along depth (y direction) is given by linear wave theory (Kisacik (2012)):

$$\begin{aligned} p(y) &= \rho g H_i \frac{\cosh(k(h_s + y))}{\cosh(kh_s)} && \text{for } -h_s < y < 0, \\ p(y) &= \rho g H_i \left(1 - \frac{y}{H_i}\right) && \text{for } 0 < y < H_i, \end{aligned} \tag{2.1}$$

where:

H_i = incoming wave height,
k = wave number ($k = 2\pi/T$),
h_s = water depth,
ρ = water density,
g = gravitational acceleration.

Resultant forces at the structure can also be obtained by integrating pressures from Equation 2.1 over the water depth. For a second order approximation of the pressures, Sainflou (1928) proposed a formula using Stoke's second order wave theory for relatively deep water:

$$\begin{aligned} p_1 &= (p_2 + \rho g h_s)\frac{H_i + \delta_0}{h_s + H_i + \delta_0}, \\ p_2 &= \frac{\rho g H_i}{\cosh(k h_s)}, \\ p_3 &= \rho g (H_i - \delta_0), \end{aligned} \tag{2.2}$$

where:

δ_0 = increase of still water level ($kH_i^2 \coth(kh_s)/2$),
p_1 = maximum pressure at still water level,
p_2 = maximum pressure at the toe of the structure,
p_3 = maximum pressure under wave through.

Reasonably good predictions were found for Sainflou's method when compared to experimental results, in the region of incoming wave height to water depth ratios H_i/h_s between 0.2 and 0.5, but underpredicted pressures outside this range (Oumeraci et al. (2001), McConnell et al. (2004)).

Initially created for caisson breakwaters, the formulation from Goda (1974) can also be applied to calculate pulsating loads on vertical walls. The method utilizes fourth order wave theory in an attempt to increase accuracy and is validated after experiments in a large wave channel. The results indicate a trapezoidal distribution of pressures vertically, with maximum pressures given by

$$\begin{aligned} p_1 &= 0.5(1 + cos\beta)(\alpha_1 + \alpha_* cos^2\beta))\rho g H_D, \\ p_3 &= \alpha_3 p_1, \\ p_4 &= \alpha_4 p_1, \end{aligned} \tag{2.3}$$

with parameters described as

$$\begin{aligned} \eta^* &= 0.75(1 + \cos\beta) H_D, \\ \alpha_1 &= 0.6 + 0.5\left(\frac{4\pi h_s/L_w}{\sinh(4\pi h_s/L_w)}\right)^2, \\ \alpha_2 &= \alpha_* = min\left[\left(\frac{h_{br} - d}{3h_{br}}\right)\left(\frac{H_D}{d}\right)^2, \frac{2d}{H_D}\right], \\ \alpha_3 &= 1 - \left(\frac{h_w - h_c}{h_s}\right)\left(1 - \frac{1}{\cosh(2\pi h_s/L_w)}\right), \\ \alpha_4 &= 1 - \frac{h_c}{\eta^*} && \text{for } \eta^* > h_c, \\ \alpha_4 &= 0 && \text{for } \eta^* \leq h_c, \end{aligned} \tag{2.4}$$

where:

L_w = wave length,
H_D = outside surf zone: $H_D = 1.8H_{1/3}$; inside surf zone: $H_D = H_{max}$ at distance $5H_{1/3}$ from wall,
$H_{1/3}$ = deep water significant wave height,
H_{max} = maximum wave height among 250 random waves,
β = wave attack angle,
h_{br} = water depth at distance $5H_{1/3}$ from wall,
d = water depth at the structure,
h_w = wall height,
h_c = wall height above still water level.

The Linear Wave Theory, Sainflou and Goda methods follow first, second and fourth order wave theories, respectively. These are the most common models to predict quasi-static wave loadings on vertical structures. Figure 2.1 illustrates the pressure distributions on vertical walls according to each method.

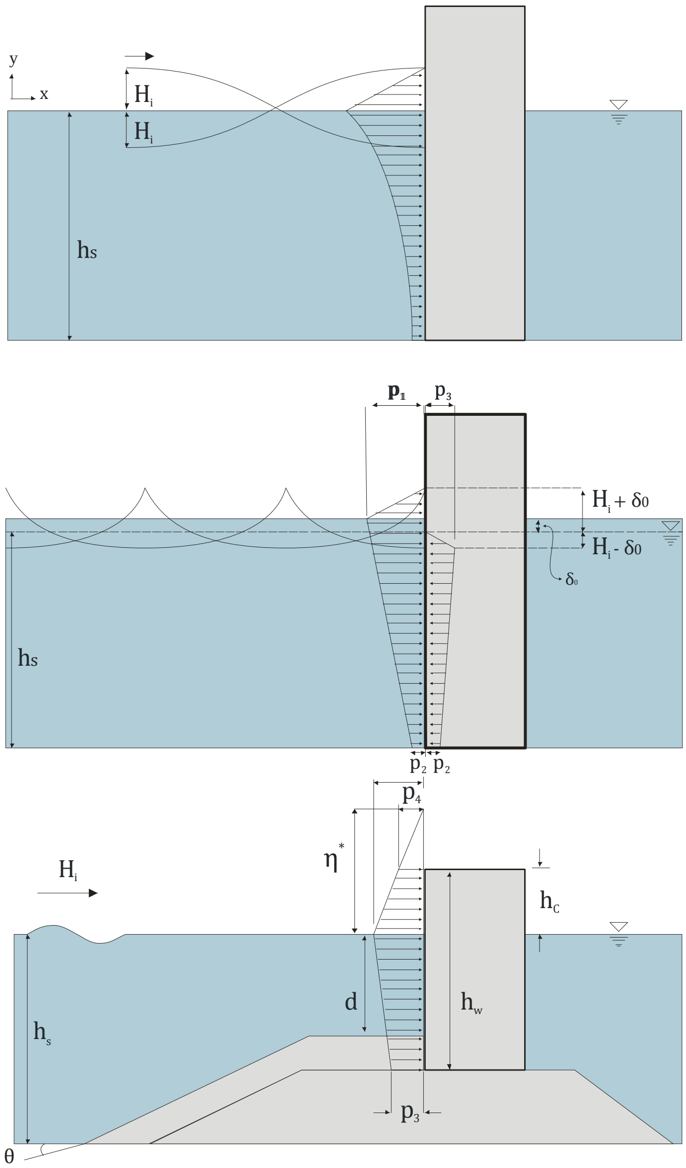

Figure 2.1: Pressure distributions as described by the Linear Wave Theory, Sainflou and Goda methods (Kisacik (2012)).

2.1.2. Impulsive wave loadings

When waves approach shallow water, shoal and break in contact with a structure, intense impulsive or shock pressures can be generated. Impulsive loadings are defined by very short and intense impact pressures, composed of a horizontal and vertical components. During the brief impact time, the incoming wave that travels with celerity c suddenly loses forward momentum, which is converted into an impulse applied on the wall (Goda (2000)). The geometry of the wall and wave front, incoming wave steepness, beach slope and air entrapment in water are among the main parameters that influence the magnitude of the impulsive pressure (McConnell et al. (2004)).

Bagnold (1939) was one of the first to record impulsive pressures from breaking waves. Observations from small scale tests identified shock pressures when a thin air layer is enclosed between the wave front and the face of the wall. Peak pressures much larger than the hydrostatic pressure were measured. Kirkgöz (1991) reviewed several impact pressures empirical results from model, prototype and field experiments and found maximum impulsive pressures up to 111 times the hydrostatic pressure, as opposed to 220 times presented by Bagnold (1939). Kirkgöz (1991) performed experiments in a wave flume 100 m long, 2 m wide, 1.25 m deep and 1/10 slope. It was concluded that maximum impact pressures can be larger on sloping walls than on vertical walls and they most commonly happen slight under the still water level. Statistical analysis showed that the stochastic behaviour of the impacts can be fitted successfully on a log-normal distribution.

Hull & Müller (2002) analysed geometrical variations of the wave shape before, during and after collision with a vertical wall using a 17 m long, 0.35 m wide, 1.20 m deep wave tank with 1/10 slope. The wave impacts were photographed in a rate of 20 frames per second. Four breaker classifications were tested, following work from Oumeraci et al. (1993):

1. Flip through: no air entrapment during wave breaking and the wave is upward deflected. It consists of an intermediate stage between a total clapotis and a small air pocket breaker.
2. Plunging breaker with small air pocket: sharp sound due to air compression.
3. Plunging breaker with large air pocket: fast and complete wave front steepening with breaker crest curling.
4. Turbulent bore breaker: collapse of the wave happens early, before reaching the wall.

Hull & Müller (2002) found that the maximum impact pressure occurs for a fully developed plunging breaker with large air pocket at still water level. The impulsive pressure is regarded as a consequence of a fluid-solid contact of the breaking wave with the wall. Air entrapment caused secondary oscillating pressures.

Hofland et al. (2011) performed field scale measurements with extensive amounts of data in the Delta Flume of Deltares, which is 200 m long, 5 m wide and 7 m deep. Among the 137 impacts measured, 8 impacts had pressures larger than 1 MPa, with 2.7 MPa as the maximum pressure measured. The largest pressures were observed for flip through impacts.

Partenscky (1989) divided the wave breaking at a vertical wall in three phases: wave approaching the wall, wave before hitting the wall and maximum wave impact on the wall. Assuming a linear distribution of pressure $p(y,t)$ along the wall during the impact, impulsive pressures then can be described theoretically as

$$p(y,t) = \frac{p_{max}(y)t}{t_i}, \tag{2.5}$$

with

$$p_{max}(y) \approx \frac{2\rho H_i}{t_i} V(y), \tag{2.6}$$

where $V(z)$ is the horizontal wave velocity component distributed along the wall height z and estimated from linear wave theory for $y \leq 0$ and approximated as half of the shallow water wave celerity $c = \sqrt{gh_s}$

for $z > 0$. The time of increase of pressure until p_{max} is represented by t_i.

To account for impulsive impacts from breaking waves on vertical walls, Takahashi & Hosoyamada (1994) introduced modification factors for the Goda (1974) method. A coefficient α_* is given as function of wave and geometrical properties, and applied in Equation 2.3. Due to restrictions associated with breaking wave conditions and structure geometry, the modified Goda method is out of the scope of this thesis.

2.1.3. Design practices

For pulsating wave conditions, the design guidelines for vertical structures are relatively well developed. The formula developed by Sainflou (1928) has been recommended by the Shore Protection Manual and Coastal Engineering Manual to predict pulsating impacts caused by low steepness waves (McConnell et al. (2004)). Also, the method developed by Goda (2000) constitutes the benchmark to assess wave loadings at vertical walls (Hofland et al. (2011), Cuomo et al. (2010)).

For impulsive wave conditions, the method by Takahashi & Hosoyamada (1994) is widely utilized by engineers to complement the original Goda method. According to Goda (2000), engineers should avoid designing vertical structures at locations vulnerable to impulsive wave impacts and choose to utilize mound breakwaters instead. If this is not possible due to physical constraints, it is recommended to protect the vertical structure with energy-dissipating concrete blocks, allowing for much lower design pressures to be adopted. The frequency of occurrence of impulsive waves can be even more important than their magnitudes. Another crucial consideration is the angle of attack β which the waves approach the structure. To evaluate the possibility of impulsive loads, a questionnaire has been proposed contemplating specific combinations of wave conditions, bottom slope and profile characteristics of a vertical wall.

A probabilistic approach for design of vertical, composite, perforated and armoured caisson breakwaters has been proposed by the PROVERBS program (Oumeraci et al. (2001)). Concerning the hydraulic aspects of the program, the objective was to review, test and improve existing design procedures, especially the ones related to impulsive impact loadings. A new method was developed to obtain horizontal forces on vertical breakwaters after extensive model, prototype and field scale experiments. The parameter $P_{i\%}$ is introduced as a function of wave heights to determine whether non-breaking or breaking loads are expected. However, the application of the PROVERBS methodologies is complex and can still lead to significant prediction uncertainty (Kisacik et al. (2012)).

Oumeraci (1994) reviewed the technical causes of failure for 17 vertical and 5 armoured vertical breakwaters, from 1881 to 1987. The reasons for failure were classified in three main groups: causes related to the structure, causes related to hydraulic conditions and causes related to geotechnical conditions. The hydraulic conditions group was subdivided in wave loadings, design wave exceedance, wave concentration and wave overtopping. It was shown that almost all failures were mainly caused by wave breaking pressures from violent storms, even though in some situations the depth conditions were considered to prevent wave breaking on the structure. The early idea that vertical structures would reflect wave energy towards open sea led many engineers to completely disregard the occurrence of impulsive wave loadings. The most prevailing failure modes associated with horizontal wave loadings are sliding and foundation shear failure.

2.2. Vertical structures with overhangs

The response from vertical structures with overhangs subject to wave impacts is significantly distinct from entirely vertical structures. Only pulsating loads are observed for structures subject to standing waves with freeboards larger than the wave height. In this case, the loads are equivalent to the situation without overhangs. But if the standing wave collides with the horizontal overhang, impulsive loads are generated (de Almeida et al. (2019)). The following sub-sections discuss specific wave loadings and engineering design issues for this type of structure. Ventilations are introduced as design elements in sub-section 2.2.3.

2.2.1. Impulsive wave loadings

Huang et al. (2018) assessed wave impacts of solitary waves on vertical and overhanging coastal structures using IHFOAM. Two simulations with $H_i = 0.133$ m and $H_i = 0.266$ m were validated through comparison of both wave surface elevations and horizontal forces with experimental data from Robertson et al. (2013). Analysis of the loading duration, bed slope and overhangs lengths concluded that wave impacts are maximum for waves breaking at the structure. But this wave breaking was caused by a sloping sea bed. For flat sea bottoms, wave breaking does not occur.

Standing waves are resultant from the interaction of incoming and reflected waves by solid vertical boundaries such as seawalls. The incident and reflected waves have same phases but opposite directions, which leads to amplification of wave heights and possibility of reaching a suspended structure. Wilde et al. (1998) investigated impulsive standing wave impacts on a horizontal plate though small scale wave flume experiments. Resonance was established by the harmonic motion of a wave-maker, inducing a standing surface wave with increasing amplitude in time until collision with the plate occurred, causing a peak pressure of 14 kPa over a time interval of 10 ms. Similar impulsive impacts from standing waves are also observed for larger scale physical and numerical experiments.

The scientific literature regarding impulsive breaking wave loadings is very extensive (Hull & Müller (2002), Oumeraci et al. (1993)). Less known is the impulsive impact caused by non-breaking waves in deeper water depths or flat bottoms, under confined configurations. Structures with exposed overhangs may be vulnerable to impulsive impacts from non-breaking standing waves under the horizontal surface, which propagate also to the vertical part (Castellino et al. (2018)).

Experiments were conducted by Kisacik et al. (2014) in a small scale wave flume to investigate impulsive wave impacts on a vertical wall 0.3 m high with an overhanging horizontal slab 0.6 m long. The tests considered four water depths and five wave periods for regular and irregular waves. The relationship between measured forces and the hydraulic parameters was analysed to generate response fitting functions $(c'/h_s)^2$ so that the impulsive vertical force F_v can be estimated as

$$F_v = \beta_1 \rho g h_s^2 (H_i/h_s)^{\beta_2}, \tag{2.7}$$

where $\beta_1 = -1.5(c'/h_s)^2 + 37.7$ and $\beta_2 = -0.22(c'/h_s)^2 + 3.83$. This expression is valid for the range $0.45 \leq H_i/h_s \leq 0.80$. The quasi-static vertical force F_{vqs} can be estimated as

$$F_{vqs} = \gamma_1 F_{hqs}, \tag{2.8}$$

where $\gamma_1 = 0.021(c'/h_s)^2 + 0.32$ and F_{hqs} is the horizontal quasi-static obtained by integrating pressures from the Goda method through Equations 2.3 and 2.4 with $H_D = 1.8H_i$. Then the rise time t_r can be estimated from the empirical relationship

$$\frac{F_v}{F_{vqs}} = 0.22\frac{t_r}{T} - 0.56. \tag{2.9}$$

Castellino et al. (2018) performed a numerical study on the influence of geometry of caisson breakwaters under standing wave loadings. Simulations of breakwaters with vertical and a fully recurved wall (90°) were compared for varying wave conditions. Results showed impulse pressures significantly higher for overhanging recurved walls, with peak pressures concentrated under the recurved parapet (Figure 2.2). It is argued that this confined wave impact reflects the sudden interruption of horizontal momentum of water mass due to the geometry of the structure, resulting on impulsive wave impacts due to flow deflection. Effects of compressibility of water were considered to be minimal and air entrapment was not found on the experiments.

Chen et al. (2019) measured breaking and non-breaking wave impacts during laboratory scale experiments for once in 10000 year conditions. The structure consisted of a vertical wall with an overhanging

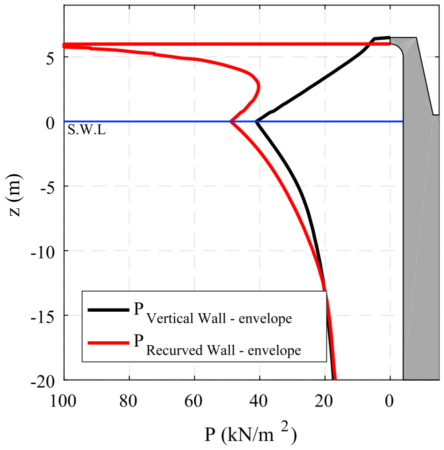

Figure 2.2: Comparison of impulsive pressures on recurved and vertical walls (Castellino et al. (2018)).

beam. It was observed that impacts from standing waves produced more impulsive impact events than breaking waves, specially for higher water levels, following the classification from Kortenhaus & Oumeraci (1998).

2.2.2. Design aspects

Coastal vertical structures with overhangs are treated in the EurOtop Overtopping Manual (van der Meer et al. (2018)) as seawalls with parapets or wave return walls. These elements are applied at the top of structures to redirect up-rushing waves seawards, decreasing overtopping and consequently preventing floods. An example of vertical wall with a fairly considerable parapet subject to impulsive wave impacts is represented in Figure 2.3. Since the EurOtop Manual is focused on wave overtopping, no direct guidelines regarding wave impacts on wave return walls or parapets are provided.

Figure 2.3: Sea wall with significantly large parapet at Cascais, Portugal (van der Meer et al. (2018)).

Guidelines for design of coastal structures under wave loadings, by McConnell et al. (2004), highlight the importance of keeping a minimum vertical distance between the water level exposed horizontal structural elements like decks and beams of jetties or piers. This air gap clearance is governed by an extreme wave crest elevation estimated from significant wave heights. Also, Kaplan's model (Kaplan (1992)) is recommended to predict vertical forces from wave impacts. However, this model only holds for horizontal elements detached from vertical structures.

According to Chen et al. (2019), even though impulsive impacts are crucial for the design of marine structures, they are often not explicitly considered due to the assumption that the structural natural period is much longer than the wave loading durations. But dynamic effects of damping and amplification from impulsive forces are not always understood, specially for slender structures like sluice gates and storm surge barriers.

In addition to that, the common engineering methods for determination of wave loadings are not suitable for impulsive impact pressures on vertical structures with overhangs. For instance, formulations from Sainflou (1928) and Goda (1974) are appropriate only for quasi-static loads. Even the modified Goda method for impulsive loads by Takahashi & Hosoyamada (1994) is inadequate, since it only applies to solely vertical structures, such as caisson breakwaters. The absence of theoretical insights on how to deal with these impacts became evident during the renovation projects of discharge sluice gates in the Afsluitdijk (Chen et al. (2019)). To acquire knowledge about the phenomenon, engineers implement physical or computational models.

From these models, the traditional engineering design approach consists of initially considering a time-series of the impacting loadings. Then, statistical examination determines design peak loadings for an arbitrary frequency of occurrence. This can be done through extreme value analysis, for example. Finally, these peak loads are applied to an structural model to obtain design reaction loads. For complex geometries, this approach may lead to vast overestimation of wave loadings on the structure (Chen et al. (2019)).

As an alternative to computational and physical modelling, the wave pressure-impulse theory developed by Cooker & Peregrine (1995) might provide a simplified but reliable way to consider impulsive wave impact pressures. Measurements of wave impacts show good agreements with predictions from this theory with relative insensitivity to the colliding wave shape (Cooker & Peregrine (1995),Wood & Peregrine (1996)). Peak pressures from shock wave loadings are highly variable, show stochastic behavior and therefore are difficult to predict, but the integral over time of localized pressures is more well behaved (Renzi et al. (2018)). Moreover, pressure-impulse calculations are much less computationally expensive than computational fluid dynamics.

As an example of application of the pressure-impulse theory for complex geometries, Renzi et al. (2018) developed an analytical model to predict wave slamming impacts on a flap-type wave energy converter. The analytical model was compared to 27 pressure-impulse values measured from experimental data. The influence of the air pocket during impacts was considered in the model by introducing an air entrapment coefficient. Parametric analysis was performed to evaluate a wetting parameter and impact angle on the flap. The model was validated demonstrating that the peak slamming pressures predicted for distinct air factors are in a compatible range with the experimental results.

Based on pressure-impulse analysis, Chen et al. (2019) introduced a new design approach for impulsive loads on structures with overhangs. The new approach comprises filtering impulsive loads from quasi-static loads using the theoretical principles from Cooker & Peregrine (1995), and statistically analysing them separately. This approach provides better inclusion of impulsive wave impact loads into structural models (Chen et al. (2019)).

2.2.3. Ventilations

The use of ventilations or openings along the structure consists of a design alternative sometimes employed in coastal engineering. For instance, perforated vertical walls are commonly used in some countries to reduce wave reflection and overtopping, even though few studies exist to assess the effects of the perforations (van der Meer et al. (2018)).

Gaeta et al. (2012) investigated the effects of venting on prototype jetties exposed to vertical wave forces. The openings were tested in the form of circular holes at the corners of rectangular plates, in two configurations: 3% and 10% of the total deck area. When compared to the case without venting, it was observed that the holes decreased the maximum forces at the deck, as them allowed air and water to quickly emerge upwards, but the pressure relief amount was not specified.

Azadbakht & Yim (2016) performed numerical experiments to predict uplift and horizontal wave forces at bridge superstructures. Ventilations were positioned along the bridge deck spans in the model (Figure 2.4a). It was argued that the effects of the venting holes are three dimensional since their lengths are small compared to the bridge deck length. Simulations were performed without the effect of air (single-phase model), including the effect of air and with ventilations. The results showed 56% average reduction of the wave loads with venting covering only 3% of the deck area (Figure 2.4b), due the trapped air offering resistance against wave impacts and consequently increasing loads.

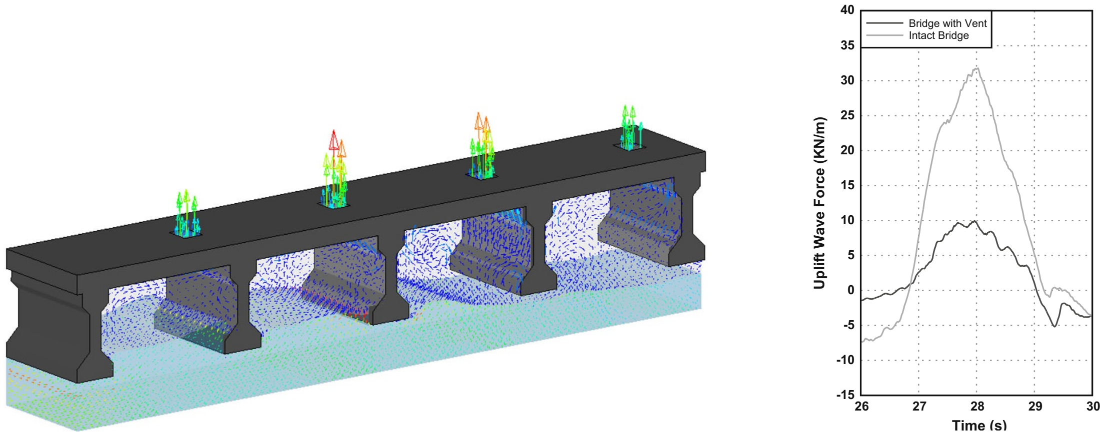

(a) (b)

Figure 2.4: Effects of venting on a bridge deck (Azadbakht & Yim (2016)).

Even though a gap between a beam and vertical wall was considered in the experiments performed by Chen et al. (2019) to assess impulsive forces due to wave impacts, there is no indication of the influence of the venting hole for pressure release. The small scale physical model replicated a discharge sluice in the Afsluitdijk, as seen in Figure 1.2. The investigation of venting holes applied in this particular case would provide guidance to engineers involved in the renovation project of the Afsluitdijk (Rijkswaterstaat (2015)).

2.3. Wave pressure-impulse theory

To evaluate the effects of wave impact pressures on vertical structures with overhangs, this section provides an overview of the application of wave pressure impulse theory, its main assumptions, formulation and boundary conditions. The analytical solution using conformal mapping and finite difference numerical approximations in 2D and 3D are briefly discussed.

2.3.1. General concepts

Wave breaking on structures generates local pressures over a very short time interval that resemble the shape in Figure 2.5 when recorded. For a specific point, there is an abrupt increase of pressure relative to the initial hydrostatic level up to the peak pressure p_{max}.

Although peak pressures have shown high variability for seemingly identical wave characteristics, the pressure-impulse of the impact is nearly constant (Cooker & Peregrine (1995)). Considering the local pressures as $p(x,t)$ along the time interval from t_1 to t_2, the pressure-impulse is defined mathematically as

$$P(x) = \int_{t_1}^{t_2} p(x,t)dt. \tag{2.10}$$

During wave impacts, the Reynolds number of the fluid motion is high, allowing viscosity terms to be omitted from the Navier-Stokes equation. Therefore the flow can be described with the Euler equation as

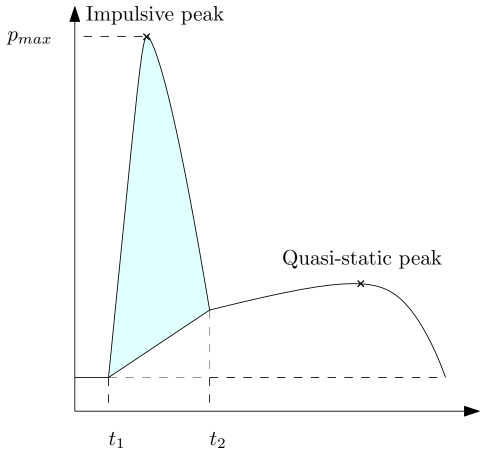

Figure 2.5: Typical wave impact pressure signal sketch (adapted from Cooker & Peregrine (1995)).

$$-\frac{1}{\rho}\nabla p = \frac{\partial \vec{u}}{\partial t} + (\vec{u}\cdot\nabla)\vec{u}, \tag{2.11}$$

where ρ is the water density and $\vec{u}$ is the velocity vector. Since the impact duration is extremely short, the fluid acceleration and induced pressure gradient terms are much greater than the nonlinear convective terms, giving

$$-\frac{1}{\rho}\nabla p = \frac{\partial \vec{u}}{\partial t}. \tag{2.12}$$

Integrating Equation 2.12 over time, and using the definition of pressure-impulse from Equation 2.10 yields

$$-\frac{1}{\rho}\nabla P = \Delta\vec{u}, \tag{2.13}$$

where $\Delta\vec{u}$ is the difference between velocities after and before the impact. For an incompressible fluid with constant density, $\nabla\vec{u} = 0$. Calculating the divergence of Equation 2.13 then leads to

$$\nabla^2 P = 0. \tag{2.14}$$

It has been demonstrated that the pressure-impulse P satisfies the Laplace equation for a given set of boundary conditions. For the problem of wave impact on a vertical structure of depth L_y and overhang of length L_o, the geometric characteristics are depicted on Figure 2.6. The free surface is horizontal and the shape of the incoming wave is considered to be unimportant for the pressure-impulse theory (Wood & Peregrine (1998)).

The boundary conditions are summarized as follows:

- Bottom boundary: no variation of normal velocity before and after the impulse at a stationary rigid boundary, $\partial P/\partial y = 0$.
- Left boundary: no variation of normal velocity before and after the impulse at a stationary rigid boundary, $\partial P/\partial x = 0$.
- Right boundary: pressure impulse dissipates and tends to zero, $P \rightarrow 0$.
- Top boundary: solid along the overhang length, where the normal derivative of the pressure-impulse is the unitary liquid approach velocity, $\partial P/\partial y = 1$. At the free surface, the pressure is constant and assumes a zero reference , $P = 0$.

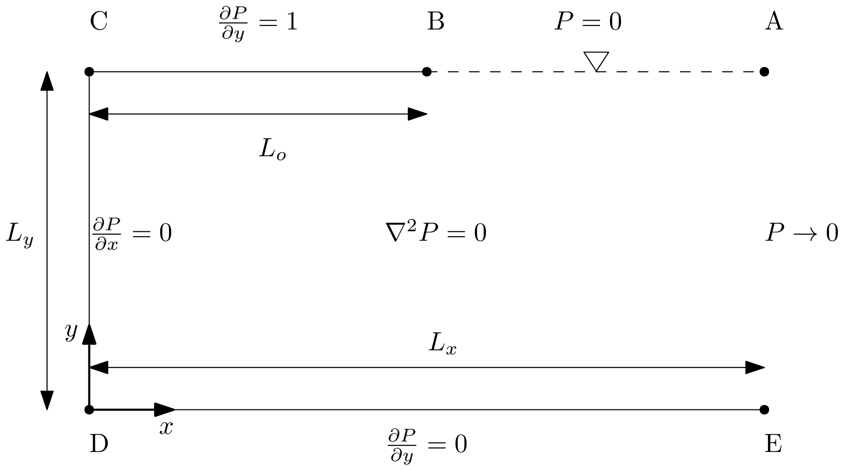

Figure 2.6: Boundary conditions and geometry of the problem to be solved (adapted from Wood & Peregrine (1996)).

Assuming a triangular pressure time series (Renzi et al. (2018)), the maximum pressure-impulse P_{max} is related to the peak pressure p_{max}, according to the equation

$$p_{max} = \frac{2P_{max}}{\Delta t}. \tag{2.15}$$

The total impulse on the wall I is defined as the integral of the pressure-impulse over the wall height:

$$I = \int_0^{L_y} P dy. \tag{2.16}$$

The pressure-impulse P obtained by the mathematical model is dimensionless. For practical applications, the conversion to the dimensional $\overline{P}$ is required using the relationship:

$$\overline{P}(\bar{x}, \bar{y}) = \rho U L_o P(Lx, Ly), \tag{2.17}$$

where U is the vertical wave impact velocity to be measured or estimated. All other variables are known.

2.3.2. Analytical solution

A general analytical solution for the Laplace Equation 2.14 subject to the boundary conditions described on section 2.3.1 has been proposed by Wood & Peregrine (1996). Since there is a singularity problem at point B, three conformal maps are required to transform the original problem:

1. $w = u + iv = \cosh(\pi z / L_y)$, where z is the original plane from Figure 2.6.
2. $h = f + ig = Mw + N$, where $M = 2/(\cosh(\pi/L_y) - 1)$ and $N = M + 1$.
3. $\zeta = \xi + i\eta = L_y \cosh^{-1}(h)/\pi$, generating the ζ-plane shown in Figure 2.7.

Solving by separation of variables, the analytical expressions for the pressure-impulse become

$$P = \sum_{n=1}^{\infty} A e^{-\alpha_n \xi} \cos(\alpha_n \eta), \tag{2.18}$$

$$A = \frac{2}{\alpha_n L_y} \int_0^{L_y} \frac{1}{M} \frac{\sin(\pi\eta/L_y)\cos(\alpha_n \eta)}{\sqrt{b^2 - 1}} d\eta, \tag{2.19}$$

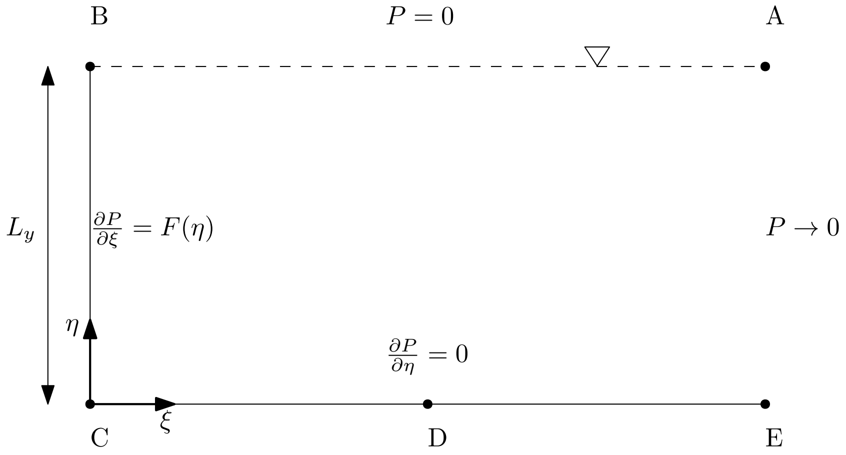

Figure 2.7: New boundary conditions of the problem after conformal mapping (adapted from Wood & Peregrine (1996)).

where $\alpha_n = (n + 1/2)/\pi/L_y$ and $b = (\cos(\pi\eta/L_y$[1]$) - N)/M$.

Figure 2.8 demonstrates an example of pressure-impulse contours for depth $L_y = 2.0$ and overhang length $L = 1.0$, determined by the analytical solution. It can be noted that the pressure-impulse increases gradually towards the vertical wall and that the largest values are concentrated at the corner between the overhanging element and vertical structure.

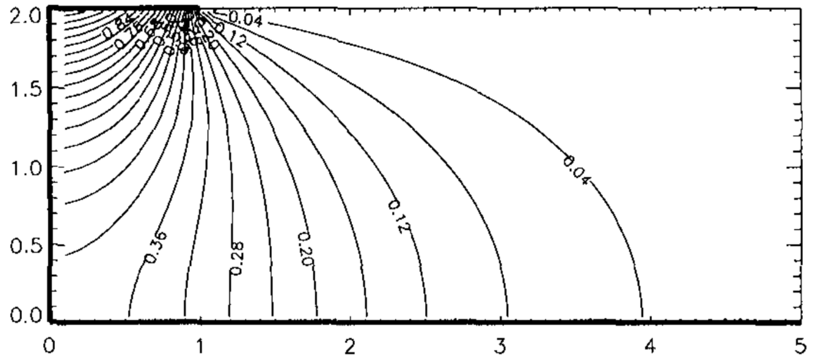

Figure 2.8: Pressure-impulse contours from analytical solution, for $L_y = 2.0$ (Wood & Peregrine (1996)).

2.3.3. Numerical solution

To solve the wave pressure-impulse problem described in 2.3.1, a numerical routine has been implemented by Hofland et al. (2019). The mathematical model is discretized into an $N \times M$ rectangular grid with $\Delta x = \Delta y$, as shown in Figure 2.9 below.

The 2D Laplace equation 2.14 is then approximated using a second order central difference relaxation scheme, so it can be rewritten for each K_{th} iteration in the form:

$$P_{i,j}^{K} = \frac{\Delta y^2 \left(P_{i+1,j}^{K-1} + P_{i-1,j}^{K-1}\right) + \Delta x^2 \left(P_{i,j+1}^{K-1} + P_{i,j-1}^{K-1}\right)}{2(\Delta x^2 + \Delta y^2)}, \qquad (2.20)$$

for $2 < j < N - 1$ and $2 < i < M - 1$. The boundary conditions are set as:

- Bottom boundary: $P_{1,j}^{K} = P_{2,j}^{K}$.

---

[1] The divisor L_y was added to provide consistent results with the literature.

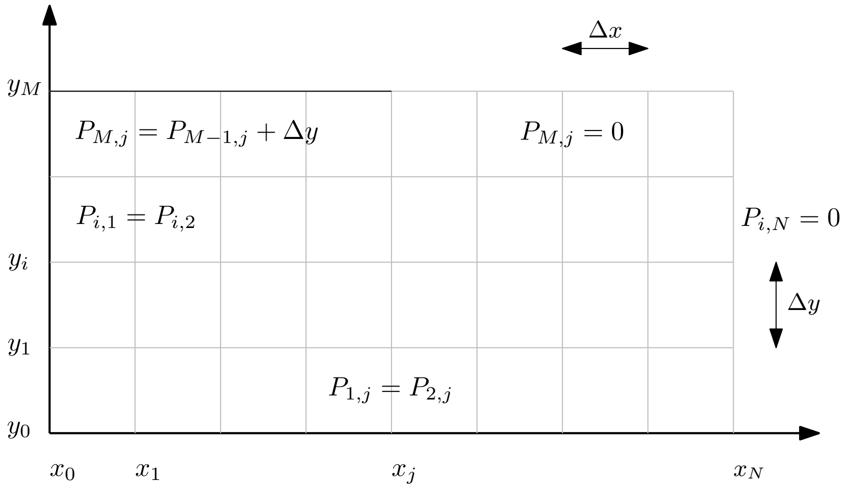

Figure 2.9: Discretized 2D numerical grid and boundary conditions.

- Left boundary: $P^K_{i,1} = P^K_{i,2}$.
- Right boundary: $P^K_{i,N} = 0$.
- Top boundary: $P^K_{M,j} = P^K_{M-1,j} + \Delta y$ along the overhang length.
- Top boundary: $P^K_{M,j} = 0$ at free surface.

Similarly, the numerical algorithm was expanded to approximate the 3D Laplace equation, to consider not only variations in overhang length, but also width. Using the 3D finite difference scheme from Onabid (2012), the numerical approximation is defined as

$$P^K_{i,j,k} = P^{K-1}_{i,j,k} + \frac{\Delta t}{\Delta^2}\left(P^{K-1}_{i+1,j,k} + P^{K-1}_{i-1,j,k} + P^{K-1}_{i,j+1,k} + P^{K-1}_{i,j-1,k} + P^{K-1}_{i,j,k+1} + P^{K-1}_{i,j,k-1} - 6P^{K-1}_{i,j,k}\right), \tag{2.21}$$

where $\Delta t = \Delta^2/6$ and $\Delta = \Delta x = \Delta y = \Delta z$. The boundary conditions at the $N \times M \times O$ grid then become:

- Bottom boundary: $P^K_{i,j,1} = P^K_{i,j,2}$.
- Left boundary: $P^K_{i,1,k} = P^K_{i,2,k}$.
- Right boundary: $P^K_{i,M,k} = P^K_{i,M-1,k}$.
- Far boundary: $P^K_{N,j,k} = 0$.
- Top boundary: $P^K_{i,j,O} = P^K_{i,j,O-1} + \Delta z$ along the overhang length.
- Top boundary: $P^K_{i,j,O} = 0$ at free surface.
- Wall boundary: $P^K_{1,j,k} = P^K_{2,j,k}$.

The 3D solution with modified top boundary condition along the venting holes represents an interesting tool to account for pressure-impulse loss due to ventilations.

2.4. Vertical impact velocity prediction

To apply the pressure-impulse theory for the case of a vertical structure with overhang, it is required to estimate the vertical particle velocity at the moment of impact underneath the horizontal surface. Three wave stading theories are explored in this section.

The most simple method to determine the vertical wave velocity is through Linear or Airy Wave Theory. It consists of a first order description, where the wave is represented by a simple sine function. However, this approximation will probably not be very accurate for surface velocities, especially outside the applicability range of $h_s/gT^2 > 0.02$ and $H_i/gT^2 > 0.001$ (Schiereck (1996)). For a velocity potential Φ, the vertical velocity $U = \partial\Phi/\partial y$ is obtained as

$$U = \frac{\pi H_i}{T}\frac{\sinh(k(y+h_s))}{\sinh(kh_s)}\sin(kx-\omega t), \tag{2.22}$$

where $\omega = 2\pi/T$ represents the angular frequency. The expression above still holds for standing waves by doubling the wave height under the full reflection assumption (Holthuijsen (2009)).

For engineering applications related to wave impacts, however, more advanced wave theories may be used. Broughton & Horn (1987), for instance, developed a prediction method for vertical wave impact forces at the underside of a deck, which required estimation of the wave celerity using Stoke's 5th Order Theory. For standing waves, Sobey (2009) developed a Stokes-style analytical theory up to 5th order valid for the range $0.1 < \omega^2 H_i/g < 1.5$ and $0.6 < \omega^2 h_s/g < 4.0$. The vertical wave velocity is provided through

$$U = k(g/k^3)^{1/2}\sum_{i=1}^{N}\epsilon^i\sum_{j=0}^{i}\sum_{m=0}^{i} jA_{i,j,m}\frac{\sinh(jk(h_s+y))}{\cosh(jkh_s)}\cos(jkx)\sin(m\omega t), \tag{2.23}$$

where the coefficients $A_{i,j,m}$ are expanded to order $N = 3$ with:

$$\begin{aligned}
q &= \tanh(kh_s);\\
\epsilon &= kH_i;\\
A_{1,1,1} &= -1/\sqrt{q};\\
A_{2,2,2} &= \frac{3}{16}\frac{-1+q^4}{q^{7/2}};\\
A_{2,0,2} &= \frac{1}{16}\frac{1+3q^2}{q^{3/2}};\\
A_{3,1,3} &= -\frac{1}{256}\frac{31q^4-62q^2-9}{q^{9/2}};\\
A_{3,1,1} &= \frac{1}{256}\frac{6q^{10}+11q^8-63q^6+96q^4+27q^2+27}{q^{13/2}};\\
A_{3,3,3} &= -\frac{1}{256}\frac{39q^6-53q^4+5q^2+9}{q^{13/2}};\\
A_{3,3,1} &= -\frac{1}{256}\frac{6q^8-13q^6-5q^4+9q^2+3}{q^{9/2}}.
\end{aligned}$$

Tadjbakhsh & Keller (1960) developed a relatively simple theory to describe standing surface waves of finite amplitude. The motion is determined to third order as a function of the amplitude a divided by the wavelength L_w. The vertical velocity U is given by

$$U = \frac{1}{8}\left((\omega_0^2-\omega_0^{-2})+(\omega_0^{-2}-3\omega_0^{-6})\cos(2t)\right)\cos(2x), \tag{2.24}$$

where $w_0 = \sqrt{\tanh(kh_s)}$.

A comparison of the maximum vertical wave velocities estimated by the three standing wave theories is depicted in Figure 2.10. The results are shown as a function of the product between wave number and amplitude ka and the product between wave number and water depth kh_s. The range of variation is based on the dimensionless water depth validity $\omega^2 h_s/g$, as suggested by Sobey (2009).

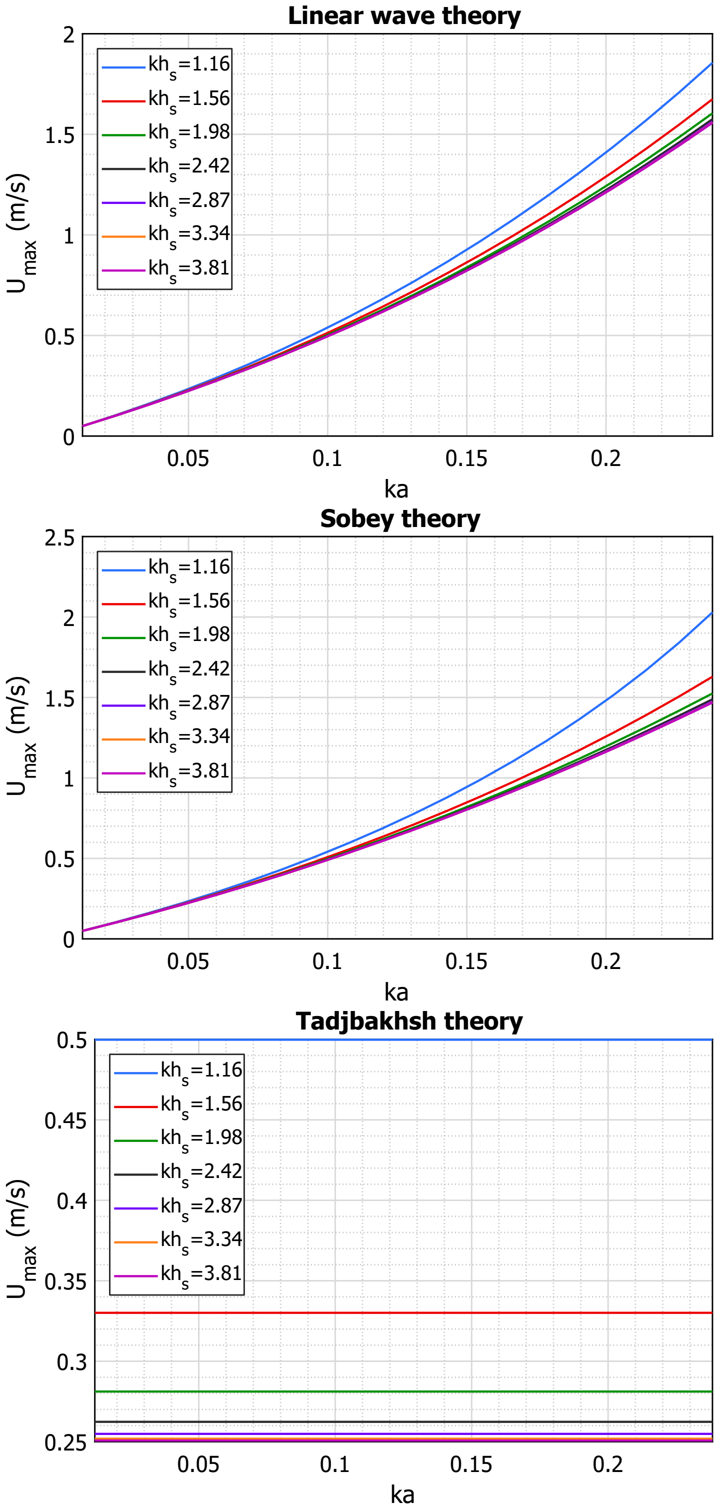

Figure 2.10: Maximum vertical velocities as described by the linear, Sobey and Tadjbakhsh standing wave theories.

3

Pressure-impulse modelling

In this chapter, the theoretical pressure-impulse model is applied to evaluate the effects of ventilations on vertical structures with overhangs subject to upward wave impacts. First, the numerical model in two dimensions is validated against the analytical method through a grid refinement study. Subsequently, openings are included in the model to assess two study cases and their variations, for two and three dimensions. Finally, the influence of ventilation and geometrical parameters to release pressure-impulses are investigated.

3.1. Grid refinement study

Pressure-impulse results are obtained using the analytical and 2D numerical solutions discussed in Sub-sections 2.3.2 and 2.3.3. The distributions of pressure-impulse are evaluated for wave impacts beneath structures with unitary overhang length $L_o = 1.0$, which is the chosen scaling parameter for 2D assessments. For the cases of dimensionless wall heights $L_y = 2.0$, $L_y = 1.0$ and $L_y = 0.5$, the analytical and numerical results are compared for validation. These are the same cases considered by Wood & Peregrine (1996). The domain length L_x is set to the maximum between $4L_y$ and $4L_o$ in all cases to guarantee $P \to 0$ at the right boundary condition shown in Figure 2.6.

To solve the Laplace Equation analytically using conformal mapping, the sum in Equation 2.18 is taken to thirty terms and numerical integration determines the coefficient of Equation 2.19. In this section, the influence of ventilations for pressure relieve is not yet examined. Next, the iteration and grid size effects related to the numerical method are shown.

3.1.1. Iteration effects

The accuracy of the results provided by the finite difference scheme of Equation 2.20 is highly dependent on the total number of iterations K, since the value of the pressure-impulse $P_{i,j}$ is updated under an iterative process until convergence is reached.

The average difference dP of the pressure-impulse values between iterations tends to zero as the total number of iterations increases. The numerical solution is considered to converge when $dP < tol$, where tol is a tolerance value, small enough so that more iterations would lead to insignificant changes on the final results. Numerical experiments demonstrated that $tol = 10^{-9}$ is appropriate for a precision of two decimal places, since dP rapidly decreases for iterations beyond this threshold (see Figure 3.1).

Figure 3.2 depicts the influence of the number of iterations until convergence on the pressure-impulse results for wall heights $L_y = 2.0$, $L_y = 1.0$ and $L_y = 0.5$, with spatial steps $\Delta x = \Delta y = 0.01$. The results are compared with the analytical solution. It can be noticed that the convergence in general approximates the numerical solution to the analytical. Also, larger domains need more iterations to converge. To further increase the number of iterations has proven to be ineffective to decrease the error of the numerical solution. Instead, the error remains approximately constant due to very small

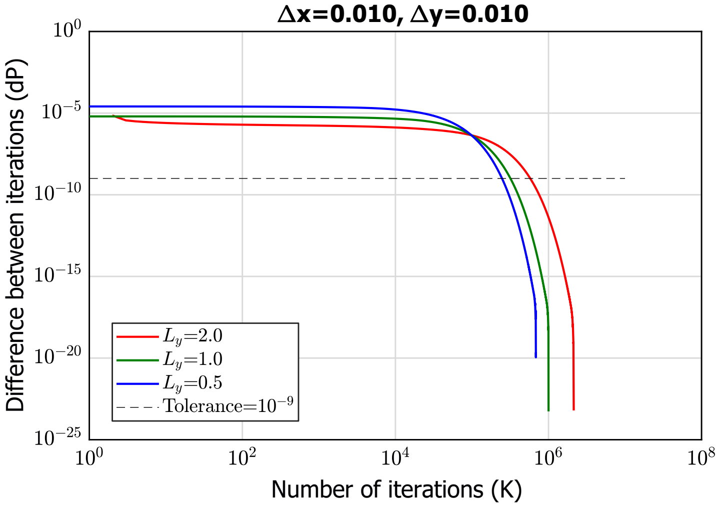

Figure 3.1: Pressure-impulse changes between iterations for $L_y = 2.0$, $L_y = 1.0$ and $L_y = 0.5$ with $\Delta x = \Delta y = 0.01$.

changes between iterations. Therefore, the effects of the grid size are also investigated.

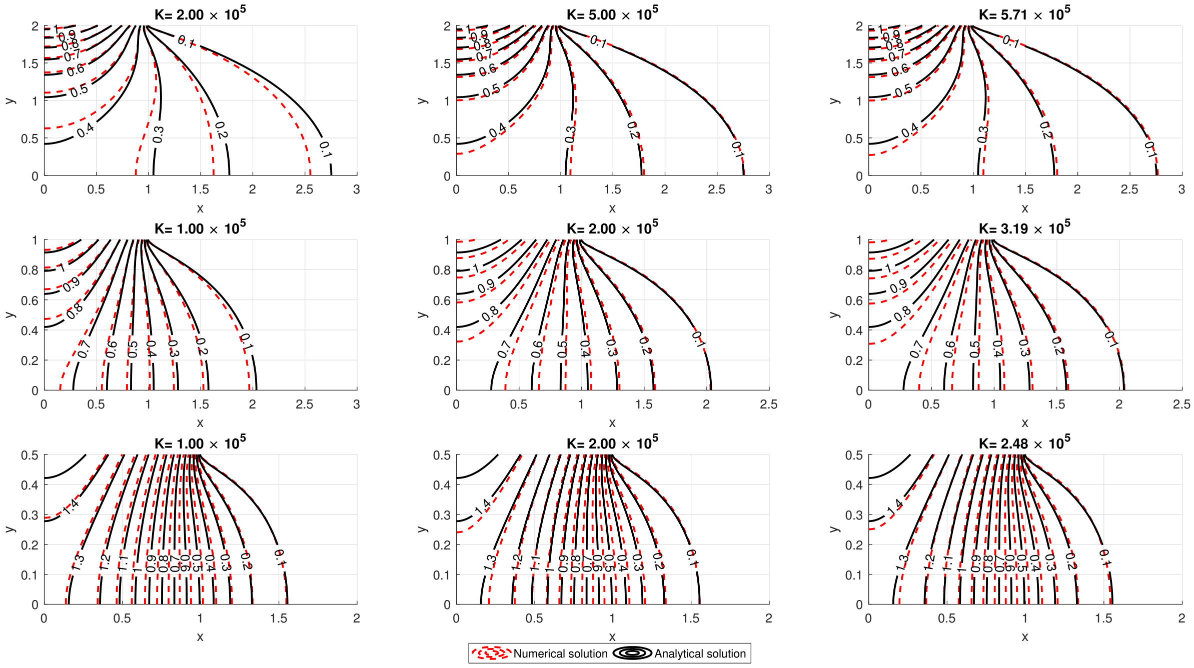

Figure 3.2: Effects of the number of iterations K for $L_y = 2.0$, $L_y = 1.0$ and $L_y = 0.5$ with $\Delta x = \Delta y = 0.01$.

3.1.2. Grid size effects due to structure dimensions

The numerical model performance for each grid size is evaluated based on the relative error compared to the analytical solution, defined as the average of differences between the numerical and analytical solutions. After convergence is reached, the error is determined for grid sizes $\Delta x = \Delta y = 0.100$, 0.050, 0.010, 0.005 and 0.0025 with $L_y = 2.0$, $L_y = 1.0$ and $L_y = 0.5$. These spatial step values are derived from dividing $L_o = 1.0$ by a factor F into 10, 20, 100, 200 and 400 equally spaced elements, respectively. Since the grid is composed by $N \times M$ points, the number of elements associated to refinements along a dimension is directly proportional to the square of the total number of elements, which greatly increases the required computing time.

Table 3.1 compares the computed relative errors, showing that the numerical results become more accurate for finer grids and that the optimal grid size is dependent on the geometry of the problem. For instance, pressure-impulses obtained for $L_y = 2.0$ with $\Delta x = \Delta y = 0.050$ are much more accurate than for $L_y = 0.5$ with $\Delta x = \Delta y = 0.025$. This implies that the smallest dimension between L_o and L_y should be the reference to determine optimal grid sizes. The expression to optimize spatial steps without ventilation then becomes

$$\Delta x = \Delta y = \frac{\min(L_o, L_y)}{F}, \tag{3.1}$$

where $F \geq 200$ produces precise results within 2% relative error. The pressure-impulse values estimated using $F \leq 20$ are not reliable due to the high relative errors reported. Figure 3.3 shows the optimized numerical results compared to the analytical solutions for $L_y = 2.0$, $L_y = 1.0$ and $L_y = 0.5$.

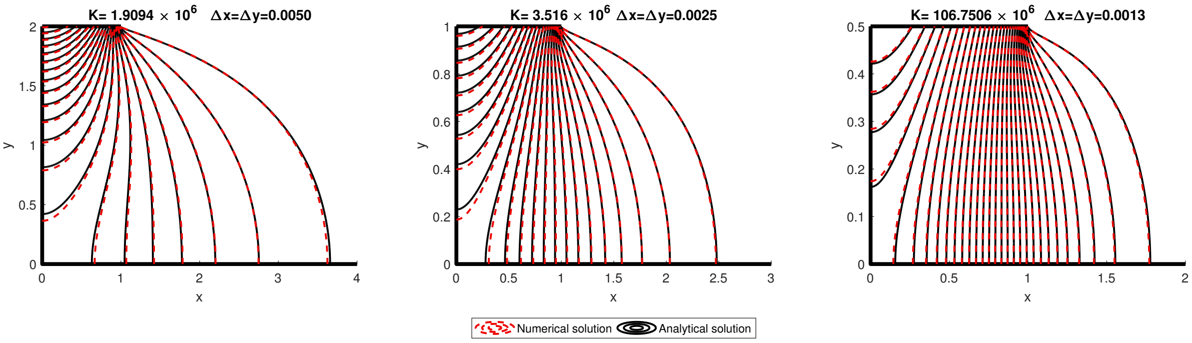

Figure 3.3: Comparison of analytical (black) and numerical (red) solutions for $L_y = 2.0$, $L_y = 1.0$ and $L_y = 0.5$ after grid refinement.

Table 3.1: Computed pressure-impulse errors between numerical and analytical solutions.

$L_y = 2.0$			
$\Delta x = \Delta y$	Iteration cycles	Absolute error	Relative error (%)
0.1000	8351	0.0164	15.93%
0.0500	31463	0.0089	8.62%
0.0100	571420	0.0018	1.76%
0.0050	1909400	0.0002	0.14%
$L_y = 1.0$			
$\Delta x = \Delta y$	Iteration cycles	Absolute error	Relative error (%)
0.1000	4397	0.0907	39.29%
0.0500	16756	0.0425	18.40%
0.0100	319080	0.0078	3.39%
0.0050	1079200	0.0033	1.41%
0.0025	3516000	0.0005	0.21%
$L_y = 0.5$			
$\Delta x = \Delta y$	Iteration cycles	Absolute error	Relative error (%)
0.0500	13030	0.2834	47.43%
0.0100	248250	0.0435	7.28%
0.0050	855690	0.0186	1.86%
0.0025	2874600	0.0060	1.00%
0.0013	106750594	0.0048	0.80%

3.1.3. Grid size effects due to venting dimensions

By replacing the top boundary condition along the horizontal overhang with a free surface condition, openings of length L_h can be introduced to the problem to simulate venting holes. The opening is located at the corner where the vertical wall and the overhang meet, since this is the point of maximum pressure-impulse.

The influence of the grid size with $\Delta x = \Delta y = 0.0050$, 0.0033, 0.0025 and 0.0020 is tested for a case of $L_h = 0.05$ and $L_o = L_y = 1.00$. As depicted in Figure 3.4, the pressure-impulse contours for each grid size become more distinct in the region near the gap. The ventilation influence on pressure-impulse results is considered insensitive to changes for spatial steps 10 times smaller than the opening length, due to absolute differences of the maximum pressure-impulses at wall in the order of 10^{-2} between this grid size and more refined grids. Consequently, the optimal spatial step considering ventilations is given by the smallest $\Delta x = \Delta y$ between $L_h/10$ and Equation 3.1.

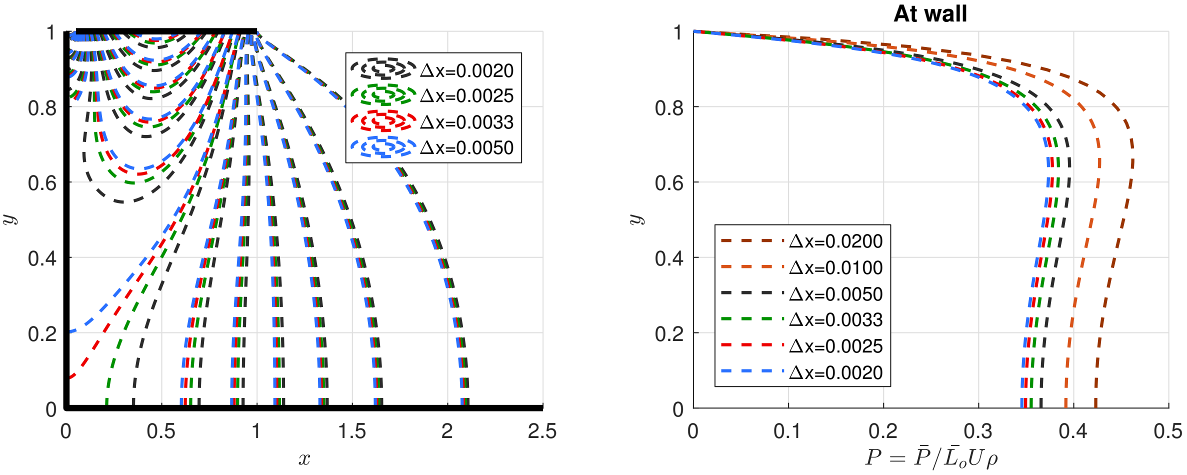

Figure 3.4: Influence of the grid size for a venting hole with $L_h = 0.05$ on the pressure-impulse contours (left) and at wall (right).

3.2. Ventilation assessment

The numerical solutions for the 2D and 3D Laplace equation are employed to assess the pressure-impulse release due to wave impacts on vertical structures with overhangs using ventilations. To ensure high quality of the results, the insights from the 2D solution concerning number of iterations and grid refinement are applied also in 3D. In this section, the conceptual pressure-impulse model is applied to two small-scale reference cases, named Case 1 and Case 2. Both cases are also studied at later stages under wave impacts using computational fluid dynamics and physical modelling tests. Case 1 represents impacts on a vertical wall 60 cm high with a 10 cm long overhang and 1 cm long venting hole. Case 2 refers to a vertical wall 60 cm high with a 20 cm long overhang, 1 and 2 cm long venting holes. The scaled geometrical dimensions of each case are depicted in Figure 3.5.

3.2.1. Study cases in 2D

In the 2D ventilation assessment using the pressure-impulse numerical model, it is assumed that the wave impact covers evenly the entire overhang length, both the domain and ventilation widths are infinitely large and the water depth is level with the wall height. Case 1 is examined for two scenarios: no venting (Case 1a) and 1 *cm* venting (Case 1b). Case 2 is examined for three scenarios: no venting (Case 2a), 1 *cm* venting (Case 2b) and 2 *cm* venting (Case 2c). The dimensionless equivalent parameters L_y, and L_o and L_h are derived for both cases by dividing all geometrical dimensions by their corresponding overhang lengths, as demonstrated in Table 3.2.

Following the recommendations from Section 3.1, the spatial step was defined as $\Delta x = \Delta y = L_o/200 = 0.005$. This grid refinement is appropriate for the venting hole lengths since $\Delta x \leq L_h/10$ holds for all cases.

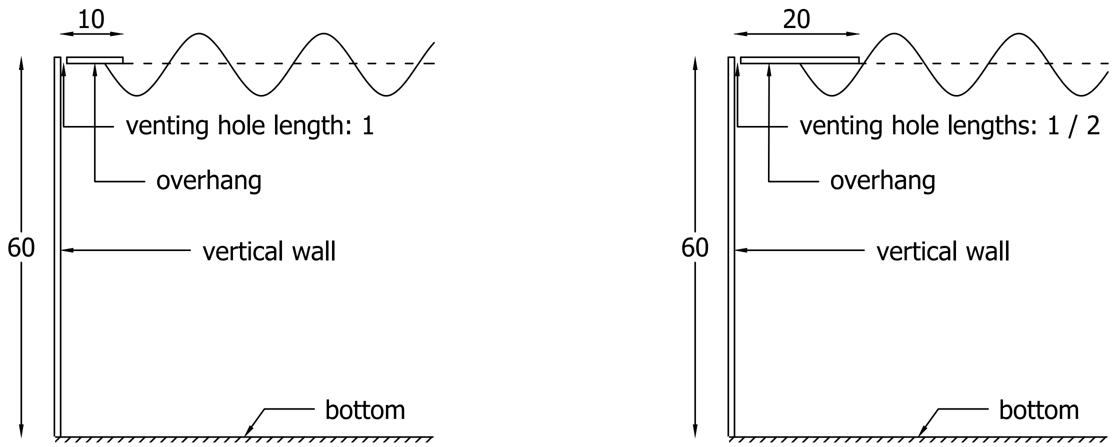

Figure 3.5: Geometrical characteristics of Case 1 (left) and Case 2 (right). All dimensions are in cm.

Table 3.2: Geometrical parameters considered in the 2D simulations for all cases.

Case	$\overline{L_o}$ (cm)	$\overline{L_y}$ (cm)	$\overline{L_h}$ (cm)	L_o	L_y	L_h
1a	10.00	60.00	—	1.00	6.00	—
1b	10.00	60.00	1.00	1.00	6.00	0.10
2a	20.00	60.00	—	1.00	3.00	—
2b	20.00	60.00	1.00	1.00	3.00	0.05
2c	20.00	60.00	2.00	1.00	3.00	0.10

The numerical results for Cases 1 and 2 are summarized on Figures 3.6, 3.7, 3.8 and 3.9. At wall, the analytical and numerical solutions without openings are identical for Case 2 and present good agreement for Case 1, which further validates the numerical results for these model dimensions.

In Figure 3.6, the decrease of dimensionless pressure-impulse with venting of $L_h = 0.1$ is evident in comparison to the situation without venting. There is a significant decrease not only in the maximum pressure-impulse values, but also in the distance away from the vertical wall that is affected by the impact.

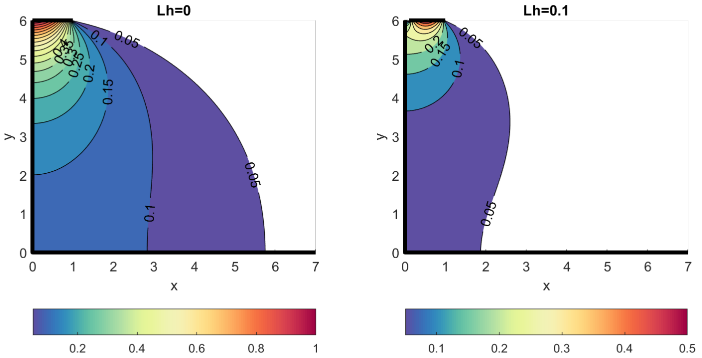

Figure 3.6: Pressure-impulse contours for Cases 1a and 1b.

Figure 3.7 illustrates the influence of venting towards pressure-impulses along the wall. It can be noticed that, when $L_h = 0$, the pressure-impulse gradually increases from the bottom of the wall up to $P = 1$ at the top. In contrast, when $L_h = 0.10$, the pressure-impulse starts reduced at the bottom, slight increases up to approximately $y = 5.7$ and becomes zero at the top of the wall.

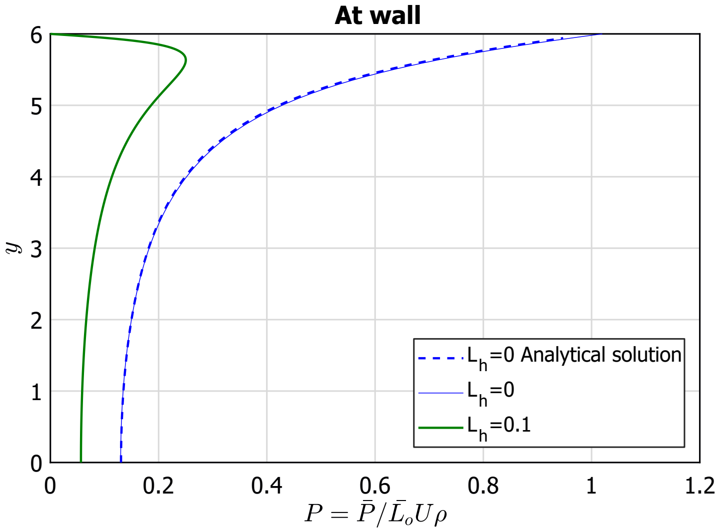

Figure 3.7: Comparison between pressure-impulses from Cases 1a and 1b at the vertical wall.

A similar trend is observed for Case 2, with smaller relative wall height L_y. Figure 3.8 shows the effects of venting on the pressure-impulse contours. The reduction is more intense for the longer venting with $L_h = 0.10$ compared to $L_h = 0.05$.

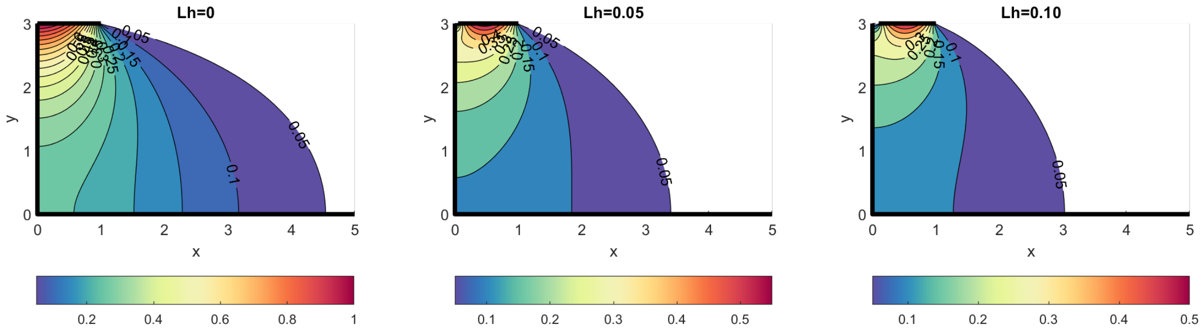

Figure 3.8: Pressure-impulse contours for Cases 2a, 2b and 2c.

Along the wall height, Figure 3.9 indicates that the relative change between venting hole sizes is much smaller than the difference between no venting ($L_h = 0$) and the smaller venting size ($L_h = 0.10$).

The opening in Case 1 was sufficient to dissipate the pressure-impulse completely before reaching the bottom, since the depth to overhang length ratio is large. The reduction of maximum pressure-impulse in Case 1 caused by 1 cm of ventilation, or 10% of the overhang length, is 79%. As a matter of comparison, the same ratio of ventilation by overhang length for Case 2 reduced the pressure-impulse by 75%. The maximum pressure-impulse, total impulse at wall and release due to ventilations for both cases are indicated at Table 3.3.

3.2.2. Study cases in 3D

To examine the influence of ventilations in three dimensions using the conceptual pressure-impulse model, three new parameters are introduced to the problem: the domain width W, the ventilation width W_h and the spacing between venting holes S, which is exactly the double of W. For consistency, the overhang length L_o remains the unitary scaling parameter. These parameters are represented in Figure 3.10.

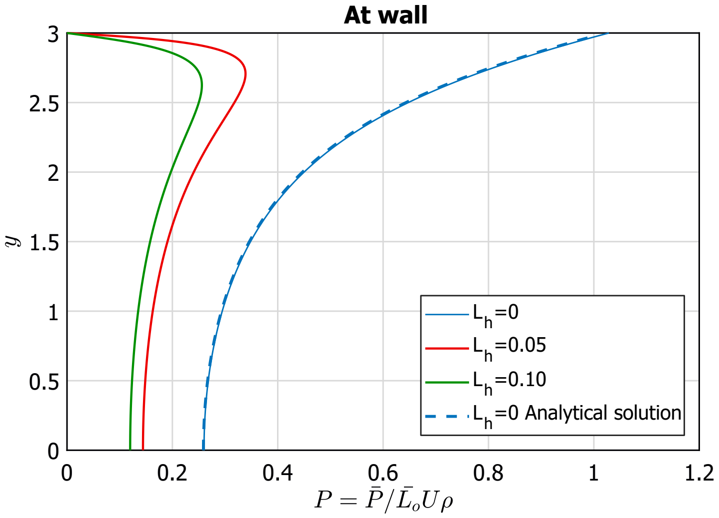

Figure 3.9: Comparison between pressure-impulses from Cases 2a, 2b and 2c at the vertical wall.

Table 3.3: Maximum pressure-impulses, total impulse at wall and their reductions due to ventilations for Cases 1 and 2 from 2D simulations.

Case	P_{max}	R_P	I	R_I
1a	1.02	—	1.64	—
1b	0.25	75%	0.64	61%
2a	1.03	—	1.31	—
2b	0.34	67%	0.63	52%
2c	0.26	75%	0.50	62%

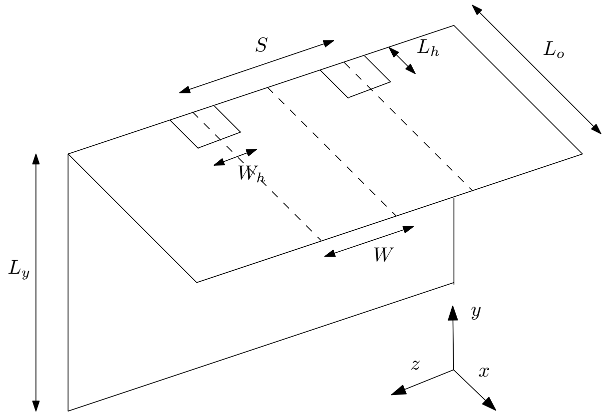

Figure 3.10: Parameters considered in the 3D simulations.

The width of the wave crest that collides with the overhang is considered to be infinitely long, a reasonable assumption for long-crested waves. The wave impact is assumed to occur homogeneously along the overhang length and width. For Cases 1 and 2, the dimensional width of the model is 80 cm and the width of the ventilation is the same as the length. All the employed dimensional and dimensionless parameters are summarized in Table 3.4. The values are identical to the 2D cases, with the inclusion of parameters related to the width of the domain, in the z direction.

The spatial steps considered in the 3D simulation are $\Delta x = \Delta y = \Delta z = L_o/100 = 0.010$ and $L_o/200 = 0.005$. Finer grid sizes could not be achieved due to computational constraints. To accelerate the convergence of the finite difference model in 3D, the simulation started with a coarse grid refinement, which provided preliminary pressure-impulse values to be used in progressively finer grids through

Table 3.4: Geometrical parameters considered in the 3D simulations for all cases.

Case	$\overline{L_o}$ (cm)	$\overline{L_y}$ (cm)	$\overline{W}$ (cm)	$\overline{L_h}$ (cm)	$\overline{W_h}$ (cm)	L_o	L_y	W	L_h	W_h
1a	10.00	60.00	80.00	—	—	1.00	6.00	8.00	—	—
1b	10.00	60.00	80.00	1.00	1.00	1.00	6.00	8.00	0.10	0.10
2a	20.00	60.00	80.00	—	—	1.00	3.00	4.00	—	—
2b	20.00	60.00	80.00	1.00	1.00	1.00	3.00	4.00	0.05	0.05
2c	20.00	60.00	80.00	2.00	2.00	1.00	3.00	4.00	0.10	0.10

interpolation, until the adopted grid is reached.

The results from 3D modelling of pressure-impulse for all cases are shown next.

Figures 3.11 and 3.12 depict the three-dimensional aspect of the problem. It can be observed that there is a local release of pressure-impulses where the venting is located. Apart from this localized effect, no other conclusions can be made in this representation. To detect more nuanced changes, side and front slices of the problem are examined.

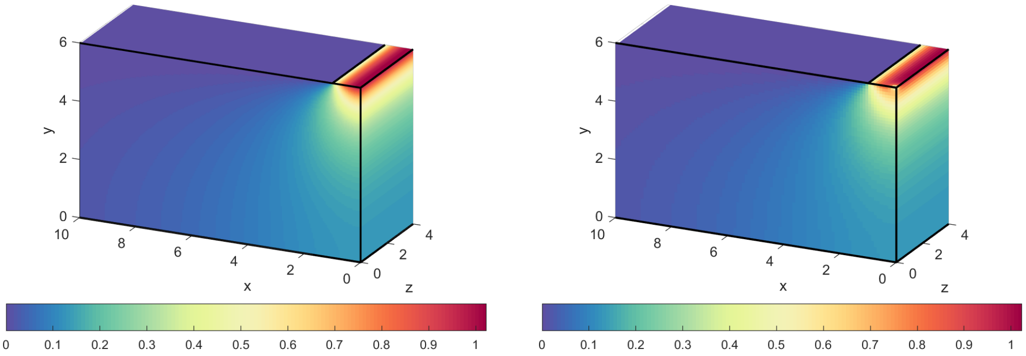

Figure 3.11: 3D view of Cases 1a (left) and 1b (right).

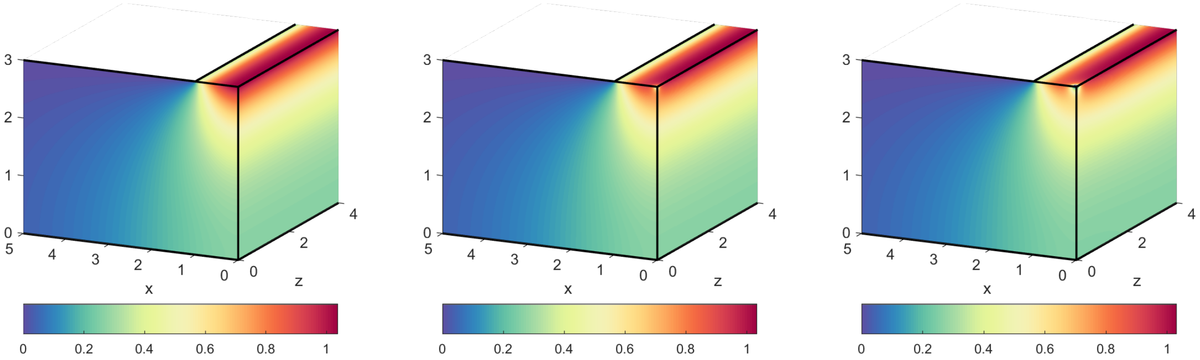

Figure 3.12: 3D view of pressure-impulse contours for Cases 2a (left), 2b (middle) and 2c (right).

The sideways comparison of pressure-impulses shown in Figures 3.13 and 3.14 reflects how the maximum values are concentrated at the corner between the wall and overhang for the cases without openings. However, when ventilations are present, the maximum pressure-impulse shifts to the region under the deck, reducing the loadings at the vertical wall. A similar effect was found in the 2D simulations, but with much larger intensity. At the sections located in the end of the domain width, away from the venting hole, the pressure-impulses become practically the same as the situation without ventilation. This indicates that the spacing between ventilations is large enough to completely dissipate the release effects of venting. The role of spacing and domain width on the model results are treated with more depth in Section 3.3.2.

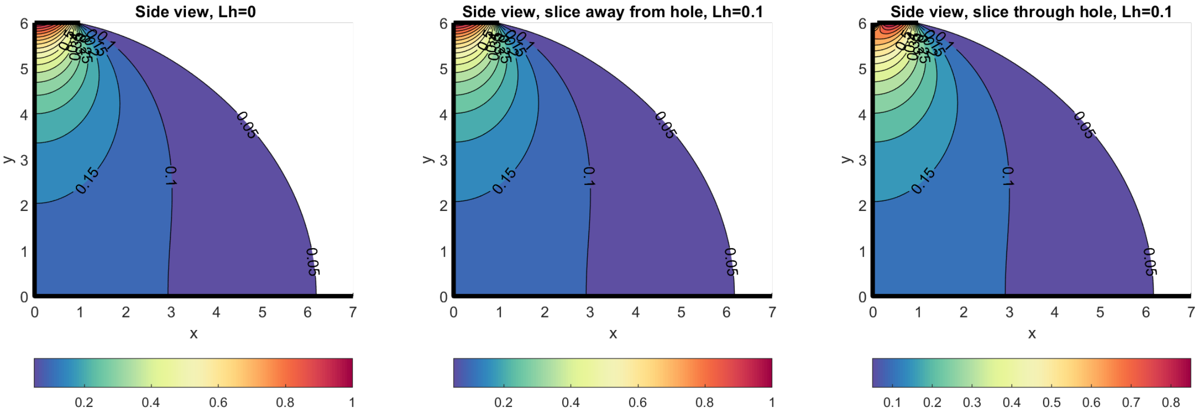

Figure 3.13: Side view of pressure-impulse contours for Cases 1a (left) and 1b (middle and right).

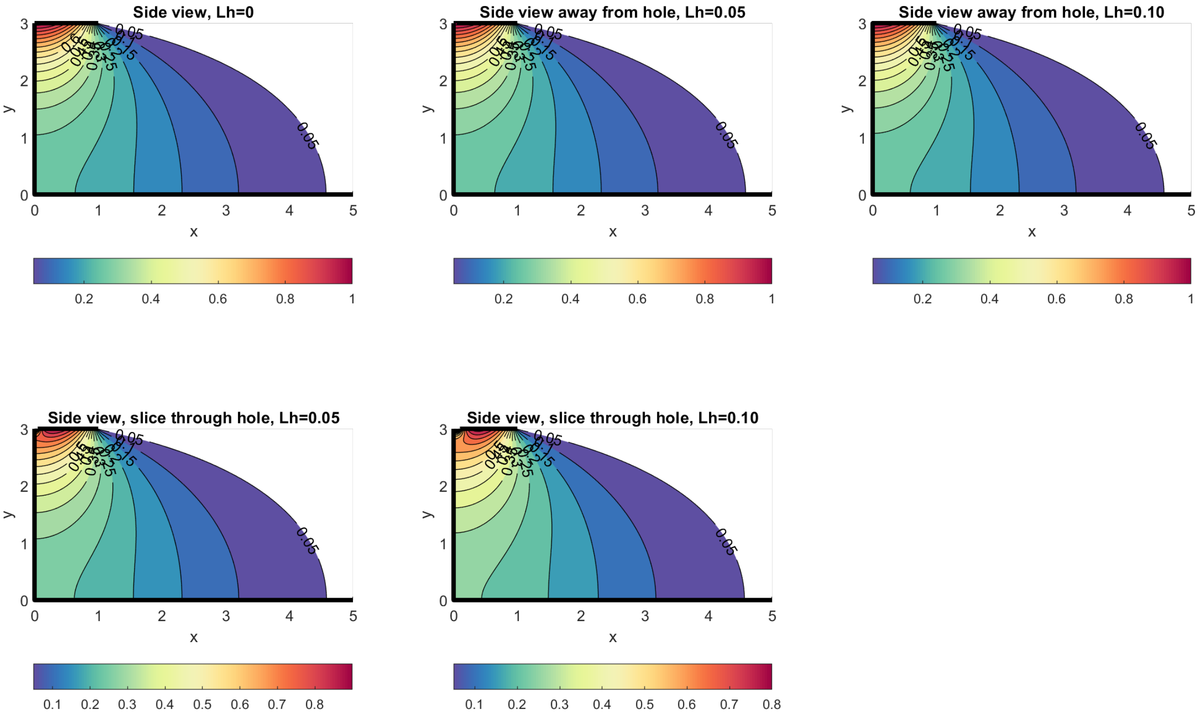

Figure 3.14: Side view of pressure-impulse contours for Cases 2a (top left), 2b (top middle and bottom left) and 2c (top right and bottom right).

This localized venting effect is also evident from Figures 3.15 and 3.16, which represent the front view of the pressure-impulses affecting the structure. To effectively reduce wave impacts, multiple openings, larger venting areas or reduced spacing are required.

Figure 3.17 illustrates the distribution of pressure-impulses along the wall, for both Cases 1 and 2. Cases with venting always have zero pressure-impulse at the top, due to the adopted free surface boundary condition at this location. Compared to the simulations in 2D, the reduction in pressure-impulse due to venting is much inferior and mostly apply to the top of the wall, near the overhang where the impact occurs. The pressure-impulse release is more prevalent in the situation with shorter relative wall height ($L_y = 3$).

Figure 3.18 compares the results from 2D and 3D simulations at wall. Simulations with $W_h = W$ was

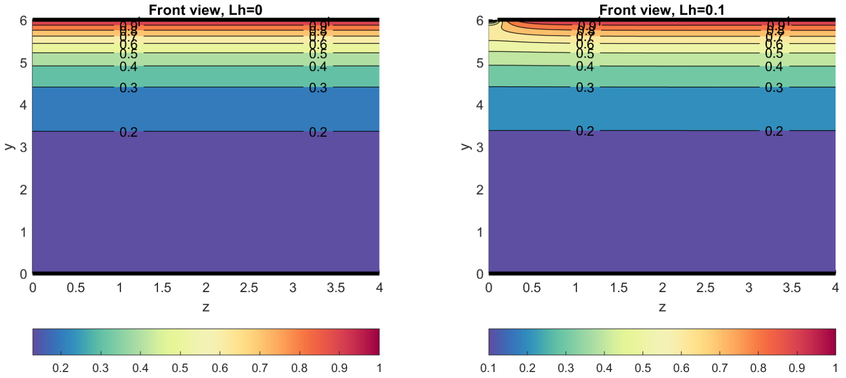

Figure 3.15: Front view of pressure-impulse contours for Cases 1a (left) and 1b (right).

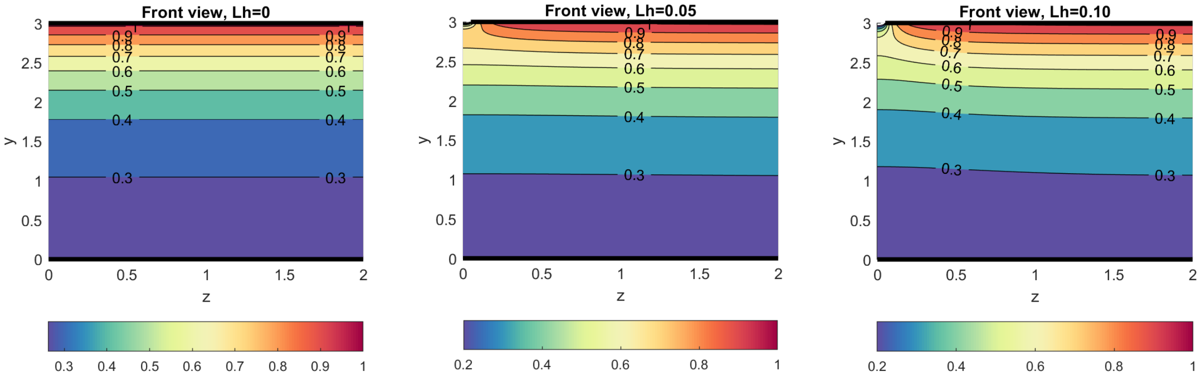

Figure 3.16: Front view of pressure-impulse contours for Cases 2a (left), 2b (middle) and 2c (right).

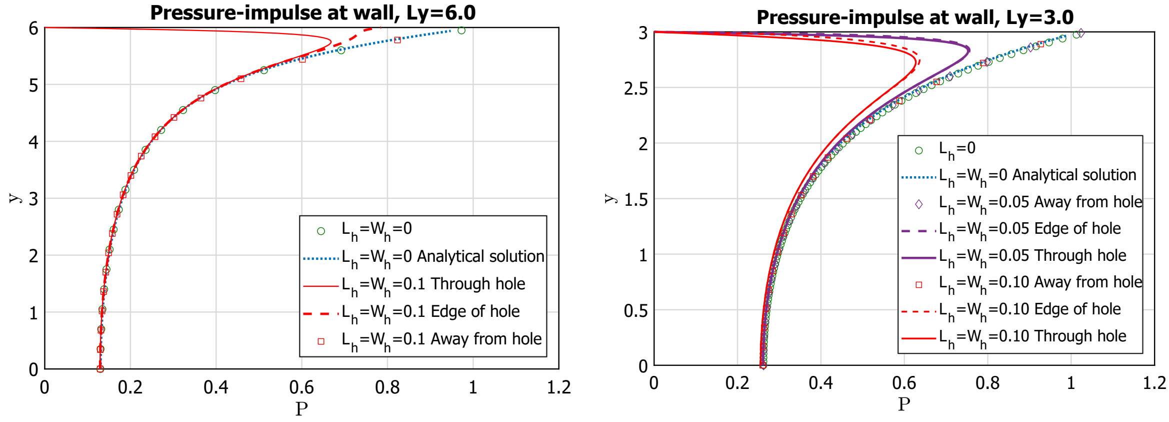

Figure 3.17: Comparison between pressure-impulses from Cases 1 (left) and 2 (right) at the vertical wall.

performed in 3D for Case 1b and 2c to test how the pressure-impulses in 3D would correlate to the 2D results. The outcome implies that 2D simulations with gaps are approximately equivalent to 3D simulations with venting across the entire domain in the z direction. Therefore only two dimensions are not sufficient to assess variations of the venting width W_h or the spacing S between ventings. Three dimensions are required to correctly assess venting hole effects.

Table 3.5 indicates the maximum pressure-impulse and the total impulse on the wall, at the section through holes in the cases where ventilations are present. P_{max} and P_{maxh} refer to the sections away and through the venting hole, respectively. Even though the values are very close without ventilations (Cases 1a and 2a), the reduction of maximum pressure-impulse and total impulse due to venting are very distinct.

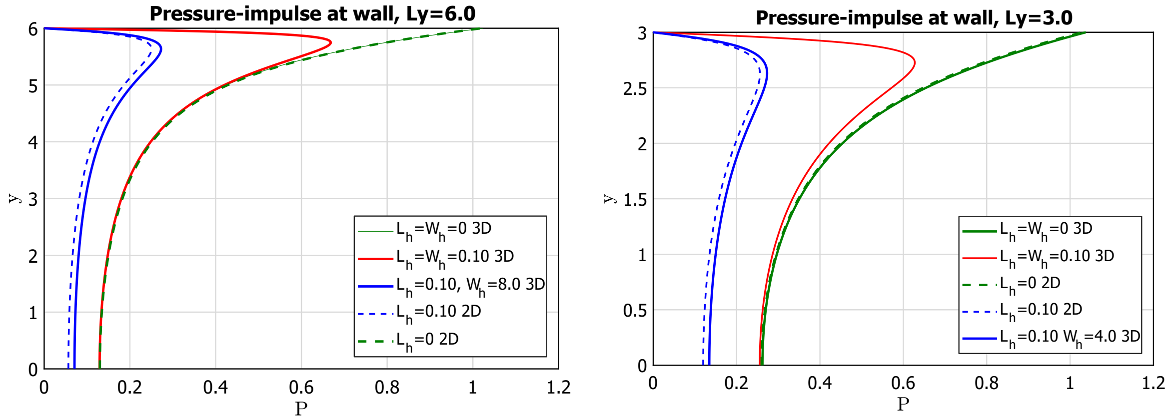

Figure 3.18: Comparison between 2D and 3D pressure-impulse results at the vertical wall for Cases 1 (left) and 2 (right).

Table 3.5: Maximum pressure-impulses, total impulse at wall and their reductions due to ventilations for Cases 1 and 2 from 3D simulations.

Case	P_{max}	P_{maxh}	R_{Ph}	I	R_I
1a	1.02	—	—	1.63	—
1b	1.02	0.67	34%	1.50	8%
2a	1.04	—	—	1.32	—
2b	1.03	0.75	27%	1.22	8%
2c	1.03	0.63	40%	1.12	15%

3.3. Parametric analysis

The relationship between the geometry of the structure, ventilation dimensions and maximum pressure-impulses are examined in this section. The objective is to understand the relative significance of the main parameters and attempt to define formulas for fast preliminary assessment of the influence of ventilations on vertical structures with overhangs subject to wave impacts.

3.3.1. Geometric parameters

In the 2D simulation without ventilations, the geometric parameters are defined as the vertical wall height L_y, domain length L_x and overhang length L_o. Since L_o is fixed as the unitary scaling parameter and L_x is the largest between $4L_o$ and $4L_y$, it is possible to derive expressions to obtain the maximum pressure-impulse $P_{max,0}$ and I_0 as a function of only L_y. Since no ventilations are used, $P_{max,0}$ is always located at the upper corner between the overhang length and the vertical wall and therefore is the peak pressure-impulse affecting both elements.

By varying the dimensionless L_y from 0.2 to 5.0, it is possible to determine the corresponding $P_{max,0}$ and I_0 from the analytical solution. The results indicate maximum dimensionless pressure-impulses inversely proportional to the vertical wall height. When $L_y < 1$, the overhang length under wave impact is larger than the vertical wall, leading to a steep increase of pressure-impulses as L_y decreases. For $L_y > 3$, the value of $P_{max,0}$ tends to 1.0. Two curves were fitted to evaluate the relationship between the parameters, as shown in Figure 3.19. The total impulse at wall obtained are in accordance to results published by Wood & Peregrine (1996).

The simple formula derived from curve fitting to obtain $P_{max,0}$ is expressed as

$$P_{max,0} = 2.788e^{-3.115L_y} + 1.028. \tag{3.2}$$

The total impulse formula is described by

$$I_0 = 0.8844L_y^{0.3456}. \tag{3.3}$$

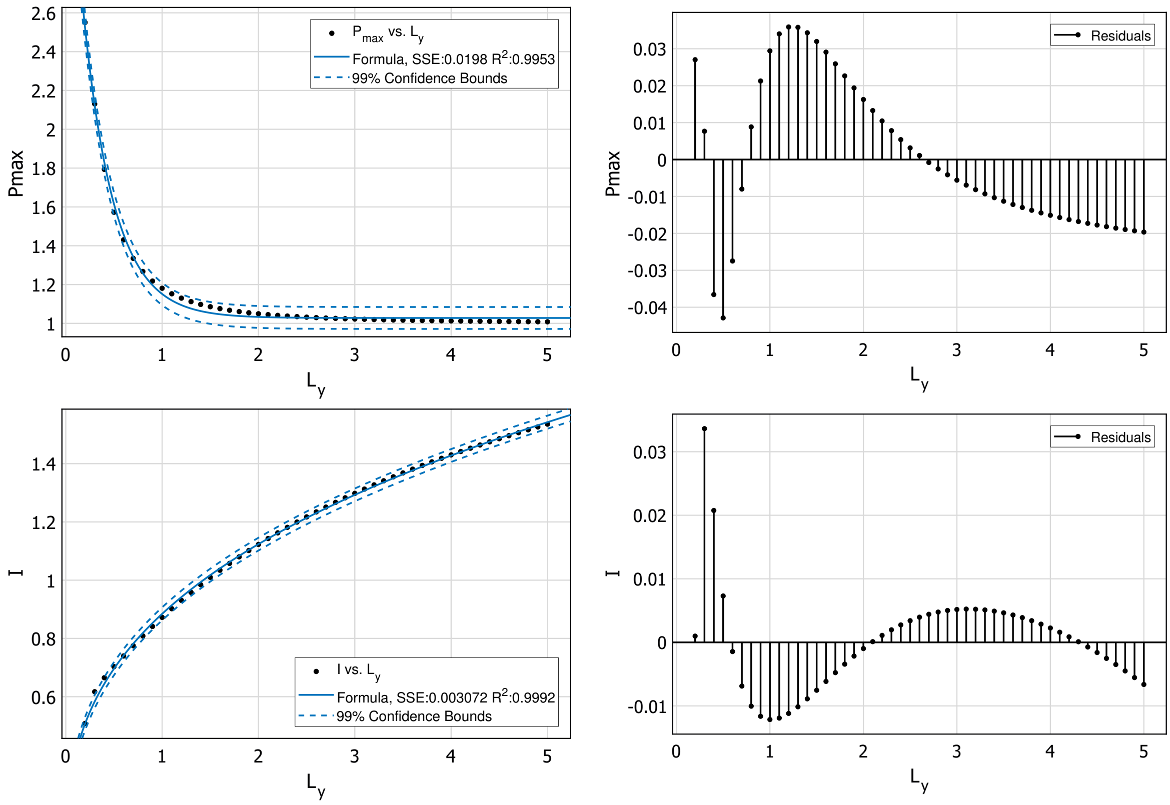

Figure 3.19: Fitted curves to determine $P_{max,0}$ and I_0 from L_y.

The maximum dimensionless pressure-impulses resultant from the analytical solution, numerical solution and formula for a range of vertical wall values are compared in Tables 3.6 and 3.7. Alternatively to the formulas presented, the exact analytical results for a wide range of L_y can be found at Table A.1 in Appendix A.

Table 3.6: Comparison of $P_{max,0}$ for a range of L_y.

	$P_{max,0}$			Relative error	
L_y	Analytical	Numerical	Formula	Numerical	Formula
0.50	1.5724	1.5695	1.6153	0.18%	2.73%
1.00	1.1810	1.1891	1.1517	0.69%	2.48%
2.00	1.0496	1.0577	1.0335	0.77%	1.53%
3.00	1.0225	1.0285	1.0282	0.59%	0.56%
6.00	1.0057	1.0197	1.0280	1.39%	2.22%

Table 3.7: Comparison of I_0 for a range of L_y.

	I_0			Relative error	
L_y	Analytical	Numerical	Formula	Numerical	Formula
0.50	0.7033	0.7014	0.6960	0.27%	1.04%
1.00	0.8722	0.8795	0.8844	0.84%	1.40%
2.00	1.1228	1.1336	1.1238	0.96%	0.09%
3.00	1.2979	1.3168	1.2928	1.46%	0.39%
6.00	1.6234	1.6308	1.6428	0.46%	1.19%

3.3.2. Ventilation parameters

The main ventilation parameters involved with the theoretical pressure-impulse model are the length of the venting hole L_h, the width of the venting hole W_h and the spacing S between ventilations. The area of ventilation is defined as $A_h = L_h W_h$ and the relative pressure-impulse release due to venting is

$$R_P = 1 - \frac{P_{max,vent}}{P_{max,0}}, \tag{3.4}$$

where $P_{max,vent}$ and $P_{max,0}$ are maximum pressure-impulses at wall including and excluding ventilations at any given cross-section, respectively. $P_{max,0}$ can be obtained from Equation 3.2. Similarly, the relative total impulse release due to venting is given by

$$R_I = 1 - \frac{I_{vent}}{I_0}, \tag{3.5}$$

where I_{vent} and I_0 are the total impulses on the wall including and excluding ventilations at any given cross-section, respectively. I_0 can be derived using Equation 3.3. Due to the ratios between the maximum pressure-impulses and total impulse in Equations 3.4 and 3.4, both R_I and R_P represent the release also if dimensional quantities are considered.

The current analysis examines the maximum pressure-impulse and total impulse at the vertical wall, in the middle section between two consecutive venting holes. In total, 41 3D simulations with $L_y = L_o = 1$ and $\Delta x = \Delta y = \Delta z = L_o/50$ were performed for the ranges of $1.0 < S < 6.0$, $0.1 < L_h < 0.5$ and $0.1 < W_h < 0.5$. Within these ranges, 13 simulations where $S/A_h > 100$ were avoided due to very small significance of the openings to release pressure-impulses in the section away from the holes. The release of total impulse due to venting among the considered parameters varied from 2% to 94%. For $L_y = 2.0$, 3.0 and 6.0, the same experiments were repeated. The complete results are available at Tables A.2, A.3, A.4 and A.5 in Appendix A.

To investigate the influence of each parameter individually, the case of $S = 3.0$ and $L_h = W_h = 0.3$ is utilized as reference for comparison. The height of vertical wall is fixed as $L_y = 1.0$. Table 3.8 demonstrates the qualitative sensitivity analysis conducted. Surely, the spacing between ventilations S has the highest influence on the release of maximum pressure-impulse and total impulse at wall among the three parameters. The width of the opening W_h influences slightly more than the length L_h, since it affects the direction where the largest pressure-impulses are concentrated, near the landward edge of the overhang.

Table 3.8: Sensitivity analysis of the ventilation parameters.

	S	L_h	W_h	ΔS	P_{max}	ΔP_{max}	I	ΔI
S_{min}	1.0	0.3	0.3	-67%	0.37	-63%	0.25	-64%
S_{base}	3.0	0.3	0.3	0%	1.00	0%	0.70	0%
S_{max}	6.0	0.3	0.3	100%	1.16	16%	0.85	21%
	S	L_h	W_h	ΔS	P_{max}	ΔP_{max}	I	ΔI
$L_{h,min}$	3.0	0.1	0.3	-67%	1.09	9%	0.78	11%
$L_{h,base}$	3.0	0.3	0.3	0%	1.00	0%	0.70	0%
$L_{h,max}$	3.0	0.5	0.3	67%	0.95	-5%	0.64	-9%
	S	L_h	W_h	ΔS	P_{max}	ΔP_{max}	I	ΔI
$W_{h,min}$	3.0	0.3	0.1	-67%	1.10	10%	0.78	11%
$W_{h,base}$	3.0	0.3	0.3	0%	1.00	0%	0.70	0%
$W_{h,max}$	3.0	0.3	0.5	67%	0.92	-8%	0.62	-11%

As represented in Appendix A, the relationship between different variables is tested to identify functions which predict R_P and R_I as functions of S, L_h and W_h. Good correlation was found against the relative venting area parameter A_h/SL_o. Figure 3.20 represents the data, fitted curves and 90% confidence bounds. The expression to estimate R_P becomes

$$R_P = \frac{213.80\frac{A_h}{SL_o} - 9.59}{\frac{A_h}{SL_o} + 29.20}. \tag{3.6}$$

R_I is determined by

$$R_I = \frac{163.30\frac{A_h}{SL_o} + 18.48}{\frac{A_h}{SL_o} + 18.00}. \tag{3.7}$$

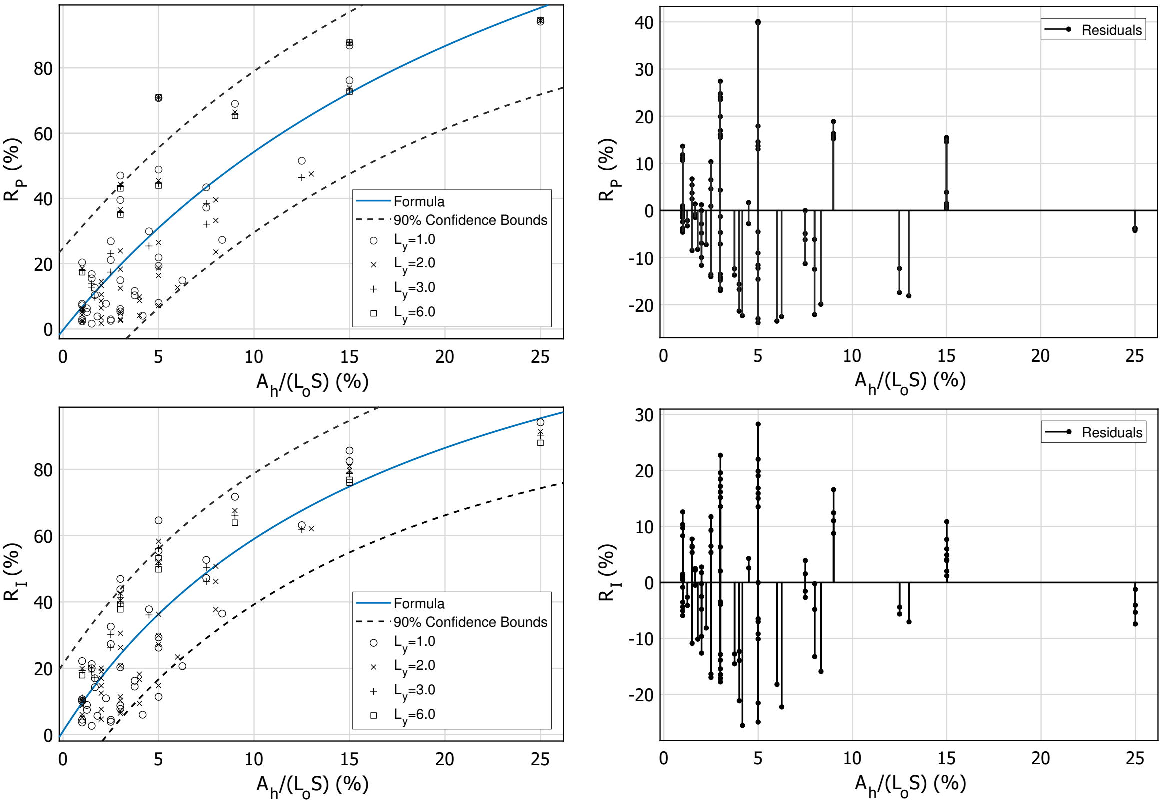

Figure 3.20: Fitted curves to determine R_P and R_I from ventilation parameters.

Equations 3.6 and 3.7 are only valid for the aforementioned ranges of S, L_h and W_h. It is implicitly assumed by using A_h that the influence from L_h and W_h are equal, but this uncertainty, for small venting holes areas, is considered to be less than the uncertainties associated with more complex formulas. After obtaining R_P and R_I from the formulas, the dimensionless maximum pressure-impulse and total impulse acting on the structure with ventilations can be estimated from Equations 3.4 and 3.5.

The statistical fit shows that the total impulse and its associated release from the simulations are more predictable than the maximum pressure-impulse. The same behaviour is found from the analytical simulations. From the relationship demonstrated between A_h/SL_o, R_P and R_I, interesting design implications can be inferred. For instance, selecting $A_h/SL_o > 10\%$ would release both P_{max} and I by more than 50%. Another point is that the dimensionless relative venting area A_h/SL_o is equivalent to the dimensional $\overline{A_h}/\overline{SL_o}$, since

$$\frac{A_h}{SL_o} = \frac{W_h L_h}{SL_o} = \frac{\overline{W_h}\,\overline{L_o}\,\overline{L_h}\,\overline{L_o}}{\overline{SL_o}\,\overline{L_o}\,\overline{L_o}} = \frac{\overline{A_h}}{\overline{SL_o}}. \tag{3.8}$$

4

Computational fluid dynamics

Wave impact simulations using computational fluid dynamics are carried out in this chapter. Two reference cases of vertical walls with overhangs are investigated regarding the influence of venting holes. They correspond to dimensional versions of Cases 1 and 2 from the pressure-impulse modelling assessment. The main equations which govern the flow and the wave generation method are briefly explained. The modelling procedure consists mainly of defining boundary conditions, establishing measurement locations and mesh generation. In 2D, the appropriate mesh refinement is determined though validation with experimental data. Finally, 3D simulations are performed to characterize the relative effect due to ventilations.

4.1. Overview

4.1.1. Governing equations

The open source computational fluid dynamics (CFD) software OpenFOAM® provides a collection of solvers and utilities appropriate to solve advanced fluid dynamics problems. The procedure to implement and execute an OpenFOAM® case is divided in three main stages: pre-processing, solving and post-processing. In the first stage, the creation of meshes define the domain geometry, boundary conditions and points where the solutions are saved. Subsequently, a variety of solvers are applied to determine the variables of interest from equations describing the flow. The output is then manipulated and visualized using post-processing tools in the last stage of the process.

Regarding the problem of impulsive wave impacts on structures, fluid velocities $\vec{u}$, pressures p and forces $\vec{F}$, along x, y and z directions over time t are the main variables of concern. The governing equations solved by OpenFOAM® to calculate these variables are (Holzmann (2016)):

1. Mass balance equation (Navier-Stokes)

$$\frac{\partial \rho}{\partial t} = -\nabla \cdot (\rho \vec{u})$$

2. Momentum balance equation (Navier-Stokes)

$$\frac{\partial}{\partial t}\rho \vec{u} = -\nabla \cdot (\rho \vec{u} \otimes \vec{u}) - \nabla \cdot \vec{\tau} - \nabla p + \rho g$$

3. Total energy equation

4. Kinetic energy equation

5. Internal energy equation

6. Enthalpy equation

OpenFOAM® offers numerical schemes to apply the shear rate tensor $\vec{\tau}$, as well as gradient ∇ and divergence $\nabla\cdot$ operators. Since the fluid is considered to be incompressible, the enthalpy and energy equations are not used in the wave impact simulations. The *PIMPLE* algorithm solves the Navier-Stokes equations by coupling pressure and momentum (Holzmann (2016)), using the volume of fluid method (Hirt & Nichols (1981)). This algorithm finds a steady-state solution using under-relaxation until convergence is reached, and then proceeds to the next time step.

From the solutions of the mass and momentum balance equations, a scalar field α is derived for each finite volume to track its fluid content, where $\alpha = 0$ for air and $\alpha = 1$ for water. Then it is possible to convey any fluid property Φ along space using the weighting

$$\Phi = \alpha\Phi_{water} + (1-\alpha)\Phi_{air}. \tag{4.1}$$

4.1.2. Wave generation

The *waves2Foam* toolbox (Jacobsen et al. (2011)) is required to implement numerical modelling of surface waves in OpenFOAM®. It has been validated and extensively employed in coastal and offshore engineering problems where detailed wave simulations are desired.

Reflected waves can interact with the generated waves, impairing the quality of the simulations and possibly causing discontinuities in the surface elevation boundary. To avoid this effect, an explicit relaxation zone technique is utilized to correct the velocity $\vec{u}$ and α fields after each time step. The relaxation function is expressed as

$$\Psi(\chi) = 1 - \frac{\exp\chi^{3.5} - 1}{\exp 1 - 1}, \tag{4.2}$$

where $\chi = 0$ at the inner edge and $\chi = 1$ at the outer edge of the relaxation zone. The correction is then applied inside the relaxation zone for Φ quantities ($\vec{u}$ or α) using

$$\Phi = \Psi\Phi_{computed} + (1-\Psi)\Phi_{target}, \tag{4.3}$$

where $\Phi_{computed}$ originates from solving the governing equations, and Φ_{target} designates solutions obtained by an arbitrary wave theory defined in *waves2Foam*. In this work, Φ_{target} is handled by the utility *OceanWave3D* (Engsig-Karup et al. (2009)), which generates waves in the first 10 meters along the longitudinal domain direction, and the absorption zone 40 to 50 meters away from the origin. The rectangular relaxation zone of inlet type is defined from 12 to 20 meters. These dimensions depend on the problem hydraulic conditions and are shown in Figure 4.1.

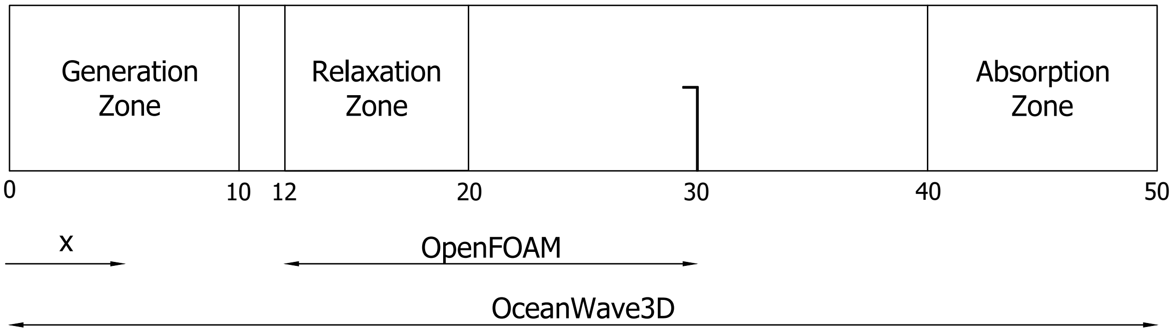

Figure 4.1: Wave generation, relaxation and absorption zones along the computational domain.

4.2. Model set-up

4.2.1. Initial and boundary conditions

A 30-meters long, 1-meter deep numerical wave flume is created in order to replicate experimental conditions from de Almeida et al. (2019). Similarly to the pressure-impulse modelling performed in Chapter 3, simulations are conducted to characterize wave impacts on a vertical wall with 60 *cm* in height and 10 *cm* or 20 *cm* in overhang length (Cases 1 and 2, respectively). Simulations in 2D are only used for initial testing purposes. To study the effects of ventilations, 3D models of width equal to 12.50 *cm* are utilized, which would allow for complete dissipation of ventilation effects for square holes of sides equal to 1 *cm*, according to the pressure-impulse model results.

Boundary conditions of wall type with no-slip velocity are assigned to vertical wall, overhang and bottom of the flume. Inlet boundaries are applied to the vertical faces near the wave generation zone. The top boundary is attached to atmospheric conditions and the lateral flume faces are of empty type in 2D and of symmetry type in 3D models. A summary of the boundary conditions setup is presented at Table 4.1. Fluid track α, velocity u and non-hydrostatic pressure p fields are assigned values as described.

Table 4.1: Boundary conditions employed in the numerical wave tank.

Boundary Condition	Type	α	u	p
Inlet	patch	waveAlpha	waveVelocity	zeroGradient
Bottom	wall	zeroGradient	slip	zeroGradient
Structure	wall	zeroGradient	slip	zeroGradient
Atmosphere	patch	inletOutlet	pressureInletOutletVelocity	totalPressure
Ventilation	patch	inletOutlet	pressureInletOutletVelocity	totalPressure
FrontBack	empty/symmetry	empty/symmetry	empty/symmetry	empty/symmetry

Regular waves of period $T = 1.3$ *s* and incoming wave height $H_i = 6$ *cm* characterizes all simulations carried out. The constant water level of 60 *cm* is level with the overhang elevation. At the inlet region, waves are generated in *OceanWave3D* for 40 *s*, allowing the waves to completely develop before the start of the CFD calculations. Figure 4.2 depicts the wave propagation along time at $x = 25$ *m*.

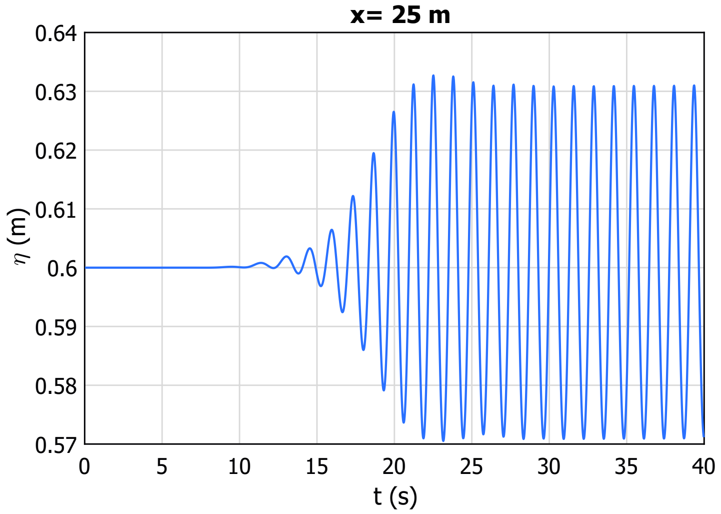

Figure 4.2: Initial wave development at $x = 25$ *m*.

The waves are generated as a stream function with wave length $L_w = 2.42$ *m* and obtained by solving a three-dimensional nonlinear potential flow problem using a multigrid finite difference scheme in *OceanWave3D* (Engsig-Karup et al. (2009)).

4.2.2. Probes and wave gauges

Particular points of interest are tracked for processing the simulation results. Probes record the non-hydrostatic fluid pressures and flow velocities on the wall structure and overhang. The total forces on the wall face is derived by integrating the pressures from each probe over the corresponding areas. Wave gauges measure the surface elevations over time. In total, 12 probes and 10 wave gauges are used at the locations depicted in Figures 4.3 and 4.4.

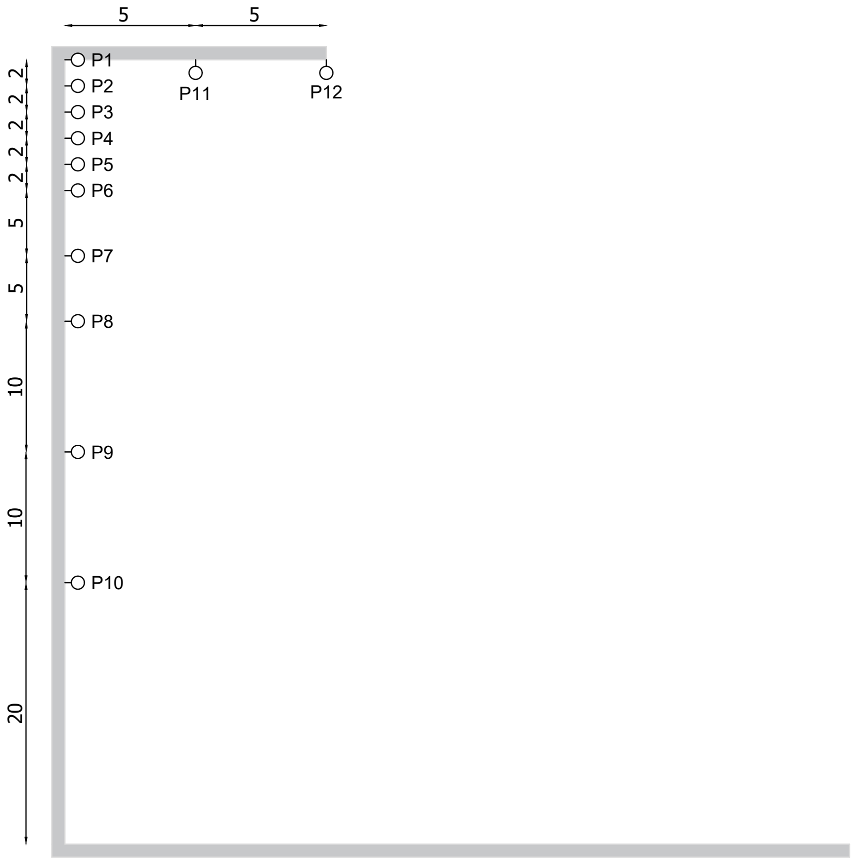

Figure 4.3: Side view of probe locations (all units in *cm*).

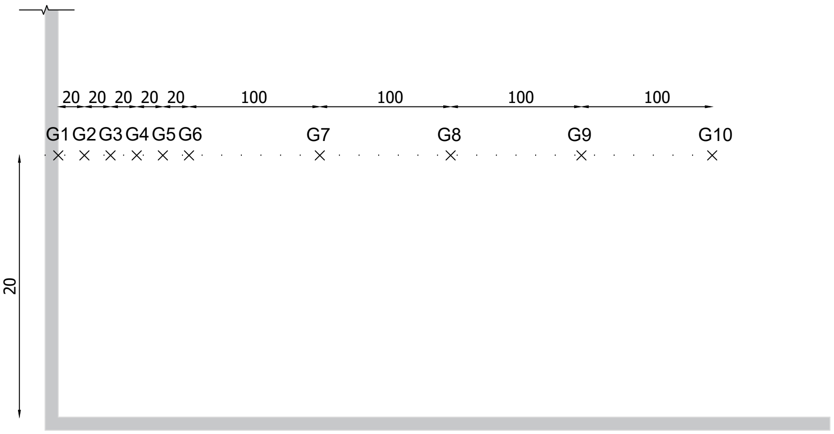

Figure 4.4: Side view of wave gauge locations (all units in *cm*).

In order to measure impulsive forces that occur in a very short time, it is crucial that the solver time step is small enough. For all simulations, the computation time interval dt varies from 1×10^{-5} *s* to 1×10^{-3} *s*, according to the relationship given by

$$C_o = \frac{\vec{u}dt}{\Delta x} \leq 1, \tag{4.4}$$

where the Courant number C_o represents a stability parameter set as 0.45, based on the wave impact simulations carried out in Castellino et al. (2018).

The function *waveGaugesNProbes* is executed to assign the wave gauges locations and sampling rate. The output control is set to the adjusted time step from Equation 4.4, allowing for an adequate measurement frequency.

4.2.3. Mesh creation and testing

Using the utility *blockMesh*, several two-dimensional meshes are created from a composition of blocks with controlled number of segments along each coordinate direction. The quantity of cells resultant from the divisions for Meshes 1, 2, 3, 4 and 5 are shown in Table 4.2. The cells are approximately square in the impact region for better stability. Each mesh refinement is classified by the correspondent number of points per wave length (p.p.w.l.).

Table 4.2: Properties of test Meshes 1, 2, 3, 4 and 5.

Mesh number	Minimum $\Delta x \approx \Delta y$ (mm)	Points per wave length	Total number of cells
1	16.0	150	68420
2	11.0	225	154788
3	8.0	300	273680
4	5.0	450	250996
5	0.4	3600	179068

Even though Mesh 4 is more refined than Mesh 3 in the impact region, the total number of cells are less due to the application of an expansion coefficient to improve efficiency by gradually decreasing the cell size 5 times along the x direction. Mesh 5 further optimizes Mesh 4 by using the expansion approach also in the z direction and receives a rectangular refinement region with two levels at the corner between the wall and overhang through the utility *snappyHexMesh*. The visual comparison between meshes is displayed in Figure 4.5.

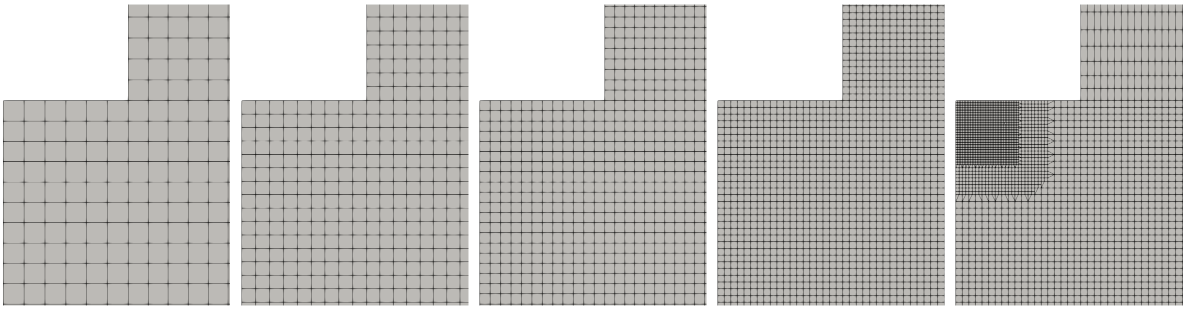
(a) Mesh 1 (b) Mesh 2 (c) Mesh 3 (d) Mesh 4 (e) Mesh 5

Figure 4.5: Geometries of 2D test meshes (zoomed in at impact region).

Considering Case 1a, with 10 cm overhang and no ventilation, test runs are executed for each mesh from 40 *s* to 50 *s* after the beginning of the wave generation. All mesh schemes are then validated against experimental measurements from de Almeida et al. (2019), where no ventilations are present. Figure 4.6 depicts how the convergence of impulsive force peaks is sensitive to mesh refinements. The validation over the entire force time series for Cases 1a and 2a using 2D meshes is depicted in Figure 4.7.

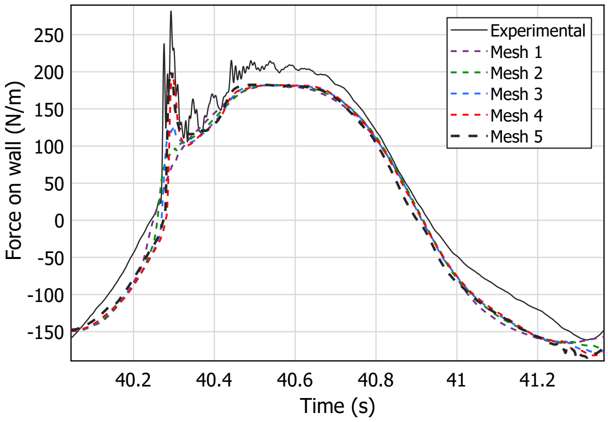

Figure 4.6: Comparison of forces between test runs and experimental data for the first simulated impact at Case 1a.

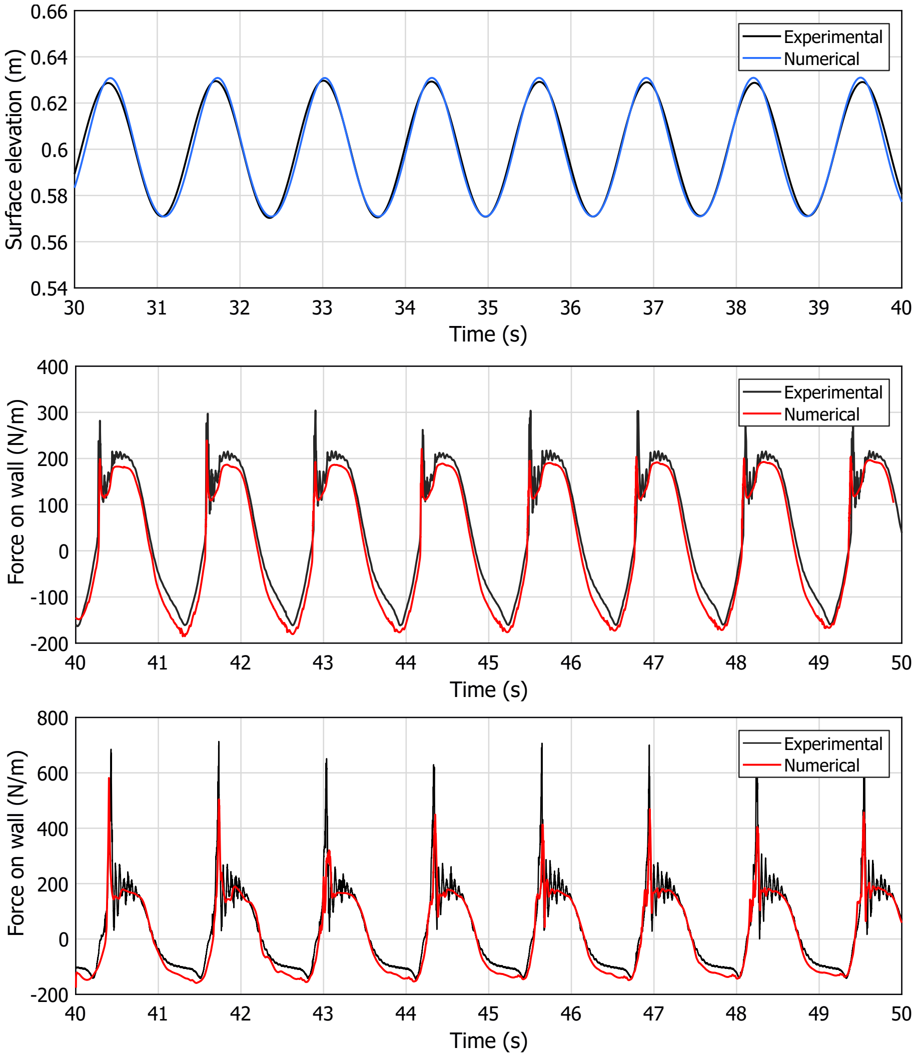

Figure 4.7: Validation of numerical surface elevation from incoming waves (top) and total forces on the wall for Cases 1a (middle) and 2a (bottom).

The results show good agreement between numerical simulations and the experimental data. However, it is essential that the computational grid is refined enough to converge the peak impulsive forces. Only quasi-static loadings are observed using the most coarse grid, Mesh 1. Due to the need for accuracy to assess ventilations, Mesh 5 is then selected as the reference refinement for all simulations. A comparison between numerical and experimental incoming wave surface elevations is also presented. Generally, the numerical results underestimate peak measured forces, but the impact durations and quasi-static loadings are well predicted.

4.3. Study cases results

After validating two-dimensional wave impact models, the effect of ventilations is examined through three-dimensional models in this section. The meshes are now also refined along the width, including additional elements to account for openings (see Figure 4.8). Since the side boundary conditions are symmetric, only half of the gap width is simulated. At least 32 cells compose the surface area relative to the opening to ensure that the flow is correctly resolved.

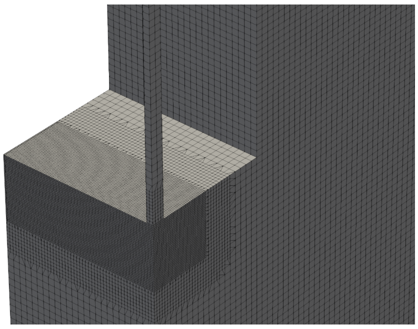

Figure 4.8: Three-dimensional mesh for the case of 10 *cm* overhang, 1 cm^2 ventilation.

The simulations are performed on an Intel Xeon® 3.50 GHz cluster equipped with 64 GB of RAM and using 20 processors in parallel. Figure 4.9 shows the surface elevation before, during and after wave impact at a vertical wall with 1 *cm* ventilation. Snapshots for other cases are available in Appendix C.

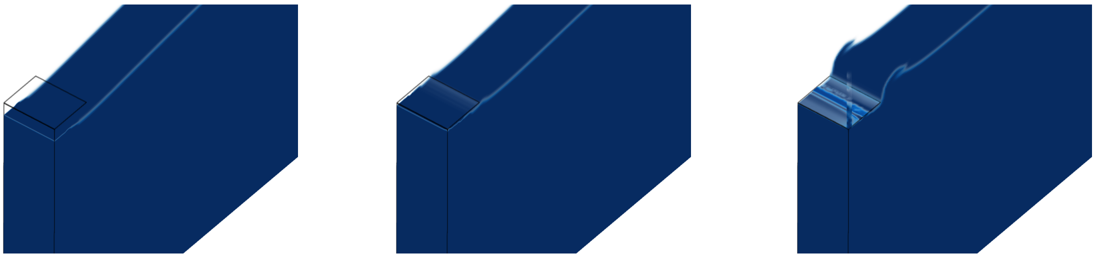

(a) $t = 40.40\ s$ (b) $t = 40.50\ s$ (c) $t = 40.60\ s$

Figure 4.9: Surface elevation before (left), during (middle) and after (right) the first impact, for the case of vertical structure with overhang 10 *cm* long and 1 *cm* of venting width.

4.3.1. Pressure release

The most visible pressure differences due to venting holes can be seen at Probe 1 located at the corner between the wall and horizontal deck. Figure 4.10 illustrates how a venting hole with length $\overline{L_h} = 1\ cm$ and width $\overline{W_h} = 1\ cm$ affects pressures locally during the first simulated impact. At the section through venting, the peak pressure p_{max} decreases approximately 30%. Consequently, there is a substantial reduction also of pressure-impulse P at this point, which can only be quantified after separation of impulsive and quasi-static loadings. The same behaviour is observed for the cases of 20 *cm* overhang with $\overline{L_h} = \overline{W_h} = 1\ cm$ and $\overline{L_h} = \overline{W_h} = 2\ cm$ (Figure 4.11), showing peak pressure releases R_p of 18% and 30%, respectively.

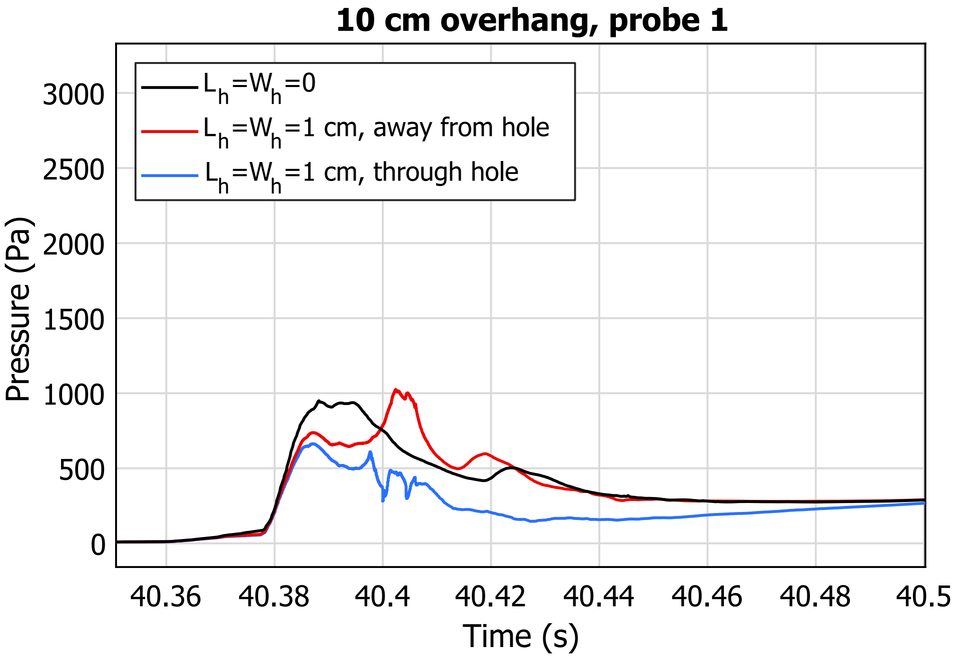

Figure 4.10: Comparison of pressures measured at probe 1 for Case 1.

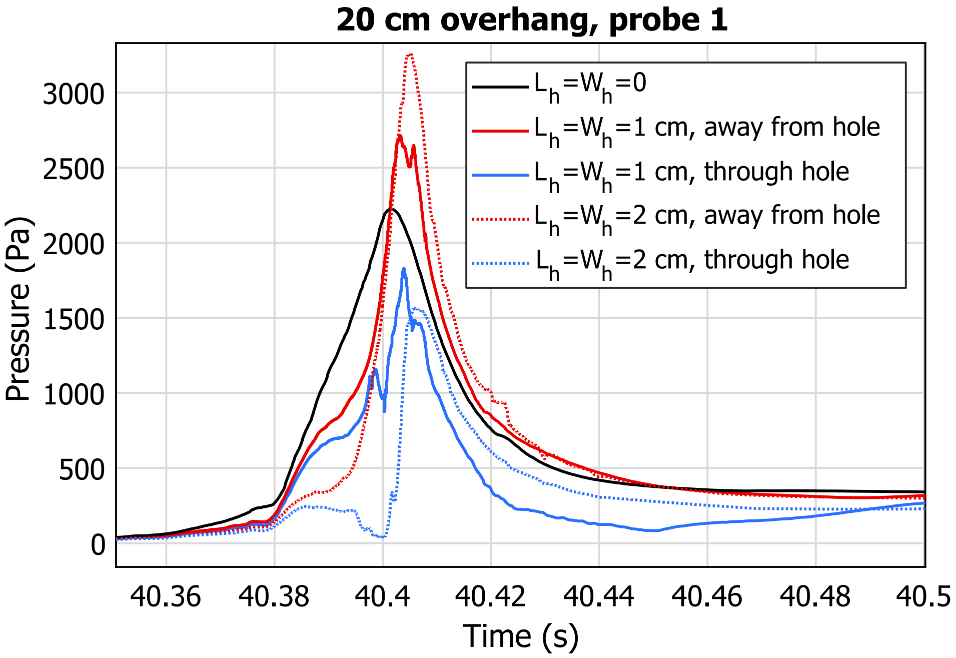

Figure 4.11: Comparison of pressures measured at probe 1 for Case 2.

In analogy to the releases of pressure-impulse R_P and total impulse R_I, the release of peak pressure R_p is defined here as

$$R_p = 1 - \frac{p_{max,vent}}{p_{max,0}}. \tag{4.5}$$

Table 4.3 lists the peak pressure p_{max}, release of peak pressure R_p and impact instants t_i for each case. Negative R_p values mean that there is an increase peak pressure with venting $p_{max,vent}$, compared to the reference without ventilation $p_{max,0}$.

Table 4.3: Peak pressures p_{max} and impact instants t_i at Probe 1 for each simulated case.

Case	$\overline{L_o}$ (cm)	$\overline{L_h} = \overline{W_h}$ (cm)	p_{max} (Pa)	R_p	t_i (s)
1a	10.00	0.00	950	—	40.3882
1b, away from hole	10.00	1.00	1023	-8%	40.4018
1b, through hole	10.00	1.00	663	30%	40.3871
2a	20.00	0.00	2224	—	40.4016
2b, away from hole	20.00	1.00	2712	-22%	40.4032
2b, through hole	20.00	1.00	1829	18%	40.4039
2c, away from hole	20.00	2.00	3258	-46%	40.4051
2c, through hole	20.00	2.00	1567	30%	40.4058

The pressure-impulse decrease through venting is aligned with the mathematical model treated in Chapter 3. However, the increase of peak pressures at sections away from holes on the cases with venting, was not expected and cannot be directly inferred from the pressure-impulse model. But there is a delay effect at the section away from the hole, which slightly increases the time of impact t_i, and generally causes the impact shape to become narrower in comparison to the cases without venting. Consequently, as long as the spacing between ventilations is long enough to disperse the venting pressure release, the integral of the pressure over the impact duration away from hole is approximately equivalent to the situation without venting, in agreement with the mathematical model.

A possible explanation for the peak increase and shorter duration of impacts lies on the increased water flow velocities in the region around the hole. At the beginning of the impact, some water mass first escapes through the venting and attenuates the impulse, even at the section away from the hole. Since the gap is small, only a limited amount of water is able to flow out in the very short duration of impact. The remaining mass then collides against the overhang with an increased velocity associated with higher forces and pressures. But this increase in peak forces is compensated by a shorter impact force area. Theoretically, a venting gap wide and long enough to allow outflow of all mass involved with the wave impact would attenuate all impulsive forces and the impact on the wall would be equivalent to the case without overhang at all.

In Chapter 5, a deeper analysis is done regarding pressure-impulses for the simulation results, by separation of impulsive and pulsating loads. Also, the effects of ventilations on the velocity field are discussed.

4.3.2. Pressure fields

Figures 4.12 to 4.15 compare the instantaneous non-hydrostatic pressure field for all cases during the first simulated wave impact, at $t = 40.40$ *s*. The results imply that ventilations release pressure locally in a similar fashion to the pressure-impulse model discussed in Chapter 3.

Clearly, the efficiency of the venting holes is higher for the longer overhang, where the largest pressures occur. The side view of pressure contours depicts the concentration of loadings at the corner between the vertical wall and the overhang. In the presence of ventilations, this peak of pressures shifts to the region below the horizontal surface, as depicted in Figures 4.12 and 4.13 for Cases 1 and 2, respectively.

By examining the front view of the instantaneous pressure contours at the moment of impact (Figures 4.14 and 4.15), it may be inferred that a hole 1 *cm* wide almost has no effect on the decrease of loadings for a structure with overhang 10 *cm* long, and the 2 *cm* gap would release a significant amount of pressures by itself. But these interpretations are misled due to the change of geometry between

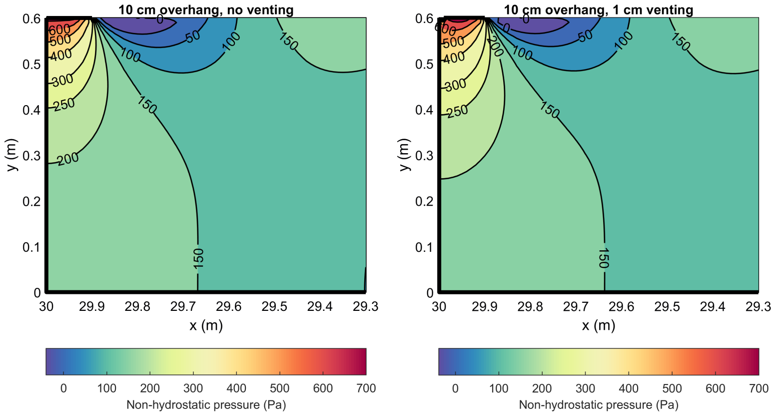

Figure 4.12: Side view of pressure distribution in Cases 1a (left) and 1b (right).

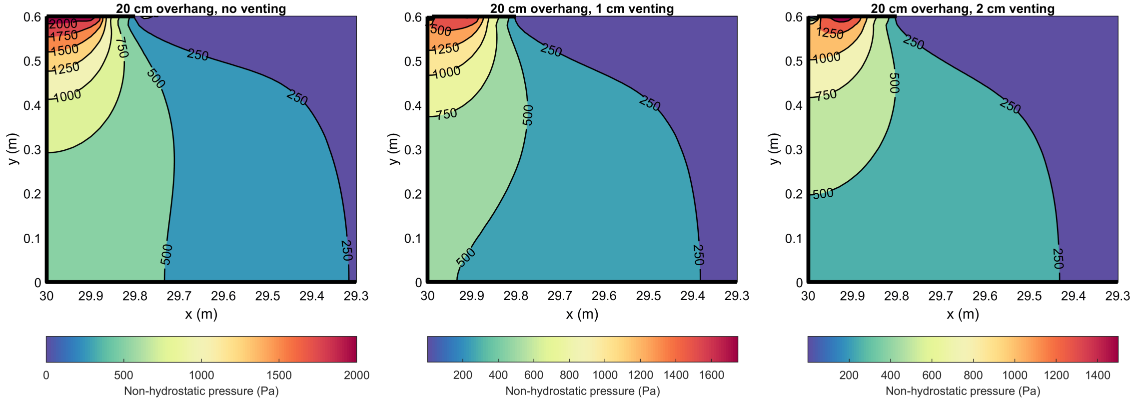

Figure 4.13: Side view of pressure distribution in Cases 2a (left), 2b (middle) and 2c (right).

cases, which modifies the flow and consequently advances or delays the exact moment of the impulsive impacts. Even though the changes are very short, this phenomenon hinders the ability to quantify the real influence of ventilations due to the intense and fast nature of impulsive forces.

Therefore, the next investigations in Chapter 5 are based on the cumulative distribution of pressures along time from pressure-impulse and total impulse quantities.

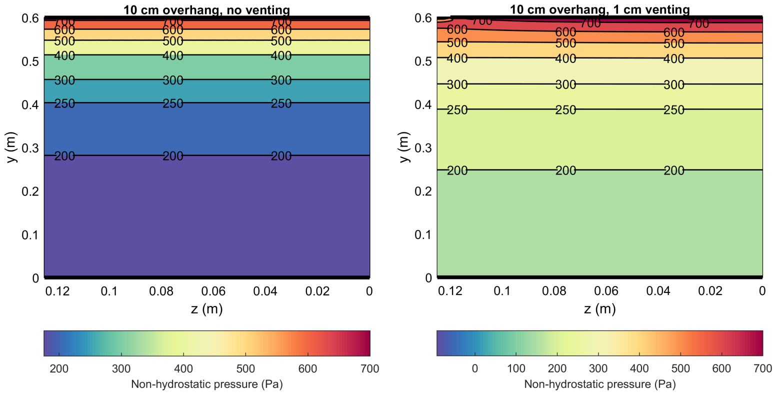

Figure 4.14: Front view of pressure distribution in Cases 1a (left) and 1b (right).

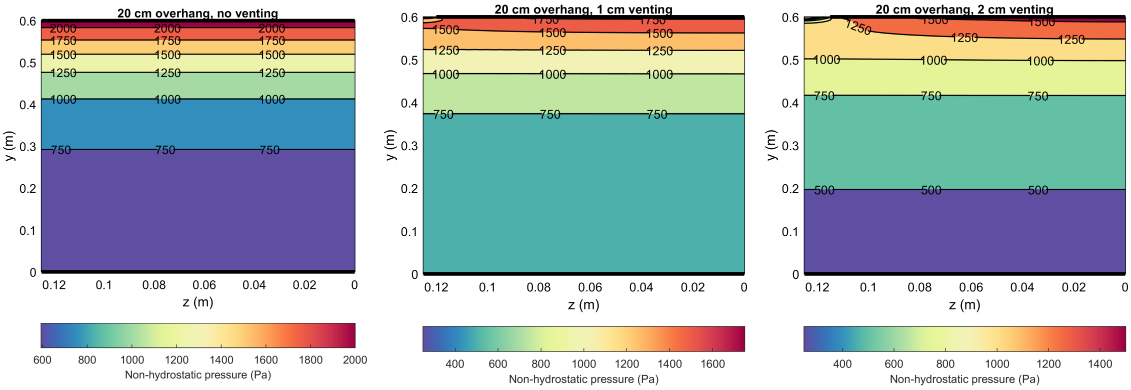

Figure 4.15: Front view of pressure distribution in Cases 2a (left), 2b (middle) and 2c (right).

5

Analysis and validation

In this chapter, the pressure-impulse mathematical model from Chapter 3 is compared with computational fluid dynamics simulations performed in Chapter 4. To this end, some further translations of results are necessary. Splitting of the simulated impulsive and quasi-static forces is achieved using theoretical pressure distributions and low-pass filters. Both separation methods are evaluated against available experimental data. Vertical impact velocities are determined from standing wave theories, probes and wave gauges measurements employed in the simulations.

These approaches are combined and compared to process simulation results, as well as to convert dimensionless pressure-impulses from theory to dimensional forms. Then pressure-impulses along the wall height from the mathematical and CFD models are validated, allowing the identification of similarities and discrepancies. The main parameters of comparison are the total impulse and maximum pressure-impulse along the wall in conjunction with their releases due to ventilations.

5.1. Impact impulses

Instead of considering only local pressures as in Section 4.3.1, the total force is now used to represent an integrated effect over the entire structure and to compare splitting methods with simulated and experimental results. The total force F on the wall, per meter wide, is calculated from the probe pressure p measurements as

$$F = \int_0^{\overline{L_y}} p dy \approx p_n A_n, \tag{5.1}$$

where p_n and A_n are the pressure and area of influence, per meter wide, corresponding to each n Probe.

Separation between impulsive and quasi-static loadings is the first step required to derive wave impact impulses from a time series of recorded forces. Two main approaches are tested for this splitting, the first consists of calculating theoretical pulsating loadings to find intersection points and the second involves applying signal processing techniques to filter out impulsive loads.

Using Equation 2.1, the quasi-static force distribution from linear wave theory is determined for standing wave conditions with the hydraulic properties mentioned in Sub-section 4.2.1. An algorithm reads both simulated and calculated loads, finds the force peaks in the time series and intersection points between loads. The crossing points define the initial and final impact times, as well as the total impact duration Δt. Integration of the total forces at wall from the initial to the final impact instants provides the total impulse at wall for each wave impact.

Alternatively, the same process is repeated using the Sainflou (Sainflou (1928)) quasi-static force distribution, as described by Equation 2.2. Figure 5.1 depicts this separation method using the linear wave and Sainflou theories. The method is applied to simulated results for the wall with 10 *cm* overhang, without venting holes. It can be seen from the plots that the theoretical distributions are larger than simulated loadings, specially when the Sainflou method is employed. This matches experimental results from Rundgren (1958), which concluded that Sainflou's theory overestimates the non-breaking wave force for steep waves (Kisacik (2012)).

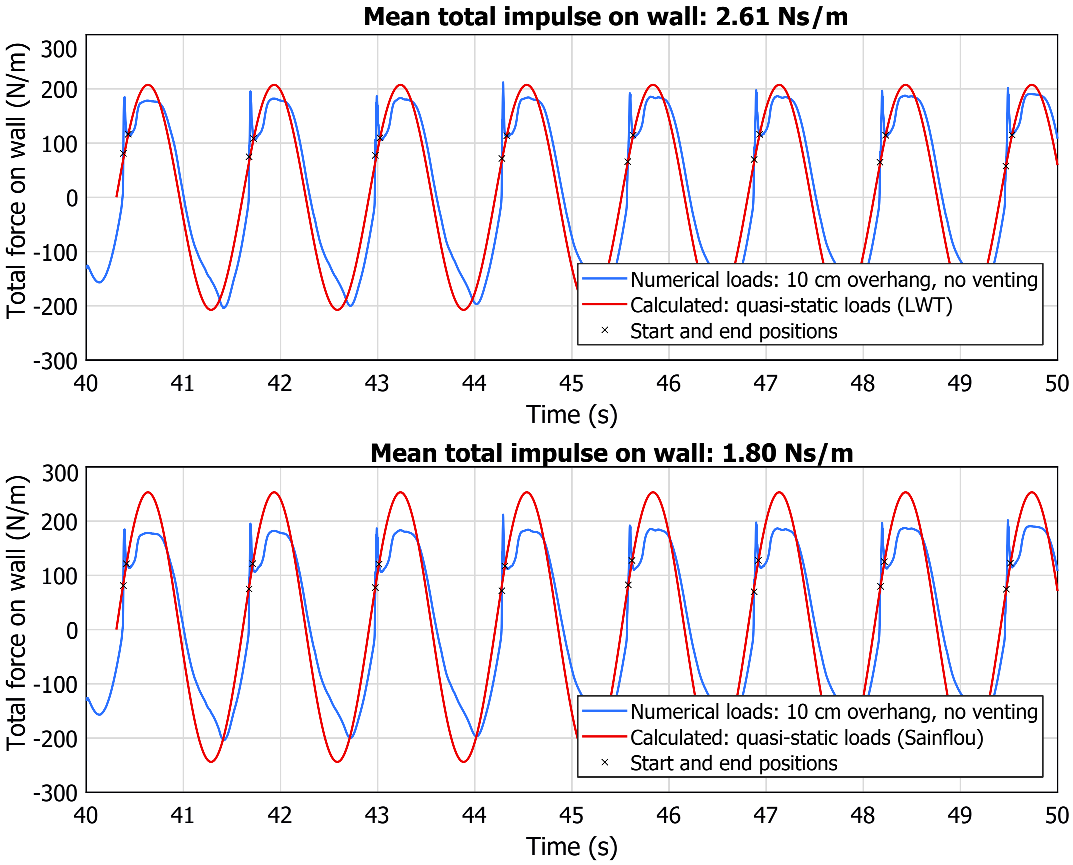
Mean total impulse on wall: 2.61 Ns/m

Mean total impulse on wall: 1.80 Ns/m

Figure 5.1: Derivation of impact impulses using linear wave theory and Sainflou quasi-static loadings.

In the second method of impact impulse derivation, impulsive and quasi-static loadings are separated using a third order, low-pass Butterworth filter. Before this filter can be applied, linear interpolation of the force signal achieves a steady frequency of 10000 *Hz*, as opposed to the variable frequency present in the raw data. Once the filter is employed, the impact duration and impulses are found as described in the previous method. Several cut-off frequencies were tested to find the filter that minimizes the difference between simulated and experimental impulses. Filters with calibrated cut-off frequencies of 2.0 and 1.6 *Hz* were found to produce the best results for the cases of vertical structures with 10 and 20 *cm* overhangs, respectively.

The filters successfully eliminate the impulsive peaks from the data, while preserving the quasi-static components of the original signal. Figure 5.2 shows the splitting and impulse derivation results applying the filtering method using 1.6 and 2.0 *Hz* cut-off frequencies for the simulated force signal corresponding to the seawall with 10 *cm* overhang, without venting.

Table 5.1 compares all impact impulses and durations from simulated and experimental data, obtained by both methods and their variations. The results correspond to impacts on 10 *cm* and 20 *cm* long overhangs, without venting (Cases 1a and 2a).

Due to overall better agreement of impact impulses between experimental and simulated data produced, the filtering method using 2.0 *Hz* cut-off frequency is selected as the standard for 10 *cm* over-

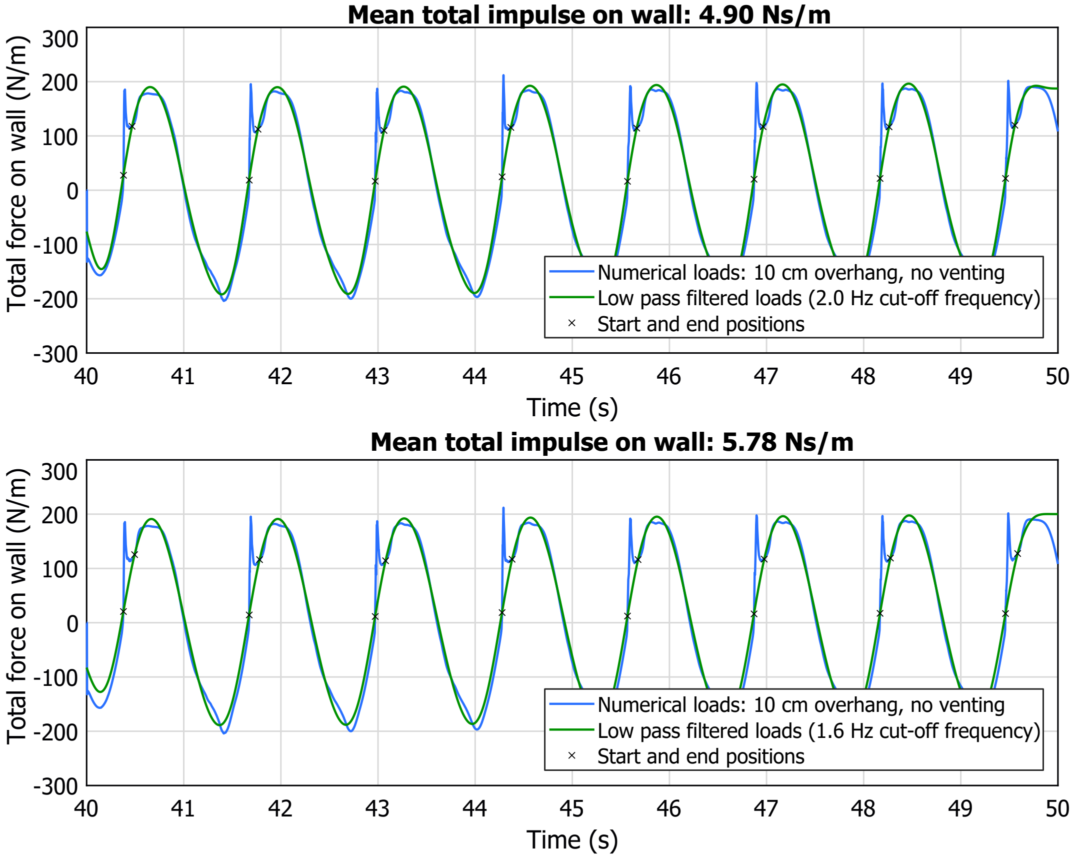

Figure 5.2: Derivation of impact impulses using Butterworth filters with 2.0 and 1.6 *Hz* cut-off frequencies.

hang length and 1.6 *Hz* cut-off frequency for for 20 *cm* overhang length in further analyses. Even though impact durations are much shorter in experimental than in simulated data using the filtering technique, the higher force peaks compensate for these differences. In Appendix D, simulated and experimental data filtering results can be found.

Table 5.1: Comparison of impact impulses and durations obtained by using theoretical pressure distributions and filtering. The values represent averages between 8 impacts.

	Total dimensional impulse $\bar{I}$ (Ns/m)				Impact duration Δt (ms)			
	Pressure method		Filtering method		Pressure method		Filtering method	
Case	LWT	Sainflou	2.0 Hz	1.6 Hz	LWT	Sainflou	2.0 Hz	1.6 Hz
1a simulated	2.61	1.80	4.90	5.78	53.75	37.50	92.10	109.98
1a experimental	5.33	4.43	4.98	5.47	54.50	46.25	49.13	57.38
2a simulated	12.97	10.48	10.72	12.60	112.75	96.38	101.00	113.34
2a experimental	18.35	16.40	13.60	14.94	99.13	87.88	70.00	75.00

5.2. Impact durations and peak forces

After choosing the default splitting method, the initial impact instant t_1, final impact instant t_2 and total impact duration $\Delta t = t_2 - t_1$ can be determined for all cases. Impact durations can be used to estimate peak forces or pressures from pressure-impulse quantities. Since these durations vary for different heights, they are obtained from the total force signal to represent the total impact on the wall.

Figure 5.3 illustrates how the filtering method provides distinct impact durations for Case 1, in which

$\overline{L_o} = 10$ *cm*, considering the first simulated impact. The force peak F_p represents the difference between peak forces and the filtered quasi-static forces at the instant of impact. It can be noticed that peak impulsive forces are higher in the experimental case than in simulated cases, but the total impulses are similar due to shorter impact duration in physical modelling tests. The impact durations are 49 *ms* for the experimental situation without venting, as opposed to 87 and 89 *ms* durations for simulated cases without venting and including 1 *cm* venting, respectively.

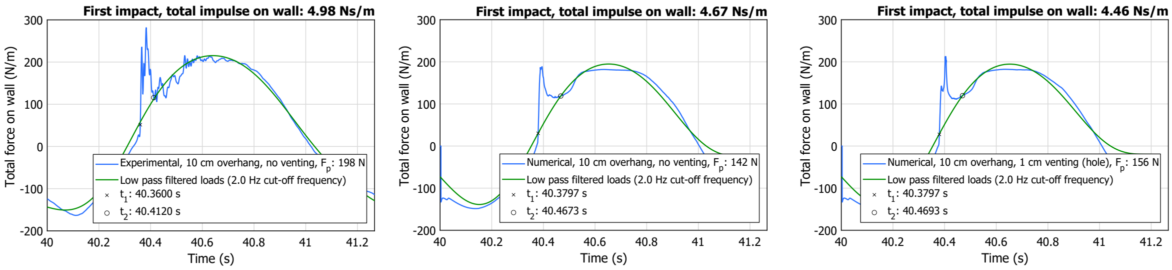

Figure 5.3: Total impulses, initial and final impact instants and force peaks for experimental Case 1a (left) and simulated Case 1a (middle) and 1b, section through hole (right).

Once the impact durations are known, peak forces are usually estimated assuming a triangular impact shape (Renzi et al. (2018)), where the total impulse $\bar{I}$ is defined by the area of a triangle with base equal to the impact duration Δt and height equal to the peak force F_p. Therefore, the estimated peak force $\tilde{F_p}$ is expressed as (Hofland et al. (2019)))

$$\tilde{F_p} = \frac{2\bar{I}}{\Delta t}. \tag{5.2}$$

Table 5.2 lists the first and final impact instants t_1 and t_2, impact duration Δt, total impulse $\bar{I}$ and peak force F_p obtained from the filtering method proposed in Section 5.1. These results correspond to the first wave impact after $t = 40$ *s*, when the simulations start. Duration of impacts from physical modelling data tends to be significantly shorter than from simulated cases. Through Equation 5.2, the peak force $\tilde{F_p}$ is estimated and compared to the actual peak force F_p. Only for experimental Case 1a, the error between predicted and estimated peak forces is small (3%). For all other cases, Equation 5.2 consistently underestimates maximum forces, which would be unacceptable in engineering designs. The cause of this lack of prediction skill is the shape difference between the peak signal and an idealized triangle. A more conservative approach would be to approximate the impulse area as $\bar{I} \approx \tilde{F_p}\Delta t_{1/2}$, where $\Delta t_{1/2}$ represents the time interval between forces at half the peak force height. But a more complete study, including more cases and impacts is required to test this hypothesis. These results are demonstrated graphically in Appendix D.

Table 5.2: Impact duration and peak force analysis results for the first impact in all experimental and simulated cases.

Case	$\overline{L_o}$ (cm)	$\overline{L_h}$ (cm)	t_1 (s)	t_2 (s)	Δt (ms)	$\bar{I}$ (N·s/m)	F_p (N/m)	$\tilde{F_p}$ (N/m)	Error
1a, experimental	10.00	0.00	40.360	40.412	52.00	4.98	198	192	3%
1a, simulated	10.00	0.00	40.380	40.467	87.60	4.67	142	107	25%
1b, away from hole	10.00	1.00	40.380	40.469	89.20	4.58	162	103	37%
1b, through hole	10.00	1.00	40.380	40.469	89.60	4.46	156	99	36%
2a, experimental	20.00	0.00	40.379	40.451	72.00	14.86	515	413	20%
2a, simulated	20.00	0.00	40.381	40.465	83.80	13.33	532	318	40%
2b, away from hole	20.00	1.00	40.382	40.467	84.20	13.39	641	318	50%
2b, through hole	20.00	1.00	40.382	40.467	84.20	13.23	631	314	50%
2c, away from hole	20.00	2.00	40.388	40.469	80.50	13.27	694	331	52%
2c, through hole	20.00	2.00	40.389	40.470	80.20	12.94	678	323	52%

5.3. Vertical impact velocities

A measure of vertical velocity at the wave impact U is required to convert impulses from dimensional to the dimensionless pressure-impulse form resultant from the pressure-impulse model discussed in Chapter 3. For a standing wave of water level equal to the wall height $h_s = 0.60$ *m*, wave height $H_i = 0.06$ *m* and wave period $T = 1.30$ *s*, the vertical velocity can be estimated using Equations 2.22, 2.23 and 2.24 from Subsection 2.4.

Using the surface elevations and vertical velocity distributions from the wave theories, an approach similar to Wood (1997) is proposed. Since the pressure-impulse model assumes that impact occurs at still water level, it is necessary to determine the standing wave velocity when the surface elevation is approximately flat and equal to the wall height. At this instant, the velocity profile peak is taken to be at wall, since it is a symmetry point. The average theoretical velocity is considered to be the mean from the start until the end of the deck length, as seen in Figure 5.4 below. The mean velocity difference between the shorter and longer decks is very small.

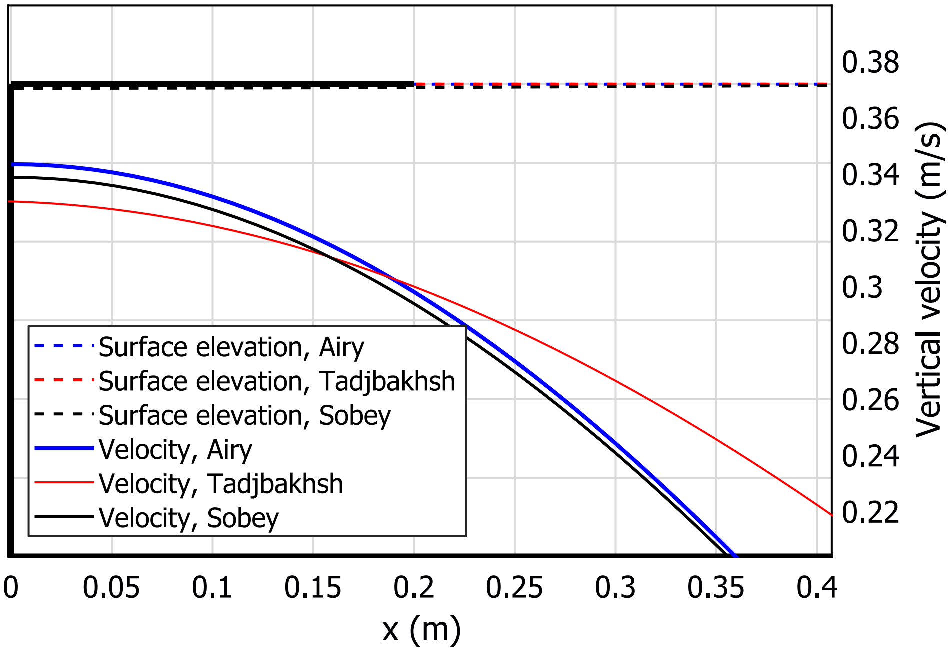

Figure 5.4: Comparison between theoretical vertical wave velocities for flat surface elevation at overhang 0.6 *m* high and 0.2 *m* long.

Table 5.3 shows the predicted velocity results from Airy (Schiereck (1996)), Tadjbakhsh (Tadjbakhsh & Keller (1960)) and Sobey (Sobey (2009)) for overhangs of 10 and 20 *cm*. A major uncertainty involved between theories and the simulated velocities is the wave reflection at wall, which is considered theoretically to be perfect, with 100% reflection coefficient. This effectively doubles the incoming wave height as the wave becomes standing, but that is not exactly the case in the simulated results.

Table 5.3: Theoretical wave impact velocities for each overhang length.

$\overline{L_o}$ (cm)	U_{Airy} (m/s)	$U_{Tadjbakhsh}$ (m/s)	U_{Sobey} (m/s)
10	0.33	0.33	0.33
20	0.33	0.32	0.32

Every 100 *ms*, CFD simulation results are available for every domain cell, allowing the creation of velocity field plots as seen in Figure 5.5. These plots show how velocities change direction to become vertical as the water flow approaches the wall, at $t = 40.40$ s. The velocity magnitude gradually increases near the surface, but remains somewhat constant along the x direction. In Appendix E, plots for all cases are available.

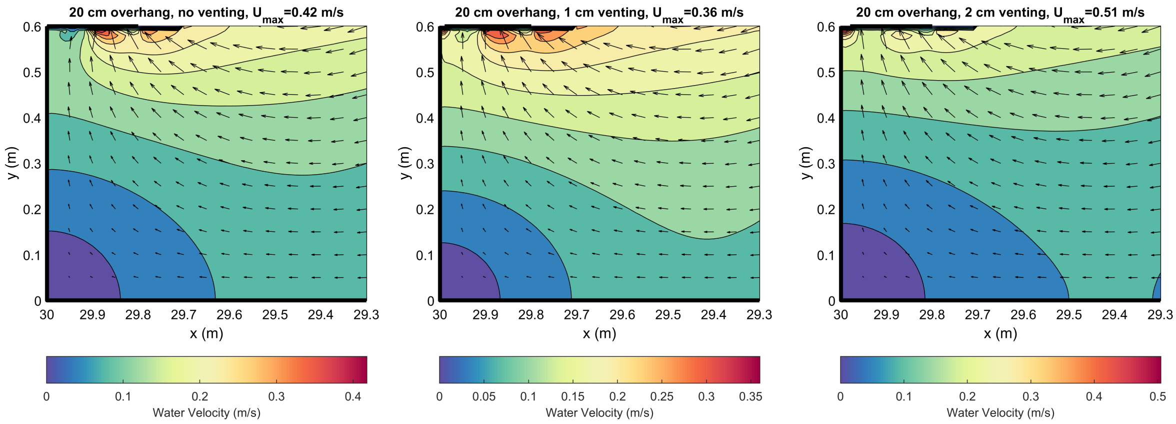

Figure 5.5: Side view of velocity fields in Cases 2a (left), 2b (middle) and 2c (right) at $t = 40.40$ s.

The presence of ventilations creates a region of increased velocities, slightly altering the mean impact velocity. As the fluid enters the smaller cross-section, it has to speed up due to the principle of mass conservation. This velocity raise is believed to be related to higher force peaks with shorter impact durations observed for cases including venting holes, when compared against cases without openings.

By increasing the resolution of the plot near the gap (see Figure 5.6), it is possible to notice a sudden decrease of velocities below the overhang, until zero velocity is reached in a thin layer close to the surface. The same behaviour is predicted by Wood & Peregrine (1996) for velocities immediately after impacts.

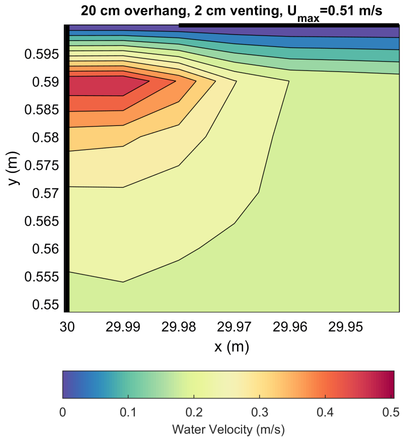

Figure 5.6: Decrease of velocity near the overhang and concentration of larger velocities due to ventilations.

Probes 1, 11 and 12 are used to measure vertical impact velocities along the overhang length. But the measurements were found to indicate localized particle velocities instead of a representative impact velocity associated with the entire water mass colliding with the overhang. Probe velocities exhibit high peaks in a similar fashion to pressure measurements, but in slightly different impact instants for each probe location, since not every water particle hits the exposed surface at the same time. A resultant measured velocity U_M is obtained through integration of the probe velocities along the overhang, and collecting the peaks relative to each impact. This approach is far from perfect due to the insufficient amount of probes both in overhang length and width, but produces results that are more similar to the theories. Figure 5.7 displays the resultant velocities for impact simulations on overhangs of 10 *cm*.

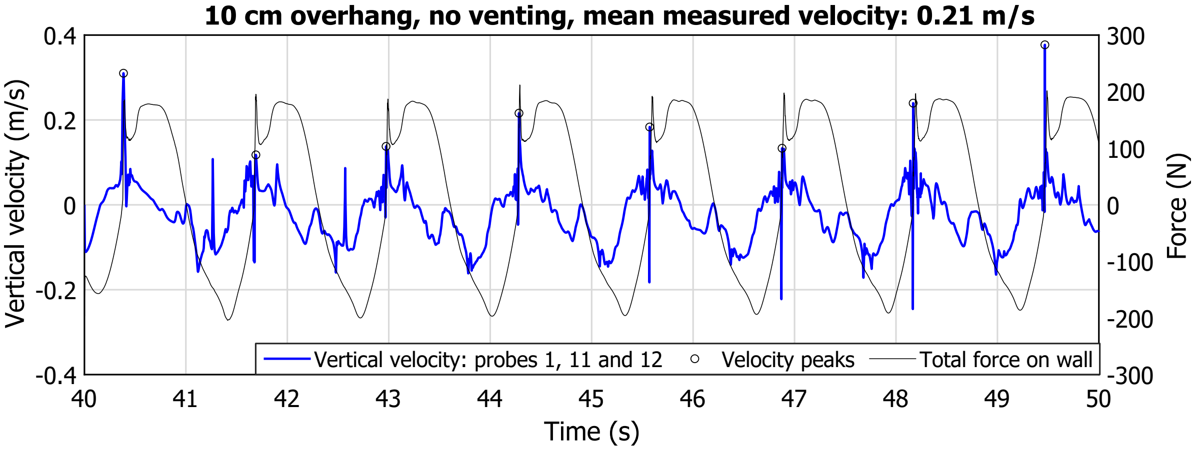

Figure 5.7: Measured vertical impact velocity U_M from Probes 1, 11 and 12 (Case 1a).

Another approach is to derive the vertical impact velocity from the surface elevation measurements at Wave gauge 2, located 20 *cm* from the wall. To calculate each derived impact velocity U_D, the derivative of the measured surface elevation is taken with respect to time and then filtered with a Butterworth filter with 2.0 *Hz* cut-off frequency for $\overline{L_o} = 10\ cm$ and 1.6 *Hz* cut-off frequency for $\overline{L_o} = 20\ cm$, the same previously applied to separate impulsive loads. The results are depicted in Figure 5.8. Even though this method seems more reliable than using the probe measurements, there are still uncertainties regarding how well the surface elevation measurement at one point could represent the entire wave below the overhang. Also, the effects of ventings over the velocity field is not directly captured. The second derivative of surface elevation with respect to time gives very high peak accelerations around the moment of each impact, reaching values above 200 and 700 m/s^2 for 10 and 20 cm overhangs, respectively.

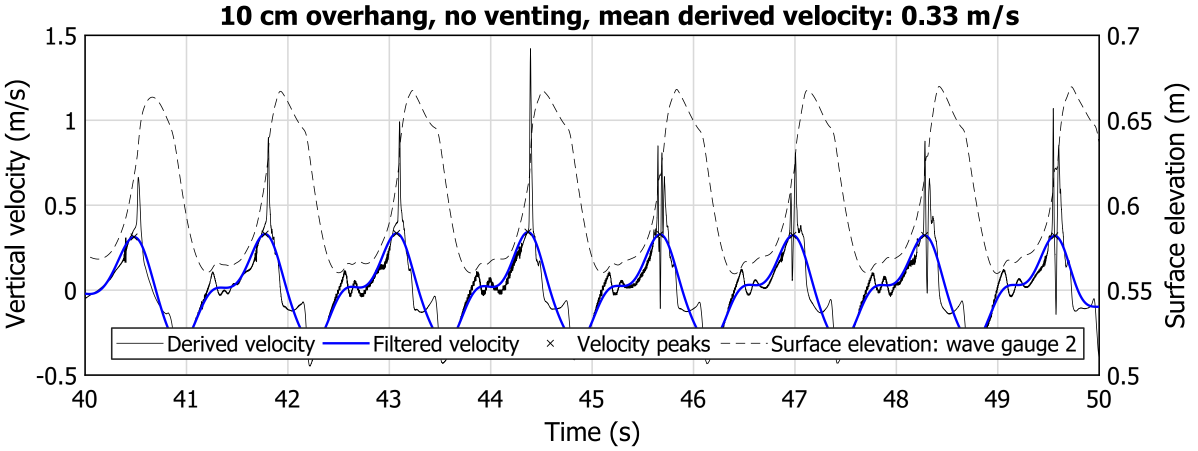

Figure 5.8: Derived vertical impact velocity U_D from Wave gauge 2 (Case 1a).

Table 5.4 lists the measured and derived vertical wave impact velocities for each case, along with relative changes compared to the standing wave theories. Measured velocities increase in the presence of venting holes, consistently with the velocity field data. But the least discrepancies are found between the derived method and wave theories. The Airy wave theory, for its simplicity, seems to be a suitable alternative to determine vertical wave impact velocities. In Appendix F, graphs comparing measured and derived velocities are available for all main cases.

Table 5.4: Measured and derived velocities for each case, compared to standing wave theories.

			U_M Relative changes			U_D Relative changes		
Case	U_M (m/s)	U_D (m/s)	Airy	Tadjbakhsh	Sobey	Airy	Tadjbakhsh	Sobey
1a	0.21	0.33	35%	34%	36%	0%	0%	2%
1b	0.23	0.33	31%	31%	32%	0%	0%	2%
2a	0.19	0.25	43%	41%	41%	24%	22%	23%
2b	0.31	0.29	5%	2%	3%	11%	8%	9%
2c	0.12	0.28	63%	62%	63%	15%	12%	13%

5.4. Pressure-impulses along the wall

Simulated pressure distributions along the wall height are retrieved from Probes 1 to 10, at cross-sections parallel to the middle of the venting hole and to the simulated slice farthest away from the hole, 12.5 *cm* distant. Figures 5.9 and 5.10 show the pressures for a particular impact relative to the Case 1, with $\overline{L_o} = 10$ *cm*, including and excluding ventilations.

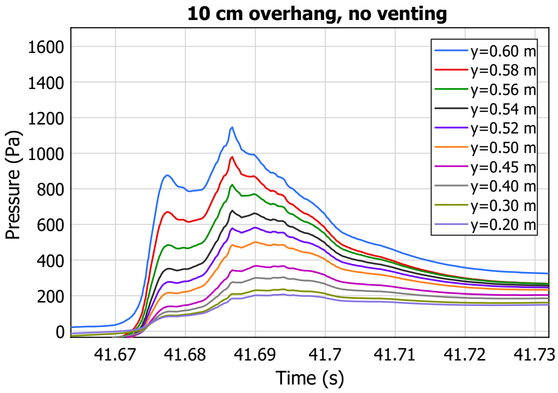

Figure 5.9: Distribution of pressures measured by probes along the wall height for $\overline{L_o} = 10$ *cm* and no venting.

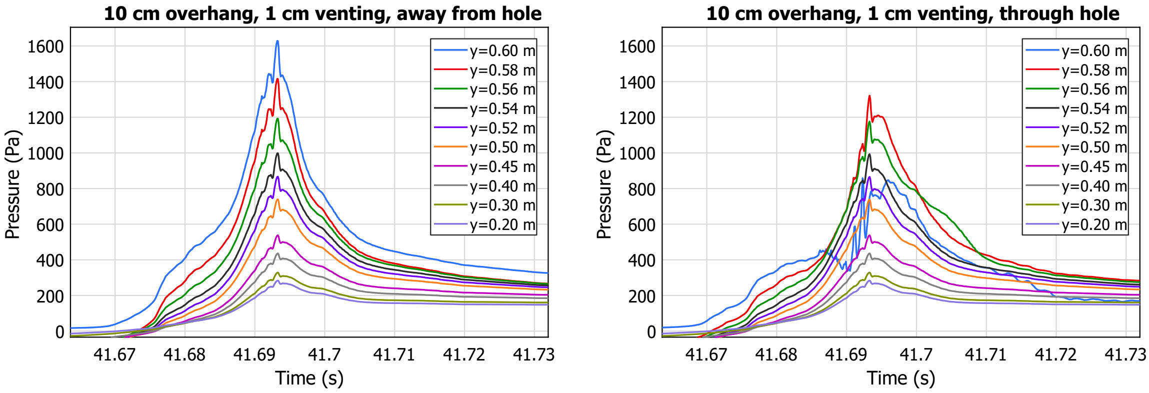

Figure 5.10: Distribution of pressures measured by probes along the wall height for $\overline{L_o} = 10$ *cm* and $\overline{L_h} = \overline{W_h} = 1$ *cm*. Probes are located in the cross-sections away from the venting hole (left) and through the hole (right).

In the situations without venting and at the section away from the hole, it is noticeable how the pressures gradually increase at higher locations and reach their maximum at $y = \overline{L_y} = 60$ *cm*. Interestingly, even though the peaks are higher away from the hole and the overall shape of the pressure signals differ greatly between both, the areas below the pressure distributions of each probe are approximately equivalent.

In the situation with venting, at the section through the middle of the hole, there are visibly reduced pressures measured by Probes 1 and 2, above the height of $y = 58$ *cm*. There is an intense release of pressure recorded by Probe 1 and, since this is the location where the highest pressure peak occurs, it is evident that the venting hole is designed in the most efficient position for pressure release.

Using Butterworth filters as described in Section 5.1, the simulated impulsive and quasi-static pressures are separated for each height to calculate pressure-impulses. For 10 and 20 *cm* overhangs, 2.0 and 1.6 *Hz* cut-off frequencies are utilized, respectively. The maximum dimensional pressure-impulse is taken as $\overline{P_{max}}$ and the total impulse at wall $\bar{I}$ is determined through integrating the pressure-impulses over the wall height, according to the expression

$$\bar{I} = \int_0^{\overline{L_y}} \bar{P} dy \approx P_n A_n, \tag{5.3}$$

where P_n and A_n are the pressure-impulse and area of influence per meter wide relative to each n Probe. Notice that the relationship between maximum pressure-impulse and total impulse is analogous to that between peak pressure and peak force.

To compare the simulated results with the theoretical mathematical model covered in Chapter 3, the dimensionless pressure-impulses P are converted to dimensional $\bar{P}$ with the equation

$$\bar{P} = P \rho U \overline{L_o}. \tag{5.4}$$

Similarly, the dimensional total impulse at wall $\bar{I}$ from the theory are then obtained from the dimensionless impulse I through the relationship

$$\bar{I} = I \rho U \overline{L_o}^2. \tag{5.5}$$

Among the vertical impact velocities U presented in Section 5.3, the best agreement between models are found using the derived velocities $U_D = 0.33$ *m/s* and $U_D = 0.25$ *m/s* for 10 and 20 *cm* overhangs, respectively. The velocities are constant for each overhang length, therefore it is assumed that the ventilations does affect significantly the impact velocity. This prevents inconsistencies in the conversion process.

Figures 5.11 and 5.12 compare dimensional pressure-impulses from CFD simulations and the theoretical model. Only the first simulated impact of each simulation is considered. There is good agreement between pressure-impulses along the wall, specially from bottom to the height of $y = 54$ *cm*. Above this height, the theoretical model consistently overestimate pressure-impulses for cases without venting and at sections away from the hole. At the section through the hole, the theory indicates a much larger release of impulse at the top of the wall than the CFD results suggest. These differences are related to the difficulties to predict peak impulsive forces due to wave impacts. However, if the total impulse over the wall is considered, the agreement between models is satisfactory.

Table 5.5 compares simulated and theoretical maximum pressure-impulse results. It is noticeable how different these predictions are, in particular for cases of 10 *cm* overhangs without venting and at the section away from it, with 75% relative error. The theory implies higher pressure-impulses than simulated values when venting is not present. This could be achieved with higher peaks or longer impact durations. But the theory also estimates lower pressure-impulses than CFD results if venting is applied. Negative release values for Cases 2b and 2c away from hole indicates a very small increase of maximum pressure-impulse relative to the case without venting. Since CFD results were validated against experimental data in Section 4.2.3 with good pressure-impulse agreement, the current theory probably present less realistic results in the impact zone. Also, the CFD model is more robust and includes air and wave shape effects.

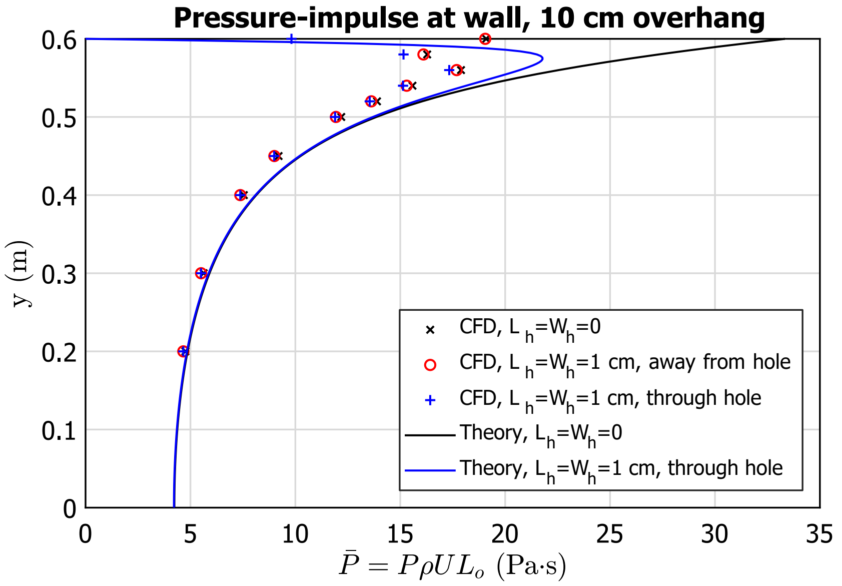

Figure 5.11: Validation of simulated and theoretical pressure-impulses along the wall for Case 1.

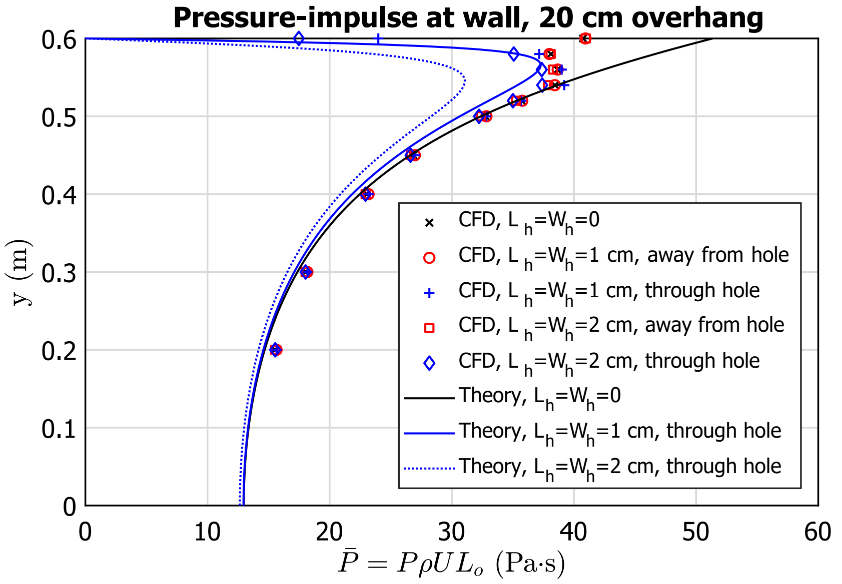

Figure 5.12: Validation of simulated and theoretical pressure-impulses along the wall for Case 2.

Table 5.5: Validation of simulated and theoretical maximum pressure-impulses for the first impact in all cases.

Case	U (m/s)	$\bar{P}_{max,CFD}$ (Pa·s)	$\bar{P}_{max,Theory}$ (Pa·s)	Error	$R_{P,CFD}$	$R_{P,Theory}$
1a	0.33	19.09	33.33	75%	—	—
1b, away from hole	0.33	19.05	33.33	75%	0%	0%
1b, through hole	0.33	17.33	21.78	26%	9%	34%
2a	0.25	40.74	51.36	26%	—	—
2b, away from hole	0.25	40.95	51.36	25%	-1%	0%
2b, through hole	0.25	39.21	37.28	5%	4%	27%
2c, away from hole	0.25	40.97	51.36	25%	-1%	0%
2c, through hole	0.25	37.40	31.06	17%	8%	40%

Regarding total impulses at wall, theory and simulations are reasonably aligned, as seen in Table 5.6. The average relative error between all cases is 9%. Release of pressure-impulse due to venting is detected by the CFD model, but only in minor quantities. This is presumably due to the very low venting area to overhang surface area ratio. In Case 2b, for instance, only 0.2% of the total overhang surface area is vented. Additional simulations are performed for $\overline{L_o} = 10$ *cm* in Section 5.5 to test this hypothesis and increase the relative venting area by reducing the spacing between holes.

Table 5.6: Validation of simulated and theoretical total impulses for the first impact in all cases.

Case	U (m/s)	$\bar{I}_{CFD}$ (N·s/m)	$\bar{I}_{Theory}$ (N·s/m)	Error	$R_{I,CFD}$	$R_{I,Theory}$
1a	0.33	4.67	5.31	14%	—	—
1b, away from hole	0.33	4.58	5.31	16%	2%	0%
1b, through hole	0.33	4.46	4.90	10%	5%	8%
2a	0.25	13.33	13.04	2%	—	—
2b, away from hole	0.25	13.39	13.04	3%	0%	0%
2b, through hole	0.25	13.23	12.04	9%	1%	8%
2c, away from hole	0.25	13.27	13.04	2%	0%	0%
2c, through hole	0.25	12.94	11.07	14%	3%	15%

The final results for Cases 1a and 2a slightly deviate from the results shown in Section 5.1 for two main reasons. First, the total impulses and maximum pressure-impulses were obtained by averaging all 8 impacts instead of only the first impact. Second, only the total forces on the wall were filtered before obtaining the pressure-impulse. Now, the pressures from each probe are filtered individually, and the total impulse is determined by integrating the pressure-impulses along the wall height. This allows a more detailed assessment and comparison between models. In Appendix G, individual comparisons of pressure-impulse along the wall are available for each case, considering the first impact and an average between 8 impacts.

5.5. Venting spacing effects

So far, all presented CFD simulations have been performed with fixed spacing of $2\overline{W} = 25$ *cm*, where $\overline{W}$ is the dimensional simulated domain width. Additional simulations with smaller spacing are conducted to investigate the effects of higher relative venting areas $\overline{A_h}/(\overline{L_o}\bar{S})$, while keeping the venting dimensions constant. In this analysis, the gap length and width are $\overline{L_h} = \overline{W_h} = 1$ *cm*, with overhang length $\overline{L_o} = 10$ *cm*.

Figure 5.13 depicts the first simulated impact for spacings between ventilations of 1, 5, 10 and 25 *cm*. Since $\bar{S} = 1$ *cm* is equal to the venting width $\overline{W_h}$, this situation is equivalent to a venting with infinite width and therefore was modelled in 2D. It can be noted from the total force distribution that less spacing between venting openings leads to shorter impact durations, which leads to release of impulses. Also, the effects of pressure relief due to venting are widespread between sections along the width of the simulated domain, or the z direction. As it has been depicted in Figure 5.10, the largest difference between sections through and away the venting hole occurs locally at the gap position, measured by Probe 1 in the corner between the overhang and vertical wall. But the local pressure release affects only approximately 2% of the wall height (1 *cm* over 60 *cm*), hence the small difference in total force away and through venting.

The distribution of pressure-impulses along the water depth in Figure 5.13 depicts a gradual reduction of pressure-impulses as the spacing between venting holes decreases. But this decrease is less intense than suggested by the theory, which is evidenced when $\bar{S} = 1$ *cm*. This trend was also identified when validating all simulated cases in Section 5.4. Maximum pressure-impulse, total impulse and their release quantities compared to the case without venting, for each spacing between holes, are listed in Table 5.7. At sections through hole, the release of maximum pressure-impulse is always higher than

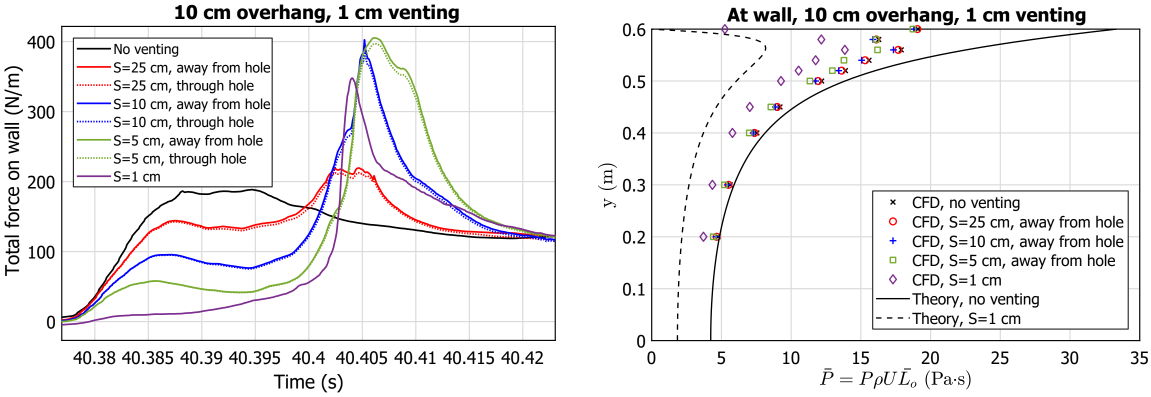

Figure 5.13: Zoomed in view of total simulated force peaks on the wall and pressure-impulse distribution along height for different spacings between ventings of $\overline{L_h} = \overline{W_h} = 1$ *cm*.

the release of total impulse. But total impulse release dominates at sections away from the opening.

Table 5.7: Effects of spacing in the release of maximum pressure-impulse and total impulse. In all cases, $\overline{L_o} = 10$ cm and $\overline{L_h} = \overline{W_h} = 1$ cm.

Section	$\bar{S}$ (cm)	$\overline{A_h}/\bar{S}^2$	$\overline{A_h}/\bar{S}\overline{L_o}$	$\overline{I_{CFD}}$ (N·s/m)	$\overline{P_{max}}$ (Pa·s)	$R_{P,CFD}$	$R_{I,CFD}$
Through hole	1	100.00%	10.00%	3.49	13.85	27%	25%
Away from hole	5	4.00%	2.00%	4.34	18.73	2%	7%
Through hole	5	4.00%	2.00%	4.25	16.19	15%	9%
Away from hole	10	1.00%	1.00%	4.52	18.80	2%	3%
Through hole	10	1.00%	1.00%	4.41	17.23	10%	5%
Away from hole	25	0.16%	0.40%	4.58	19.05	0%	2%
Through hole	25	0.16%	0.40%	4.46	17.33	9%	5%

These results are compared to empirical fits from the pressure-impulse model in Section 6.1.

6

Discussion

This chapter has the objective to explore engineering design approaches for the case of wave impacts on overhanging vertical structures with ventilations and review main findings and limitations from the modelling performed in previous chapters. Section 6.1 evaluates empirical relations found in Chapter 3. Sections 6.2, 6.3 and 6.4 address research sub-questions 1, 2 and 3, respectively.

6.1. Ventilation assessment formulas

In Section 3.3, empirical formulas were developed to assess the performance of ventilations on coastal structures. They arise from the variation of geometrical and ventilation parameters in the three-dimensional pressure-impulse model. In this Section, these formulas are tested against simulated CFD results.

Consider wave impacts in Case 1, with a wall 60 cm high and overhang 10 cm long. The dimensionless wall height is given by $L_y = \overline{L_y}/\overline{L_o} = 0.60/0.10 = 6$. The dimensionless maximum pressure-impulse at wall due to wave impacts on the deck, without venting, can be estimated by Equation 3.2 as $P_{max,0} \approx 1$, since $L_y > 2$.

The dimensionless total impulse at wall without venting is obtained by Equation 3.3 as

$$I_0 = 0.8844 L_y^{0.3456} = 0.8844 \cdot 6^{0.3456} = 1.64. \tag{6.1}$$

To provide physical meaning to the maximum pressure-impulse and total impulse, they need to be converted to dimensional quantities through Equations 5.4 and 5.5. Using $U = 0.3259$ *m/s* from Section 5.3 and $\rho = 1000$ kg/m^3, the expressions are described as

$$\overline{P_{max}} = P_{max}\rho U \overline{L_o} = 1 \cdot 1000 \cdot 0.3259 \cdot 0.1 = 32.59 \text{ Pa} \cdot \text{s}, \tag{6.2}$$

$$\overline{I_0} = I_0 \rho U \overline{L_o}^2 = 1.64 \cdot 1000 \cdot 0.3259 \cdot 0.1^2 = 5.34 \text{ N} \cdot \text{s}/m. \tag{6.3}$$

The same procedure is done for Case 2, with $\overline{L_o} = 20$ cm. Table 6.1 summarizes the results for both cases using the formulas and compares them the pressure-impulse theory and to CFD simulations, considering an average between 8 simulated impacts. Formula estimations are converted to dimensional form using the same process explained in Section 5.4. The total impulse and maximum pressure-impulse formulas are very close to the solutions obtained from the pressure-impulse theory, with the advantage that it is not necessary to solve the Laplace equations. Between formula and CFD outcomes, the average maximum pressure-impulse relative error is 34% (see Table 5.5), while for total impulses the average is only 9% (see Table 5.6).

Table 6.1: Comparison between formula, theory and simulations results. Pressure-impulses units in Pa·s and total impulse units in N·s/m (Case 1).

	Formula				Theory		Simulation	
	P_{max}	I_0	$\overline{P_{max}}$	$\overline{I_0}$	$\overline{P_{max}}$	$\overline{I_0}$	$\overline{P_{max}}$	$\overline{I_0}$
Case 1	1	1.64	32.59	5.34	33.33	5.31	19.90	5.02
Case 2	1	1.30	49.50	12.83	51.36	13.04	41.01	13.33

Figure 6.1 compares the simulated total impulse at wall against empirical fit predictions from Equation 3.3. Very good correspondence is found for both cases with 10 and 20 *cm* overhangs, without venting.

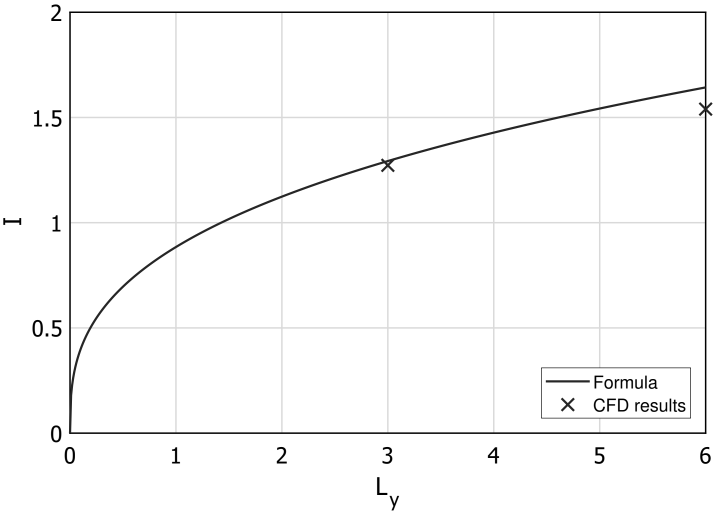

Figure 6.1: Dimensionless total impulse predicted by formula and CFD simulations.

To consider the effects of ventilations on the wave impacts, the pressure-impulse model derived relations from Equations 3.6 and 3.7 provide the release of pressure-impulse only at the section away from hole, since it is the critical section where the largest impacts occur. The release quantities are largely dependent on the spacing between ventilations $\overline{S}$. Applying these relations to Case 1b, with 10 *cm* overhang and 1 *cm* venting length, yields

$$R_P = \frac{213.80\left(\frac{A_h}{SL_o}\right) - 9.59}{\left(\frac{A_h}{SL_o}\right) + 29.20} = \frac{213.80\left(\frac{1\cdot 1}{25\cdot 10}\cdot 100\right) - 9.59}{\left(\frac{1\cdot 1}{25\cdot 10}\cdot 100\right) + 29.20} = 2.56\%, \tag{6.4}$$

$$R_I = \frac{163.30\left(\frac{A_h}{SL_o}\right) + 18.48}{\left(\frac{A_h}{SL_o}\right) + 18.00} = \frac{163.30\left(\frac{1\cdot 1}{25\cdot 10}\cdot 100\right) + 18.48}{\left(\frac{1\cdot 1}{25\cdot 10}\cdot 100\right) + 18.00} = 4.55\%, \tag{6.5}$$

where $\overline{Ah} = \overline{L_h}\overline{W_h} = 1$ *cm*^{2}. These results mean that, according to the pressure-impulse model, there are releases of 2.56% and 4.55% of maximum pressure impulse and total impulse at the section away from the gap. Since the pressure-impulse model tends to greatly overestimate venting release results when compared to simulations, the same occurs with the empirical fit predictions. Simulated effects from venting holes are much more localized than described by the theoretical model. Table 6.2 lists the results obtained using the formula and simulated data.

Table 6.2: Comparison between maximum pressure-impulse and total impulse releases predicted by empirical fit and CFD simulations. In all cases, $\overline{L_o} = 10$ cm and $\overline{L_h} = \overline{W_h} = 1$ cm at section away from hole.

$\bar{S}$ (cm)	$\overline{A_h}/\bar{S}\overline{L_o}$	$R_{P,Formula}$	$R_{P,CFD}$	$R_{I,Formula}$	$R_{I,CFD}$
1	10.0%	54.3%	27.4%	59.0%	25.2%
5	2.0%	13.4%	1.9%	17.3%	7.0%
10	1.0%	6.8%	1.5%	9.6%	3.3%
25	0.4%	2.6%	0.2%	4.6%	1.9%

Simulated results from Case 1 suggest a correlation between relative venting area and total impulse release, similarly to the pressure-impulse theory results (Figure 6.2). The relationship occurs both for sections away and through the venting holes. The graph compares empirical relations used to predict release of total impulse, derived from each model. The fitted curve corresponding to CFD results at the section away from hole is given by

$$R_P = \frac{78.69\left(\frac{A_h}{SL_o}\right) + 2.42}{\left(\frac{A_h}{SL_o}\right) + 21.29}. \tag{6.6}$$

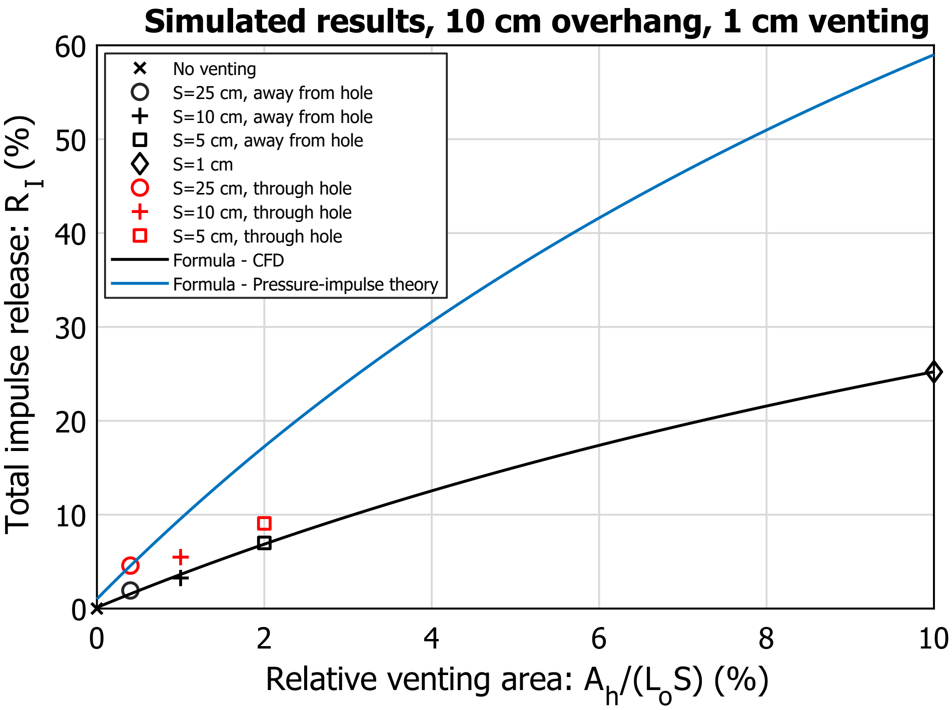

Figure 6.2: Comparison between empirical relations from CFD and pressure-impulse theory for Case 1.

In summary, after validation of the pressure-impulse and CFD models, only the formula to determine total impulse without venting indicates good correspondence between both models. Regarding release estimations including venting holes, further improvements are required in the pressure-impulse model before a better relationship can be derived. Therefore, the empirical relations of pressure-impulse release from CFD results are preferred over the theoretical results.

6.2. Pressure-impulse model discussion

The predictability of pressure-impulses on overhanging coastal structures with ventilations using the theoretical model is evaluated in this Section, addressing the research sub-question 1.

In order to include openings in the structure which receives wave impacts, a finite difference scheme is developed to solve the Laplace equation with modified boundary conditions, in two and three dimensions. When compared to the analytical solution by Wood & Peregrine (1996), without venting, numerical errors below 1% are found for well refined grids, as seen in Table 3.1. The refinement study is performed by making the grid progressively finer and setting the average difference between iterations as the tolerance parameter. To achieve proper number of iterations and grid cells for accurate results requires extensive computational power, especially in three-dimensional cases.

Conversion from dimensionless to dimensional pressure-impulse quantities introduces a new source of error in the determination of vertical impact velocities. Standing wave theories are employed following guidelines from Wood (1997) regarding positioning of the velocity distribution and consideration of the overhang length. Also, wave theories predict horizontal surface elevation at the moment of impact, when water depth is equivalent to wall height. This matches assumptions from the pressure-impulse model and simulated results (Figure 6.3). Theoretical velocities are in good agreement with simulated data (Table 5.4) and estimations from Mao (2019). But improvements are possible if the wave reflection effects at the wall were investigated with more depth.

Figure 6.3: Approximately horizontal surface elevation shortly after the moment of impact.

Using simulated probe measurements to gather velocities which represent the entire water mass collision is difficult due to limited number of probes, large variations of intensity and slightly different impact instants between probes. Both probe and velocity field data indicate that flow velocities are much higher at the positions of venting holes than along the overhang length. The attempt to calculate an average velocity using only three probes along the overhang did not yield reliable results. Measuring with more probes would provide more information about velocities, although no clear procedure to process this data has been found, especially when such high accuracy is required. Therefore, other methods are preferred in this study.

An improved approach is to derivate velocities from recorded surface elevations near the region of impact, but away from the overhang to avoid flow disturbances. This method produces short, high-intensity velocity peaks that resemble impulsive force peaks, as shown in Figure 5.8. There seems to exist an impulsive and quasi-static behaviour in the derived vertical velocities, since applying exactly the same filters to separate impulsive and quasi-static forces provides reasonable impact velocity estimators. The derived velocities for the cases without venting provides the best agreement for validation of theoretical pressure-impulses with simulations.

A major basic assumption from the pressure-impulse model is that gravity is neglected during the short impact duration (Wood et al. (2000)). To verify this notion, fluid accelerations are deducted as the second derivative of the surface elevation. Peak accelerations around the impact instants are found to be much larger than $10g$, which supports the theory (Figure 6.4).

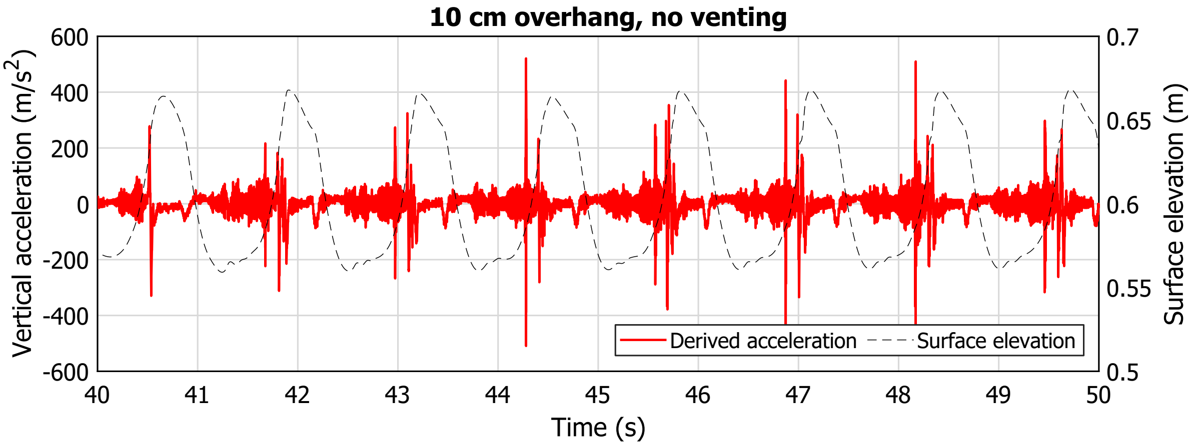

Figure 6.4: Derived vertical impact accelerations from Wave gauge 2.

Comparing theoretical and simulated pressure-impulses along the structure wall height exposes discrepancies in the region near the overhang, as shown in Figures 5.11 and 5.12. When venting is not considered, above the depth of 55 *cm* there is a steep increase of pressure-impulse predicted by the theoretical model, which is not followed by the simulated results. This reflects in large errors among maximum pressure-impulses. However, below 55 *cm*, there is good agreement between models, which leads to total impulse errors below 16% (Table 5.6) among all cases, considering only the first simulated impact.

When venting is included in the theoretical model, the release of pressure-impulse is much larger than what is observed in the simulations, independently of the geometry of the structure, venting dimensions and spacing between holes. This overestimation is caused by the local boundary condition, which assumes null pressure-impulse at the gap. Even though this condition is appropriate at the free surface away from the overhang, as defined by Wood & Peregrine (1996), it is not realistic for small holes. Simulated probe measurements at the venting position indicate a significant decrease in local pressures, but they still are larger than zero.

For small spatial steps around the venting region, the neglected convective acceleration terms $(\vec{u} \cdot \nabla)\vec{u}$ in the derivation of the pressure-impulse theory become important (Equation 2.11), affecting the validity of the simplified Laplace equation to describe pressure-impulses with venting. These convective terms are related to the change of flow velocity due to spatial effects and are commonly considered in nozzle design (Elger et al. (2012)). Since the Navier-Stokes equations include convective acceleration terms, the CFD model is more complete to describe fluid flows with venting holes.

6.3. CFD model discussion

Computational fluid dynamics is applied to investigate the mitigation of impulsive loadings on vertical structures due to wave impacts on overhanging elements through the use of ventilations, answering research sub-question 2.

As shown in Figure 4.7, simulated impulsive forces due to wave impacts are largely dependent on mesh size and time step. Convergence is found by increasing refinement levels, especially in the region around the corner between wall and overhang, where venting holes are positioned. To reduce numerical uncertainties, all simulated cases have equal mesh refinement. Allowing adaptive time step using the Courant number produces more stable simulations than fixing a constant value. Simulated quasi-static loadings remain virtually unchanged across different mesh variations.

Validation between simulations and experimental results demonstrated good agreement between forces and generated waves for both overhang lengths (Figure 4.7). By comparing numerical and experimental force signals, it can be noticed that the overall force shape and time intervals between impacts are very similar.

Overhang length has substantial effect over the magnitude of simulated impulsive force peaks and impulses, although quasi-static loadings are more or less stable (see comparison in Figure 6.5). The impulsive phenomenon is not associated with wave breaking conditions, but with flow deflection instead, confirming Castellino et al. (2018) conclusions. And longer overhangs deflect more water mass, inducing higher wave loads. This increase leads to higher pressure-impulses, in accordance with the theoretical model.

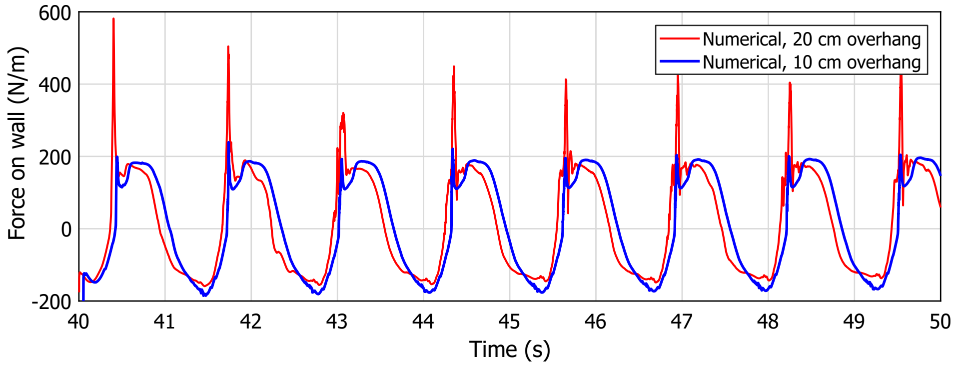

Figure 6.5: Simulated impact forces for 10 and 20 *cm* overhangs (Cases 1a and 2a).

A key limiting factor in the CFD modelling is the high computational power demanded to perform numeric calculations. Since impulsive loads occur in extremely short time intervals, it is essential that the simulation time step is low enough. For stability reasons, if the time step is reduced, the mesh resolution has to increase proportionally. Furthermore, there are three length scales that needs to be resolved properly: the wave propagation scale, in *m*, the structural scale, in *cm* and the venting scale, in *mm*. Numerous tests were conducted to optimize the mesh efficiency without compromising the integrity of the results. For simulations including venting holes with limited width, the computational domain must be three-dimensional. These simulations require several days to complete, even using cluster computing and optimized meshes. In one of the simulations with venting, the increased flow velocity would decrease the time step to prohibitively low values, due to the Courant stability criterion. Therefore, only the first impact results are considered for cases including ventilations.

The limited amount of impact samples may undermine the statistical significance of simulated results. Regression analysis and extreme value analysis are some tools utilized to deal with the stochastic nature of wave impacts (Renzi et al. (2018), Chen et al. (2019)). Due to computing challenges, statistical analysis of CFD simulations has been neglected in this study.

Reliably splitting impulsive and pulsating processes is one the main weaknesses of the analysis. Theoretical quasi-static force distributions overestimate simulated results, notably using Sainflou's formula. This overprediction endorses observations from Rundgren (1958), after conducting physical modelling tests (Kisacik (2012)). Low-pass Butterworth filters perform generally better compared to experimental data and can be used successfully across different probes along the wall height without adjustments.

According to Chen et al. (2019), the filtering cut-off frequency depends on the wave motion. In this study, since wave conditions are constant for all simulations, the optimal filter frequency has found to be also affected by the overhang length, due to its influence on the magnitude of impacts. The ratio between impulsive and quasi-static force peaks F_p/F_{qs} might be an useful parameter to optimize this splitting method. Moreover, increasing the force interpolation sampling rate from 1000 *Hz* to 10000 *Hz* significantly enhanced the splitting results.

Unexpectedly, peak total impulsive forces are found to often increase with the use of ventilations, both at sections through and away from the openings (Figure 5.3 middle and right). This phenomenon is probably associated with the increased velocities at the hole, responsible for the upward water jet flow after the wave impact. However, the rate to which forces increase and decrease are higher, causing a narrower peak. This leads to a decrease in the total area of the force during the impact, the total impulse. A similar effect has been observed in Xiao & Guo (2018), which measured local amplification of pressures using air relief openings (ARO) to mitigate wave impacts on bridge girders (Figure 6.6).

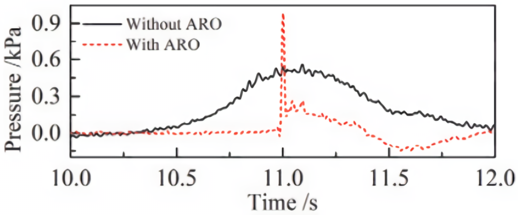

Figure 6.6: Local amplification of pressures due to air relief openings (Xiao & Guo (2018)).

CFD results indicate two main factors that induce impulse reduction due to venting. Firstly, there is a local reduction of pressures near the hole, clearly demonstrated in probe measurements at the corner between overhang and wall, at the section through hole (Figure 5.10). The influence of this release is evidenced by the fact that total impulses at the section through venting are always smaller than away from the openings. Secondly, there is a widespread reduction of pressure-impulse controlled by the spacing between ventilations (Figure 5.13). This decrease affects the entire structure width and is proportional to the relative venting area $\overline{A_h}/(\overline{L_o}\overline{S})$, as depicted in Figure 6.2.

Wood et al. (2000) emphasizes the role of trapped air on wave impacts. At the moment of collision, air bubbles are contracted by the body of water and then expand, making the water flow to bounce back. This rebound of the water mass leads to higher impulses. Bagnold (1939) studied this phenomena, and found that the pressure impacts are larger for smaller air pockets, which was observed also by Mao (2019). Since air is assumed incompressible in the simulations, the bounce back effect is not reproduced. Consequently, this could be the reason for lower simulated impulsive forces against experimental data (Figure 4.7) and lower simulated pressure-impulses near the surface compared to the theory (Figures 5.11 and 5.12). Higher impulses close to the impact region due to entrapped air could also mean larger impulse releases and therefore better performance from venting holes in the simulations. The distortion associated with air compressibility between model and prototype scales is another consequence of air entrapment, introducing scale effects not only in numerical simulations, but also experimental tests (Takahashi et al. (1985), Seiffert et al. (2015)).

6.4. Design applications

This Section adresses research sub-question 3, on how to apply results from pressure-impulse and computational fluid dynamics models in the engineering design of overhanging coastal structures subject to wave impacts including ventilations. This question is explored by looking at practical examples where the models apply and which structural elements are involved.

The main contributions from this study are to test and compare methodologies to determine design loadings in vertical walls due to wave impacts on horizontal elements and quantify the use of venting holes to relieve these impacts. In practice, the walls can represent steel gates such as the Afsluitdijk flood gates or Terneuzen lock complex in the Netherlands (Figure 6.7). These slender structures are particularly vulnerable to wave impacts due to their dynamic response.

In engineering design of coastal structures subject to wave impacts, the maximum pressure-impulse and total impulse can be utilized to determine peak pressure or forces using Equation 5.2 by assuming a triangular impact force time series. After testing in Section 5.2, it has been found that this method does not reliably predict simulated peak impulsive forces. Not only the impact force shape differs from

Figure 6.7: Sluice gates from the Terneuzen lock complex in the Netherlands (Gelders Staalstraal- en Schildersbedrijf B.V. (2019)).

a regular triangle, but also the correct determination of the impact duration is subject to uncertainties in the impulse splitting process.

In both CFD and pressure-impulse models, the accuracy of total impulse estimations is much higher than maximum pressure-impulse for all cases, attested through validation of experimental results and comparison between models. This is related to the unpredictability of peak forces, even for identical wave impacts, which has been well-documented in the literature (Bagnold (1939), Hofland et al. (2011)).

Instead of utilizing peak impulsive forces F_p, Chen et al. (2019) proposes to use the total impulse $\bar{I}$ directly as a design input for coastal structures subject to wave impacts, combined with quasi-static forces F_{qs}. Extreme value analysis determines statistically $\bar{I}$ and F_{qs} values for a certain exceedance probability. The design total reaction force F_r then can be assessed with the reformulated dynamic response function

$$F_r = F_{qs} + \bar{I}\omega_n D_f, \tag{6.7}$$

where ω_n is the natural angular frequency of the structure and D_f is the modified dynamic load factor. This factor depends on the ratio between impact duration Δt and natural period of the structure T_n and can be obtained from the design chart depicted in Figure 6.8. The chart is divided in impulsive, dynamic and static loading domains of the structure. The parameter α_r is the ratio between impact rise time t_r and impact duration Δt.

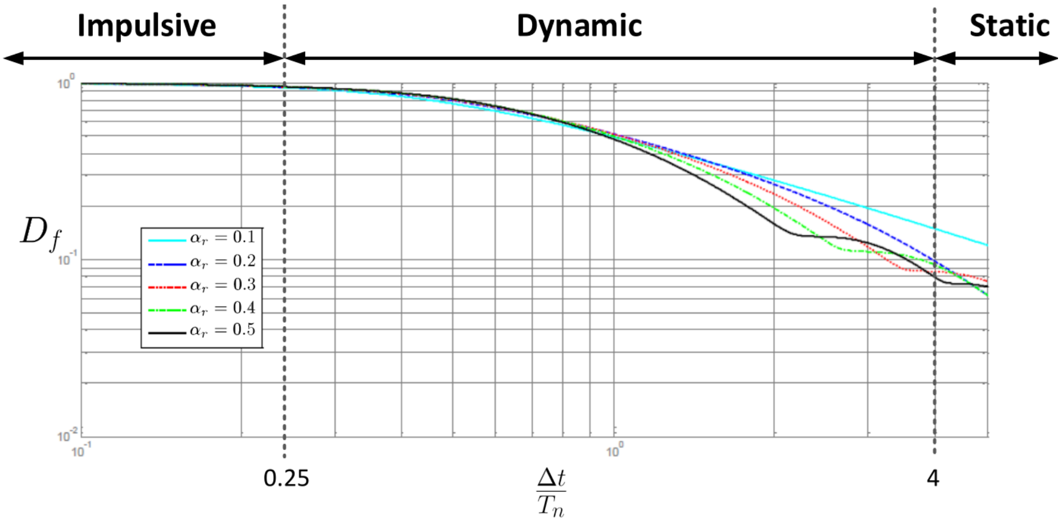

Figure 6.8: Design chart for a single degree of freedom response function based on impact impulse. Adapted from Chen et al. (2019).

As suggested by Chen et al. (2019), this new envisaged method provides an optimized estimation of the structural dynamic response. In the impulsive domain, it is clear from Equation 6.7 that the total impulse release caused by venting also reduces the total reaction force on the structure, leading to safer and more economic designs.

From the work developed and research conducted in this thesis, two simplified design methods for a vertical structure (wall) with venting and subject to wave impacts on the overhang, could be outlined in the following steps:

Pressure-impulse model design method

1. Determine geometric parameters: dimensionless wall height $L_y = \overline{L_y}/\overline{L_o}$, where $\overline{L_y}$ and $\overline{L_o}$ are the dimensional wall height and overhang length, respectively.
2. Determine the ventilation parameters: dimensionless hole length L_h, hole width W_h and spacing between holes S by using $\overline{L_o}$ as the scale factor.
3. Calculate dimensionless total impulse at wall without venting I_0 using Equation 3.3.
4. Derive the release of total impulse due to venting R_I using Equation 3.7 derived from the pressure-impulse model or the more conservative Equation 6.6 derived from CFD simulations.
5. Through Equation 3.5, determine dimensionless total impulse with venting I_{vent}.
6. Find vertical impact velocity U using standing wave theories discussed in Section 2.4 and the methodology from Section 5.3.
7. Convert dimensionless to dimensional total impulse with venting $\overline{I_{vent}}$ with Equation 5.5.
8. The quasi-static force F_{qs} can be determined with linear wave theory, Sainflou or Goda methods from Section 2.1.1.
9. The reaction force at the vertical structure F_r is found using Equation 6.7 and the design chart from Figure 6.8, assuming impulsive loading domain, for a structure with known natural period and frequency.

CFD model design method

1. Set-up numerical model with venting holes, validate and run simulations, as described in Chapter 4.
2. Split resultant impulsive and quasi-static forces through the use of low-pass filters according to instructions in Section 5.1.
3. After the separation, calculate dimensional total impulse with venting $\overline{I_{vent}}$ at the section away from hole, total impact duration Δt and identify peak pulsating forces F_{qs}.
4. As recommended by Chen et al. (2019), perform extreme value analysis of $\overline{I_{vent}}$ and F_{qs}.
5. The reaction force at the vertical structure F_r is found using Equation 6.7 with extreme values and the design chart from Figure 6.8, for a structure with known natural period and frequency.

Nevertheless, further validation and testing with small and large scale physical models are required before these design methods can be applied in engineering projects. Equation 3.7 in special requires additional validation. Empirical relations are only valid for the limits specified in Section 3.3. The CFD model design method can also be used for physical modelling tests.

7

Conclusions and recommendations

This study investigates the influence of ventilations on coastal structures with overhangs under wave impacts. Two main design approaches are explored for several laboratory scale cases, focusing on the impulsive loads caused by standing waves. Firstly, the pressure-impulse model is validated against semi-analytical solutions available in the literature and then modified to include venting holes in three dimensions. Secondly, computational fluid dynamics is employed to assess impact impulses on structures with openings after validation of the model with experimental data excluding venting. Both models are compared and their associated findings, limitations and applicability to engineering design are discussed.

Comprehensive search of the relevant literature has not identified any previous studies about the application of the pressure-impulse theory on the release of wave impacts using ventilations. A novel approach is presented and investigated for the application of the pressure-impulse theory in three-dimensions, allowing for flexibility of geometric and boundary condition specifications. This study represents some progress in the development of sophisticated design tools and measures to mitigate wave impacts on coastal structures. Insights are provided about analysis procedures and guidelines required in the implementation of the models. A contribution also is made to assert the advantages of the pressure-impulse model relative to conventional approaches, which may also extend to the design of other types of coastal structures.

7.1. Conclusions

7.1.1. Main findings

The research sub-questions, posed at the introduction of this thesis, are now answered based on the outcomes of the study:

1. **How can the pressure-impulse model be used to assess the effects of ventilations on overhanging coastal structures?**

   The pressure-impulse model can be successfully adapted to evaluate three-dimensional structural geometries and numerical errors are very small for sufficiently refined grid sizes. There is great potential in the use of the pressure-impulse model for wave impacts on overhanging coastal structures, due to its simplified and reliable way to describe impulsive loads. Pressure-impulses can be evaluated much faster than with CFD models, since the Laplace equation is solved instead of non-stationary Navier-Stokes equations. Comparison to CFD results indicates good similarity for cases without ventilations, but also that further improvements are probably necessary to correctly implement the venting hole boundary condition in the model. Empiric relations can be derived from the theoretical model solutions for rapid assessment of total impulse release using geometrical and ventilation parameters, without the need for computational or physical modelling.

2. **What is the predicted reduction of impulsive wave impact loadings on overhanging coastal structures with ventilations using computational fluid dynamics models?**

   CFD simulations predict a decrease of total impulse on overhanging vertical structures with venting subject to wave impacts. For the cases tested, a correlation is found between simulated impulse releases and relative venting area, controlled by the hole dimensions and the spacing between them. The release of pressure-impulse at the critical section away from the opening ranged from approximately 2% for 0.4% relative venting area to 25% for 10% relative venting area. Compared to the pressure-impulse theory, only modest levels of wave impact impulse mitigation are estimated using CFD.

3. **How to apply the pressure-impulse model and computational fluid dynamics results in the engineering design of coastal structures with venting and subject to wave impacts?**

   For both pressure-impulse and CFD models, distinct design approaches for coastal structures with venting subject to wave impacts are suggested. Applying the pressure-impulse model, all design input variables are determined theoretically. Empirical relations are used to estimate the reduced dimensionless total impulse due to venting from geometrical and ventilation parameters. The conversion to dimensional impulse occurs by employing vertical impact velocities, as described in standing wave theories. Pulsating forces can be obtained from theoretical methods such as the Goda method. Using the computational fluid dynamics results, quasi-static and impulsive loads are separated with low-pass filters. After the total impulse and quasi-static forces are known from either pressure-impulse or CFD models, the reaction force at the structure is determined through a reformulated dynamic response function, which also depends on the dynamic load factor and natural frequency of the structure. Due to model limitations, comparing both design approaches is recommended.

Following the answers to all research sub-questions, the main research question is then addressed:

What are the effects of ventilations in the design of vertical coastal structures with overhangs described by the existing wave impact pressure-impulse theory and computational fluid dynamics?

The pressure-impulse theory and computational fluid dynamics can effectively describe the effects of venting in two and three dimensions. Both models, for all cases tested, demonstrated a relative decrease of total impact impulse on the structure with the inclusion of ventilations. Due to its simplifying assumptions, the pressure-impulse model overestimates by 2 to 3 times the venting mitigation influence on impulsive loads, when compared to simulated results. The CFD model performs better with venting than the pressure-impulse theory due to the inclusion of convective acceleration effects. No significant changes are found for quasi-static pressures acting on the structure. Since the predictability of total impact impulse is demonstrably superior to maximum pressure-impulses, this study endorses using the total impulse as the primary design variable, instead of peak impact forces. As the total impulse is directly applied in the reformulated dynamic response function of the structure, even small levels of impact reduction can make a significant change on the design total reaction force.

7.1.2. Limitations

The assessment of the influence of ventilations on wave impacts involves complex physical processes and requires very high spatial and temporal accuracy. Therefore, limiting assumptions are necessary to implement the models.

Main limiting factors in this study can be summarized as:

- No experimental data including ventilations
- Underlying theoretical model assumptions (pressure-impulse equal to zero at venting boundary)

- Air compressibility neglected (no bounce back effect)
- Impact velocity determination uncertainties
- Inconsistencies in the splitting of impulsive and pulsating loadings
- Numerical method errors
- Wave reflection differences between models
- Measurement inaccuracies
- Low quantity of impact samples
- Constant regular wave and water level conditions
- Scale effects

Even though these limitations are present, this study may be useful as a proof of concept, which could be improved with further research.

7.2. Recommendations

In order to further advance the findings of this report and overcome some of the limitations faced during this study, the following recommendations are suggested for future research:

1. **Carry out laboratory experiments to validate models**

   It is crucial that small scale physical modelling experiments are conducted to provide reference values of wave impact impulse release due to venting, pressure-impulses along the wall and total impulses. Experiments should try to reproduce geometrical and venting parameters such as height of the vertical structure, length of overhang, venting hole width, venting hole length and spacing between ventilations. Standing waves could be generated to simplify the analysis of impact impulses. But testing a wide range of wave and water level conditions is also desirable. Multiple probes and wave gauges can be applied along the wall height and overhang length at sections through and away from the venting hole, as exemplified in this study. The experimental outcomes could be compared to pressure-impulse and simulations results from this thesis. In special, the relationship between relative venting area and total impulse at wall should be investigated.

2. **Pressure-impulse venting boundary condition analysis**

   Calibration of the venting hole boundary condition could improve the theoretical model predictions when validating against physical model measurements or simulated results. Instead of assuming zero pressure-impulse in this boundary, another relationship could be found related to the peak of velocities in the hole, or with a constant associated to the size of the hole or overhang width. Null pressure-impulse is commonly employed for free surface conditions away from the impact region, but simulated measurements indicate that this condition does not hold for small holes, possibly due to the omission of convective acceleration in the mathematical model.

3. **Collect field and large scale data**

   Even though impulsive wave impacts can be extremely high, there is a scarcity of field data available. Pressure measurements could be employed on decks subject to wave impacts from standing waves. Alternatively, large scale experiments in facilities such as the Delta Flume could be conducted (Hofland et al. (2011)). The importance of the field data is to verify how model predictions are reproduced, considering scale effects. According to the literature, distortions can be associated with the influence of entrapped air on wave impacts, since air compressibility cannot be scaled (Takahashi et al. (1985)).

4. **Improve impact velocity derivation method**

   There is a high influence of impact velocities on theoretical pressure-impulses in the conversion process to dimensional quantities, but a precise approach to obtain these velocities, considering effects of the structure and venting holes, is yet to be found. To determine wave impact velocities empirically, Wood et al. (2000) recommends the application of particle image velocimetry, which would produce results similar to the velocity fields obtained in this study, but available at every recorded instant. Wave theories applied in this study demonstrated good potential, but deeper examination of the wave reflection at wall may lead to improved results. Impact velocities could be derived also from known impact forces, as long as the colliding water mass is correctly estimated. The connection between low-pass filters and impact velocities should be elucidated and whether separation between impulsive and quasi-static processes applies also to velocities.

5. **Study relationship between filters and wave loadings**

   Low-pass filters applied to separate impulsive and quasi-static loadings in this study are mostly controlled by the specified cut-off frequency, which varied for different overhang lengths. The dependence of the cut-off frequency with wave length, wave period and structural dimensions could be explored in further studies. Perhaps the ratio between peak impulsive and quasi-static loads can be determinant in the design of filters. Optimization and automation of the splitting method would significantly decrease errors in the calculation of pressure-impulses.

6. **Increase the numerical method efficiency**

   The refinement level required to adequately resolve ventilations demands high computational power, for both the pressure-impulse model and simulations. Considering the pressure-impulse model, the ideal spatial step could not be achieved in some cases. But there are still opportunities for further efficiency enhancements. Examination of the model convergence and relaxation factor may create methods to predict accurate results with substantially fewer iterations. Parallel computing and adaptive grid refinement could also be used to decrease calculation time by large factors.

7. **Sensitivity analysis of air effects in simulations**

   Effects of entrapped air in CFD simulations could be studied through sensitivity analysis. This analysis could involve simulations without air, different air properties and compressibility magnitudes. Material porosities could also interfere on wave impact results. The objective is to verify if the air bounce back effect (Mao (2019), Wood et al. (2000)) could be effectively simulated using CFD and how it influences the distribution of pressure-impulses along the structure, especially in the region near the wave impact.

8. **Investigate other venting configurations**

   In some studies of wave impacts on bridge girders, air relief openings are distributed along both the exposed surface width and length (Azadbakht & Yim (2016), Xiao & Guo (2018)). This configuration could also be applied in overhangs subject to wave loads. This would allow for an increased relative venting area, while keeping the area of each hole constant. In addition, venting positions could be located along the wall height itself and circular hole shapes could be tested.

9. **Application of pressure-impulse theory to design other types of structures**

   Despite all limitations, the pressure-impulse model showed good predictive skill compared to CFD and physical experiments, specially without venting. This robust model could be applied also to evaluate other types of structures subject to wave impacts, such as decks, breakwaters, dikes, bridges, piers and jetties. It could become an additional design standard to effectively assess wave impact impulses with the aim to enhance safety against damage.

Bibliography

Allsop, W., Alderson, J. & Cuomo, G. (2009), Why do suspended deck coastal structures keep failing?, *in* 'Forensic engineering: From failure to understanding', Thomas Telford Publishing, pp. 191–203.

Azadbakht, M. & Yim, S. C. (2016), 'Effect of trapped air on wave forces on coastal bridge superstructures', *Journal of Ocean Engineering and Marine Energy* **2**(2), 139–158.

Bagnold, R. A. (1939), 'Interim report on wave-pressure research.', *Journal of the Institution of Civil Engineers* **12**(7), 202–226.

Broughton, P. & Horn, E. (1987), 'Ekofisk platform 2/4c: Re-analysis due to subsidence.', *Proceedings of the Institution of Civil Engineers* **82**(5), 949–979.

Castellino, M., Sammarco, P., Romano, A., Martinelli, L., Ruol, P., Franco, L. & Girolamo, P. D. (2018), 'Large impulsive forces on recurved parapets under non-breaking waves. a numerical study', *Coastal Engineering* **136**, 1–15.

Chen, X., Hofland, B., Molenaar, W., Capel, A. & Gent, M. R. V. (2019), 'Use of impulses to determine the reaction force of a hydraulic structure with an overhang due to wave impact', *Coastal Engineering* **147**, 75–88.

Cooker, M. J. & Peregrine, D. H. (1995), 'Pressure-impulse theory for liquid impact problems', *Journal of Fluid Mechanics* **297**(-1), 193.

Cuomo, G., Allsop, W., Bruce, T. & Pearson, J. (2010), 'Breaking wave loads at vertical seawalls and breakwaters', *Coastal Engineering* **57**(4), 424–439.

Cuomo, G., Allsop, W. & McConnell, K. (2004), Dynamic wave loads on coastal structures: Analysis of impulsive and pulsating wave loads, *in* 'Coastal Structures 2003', American Society of Civil Engineers.

Cuomo, G., Tirindelli, M. & Allsop, W. (2007), 'Wave-in-deck loads on exposed jetties', *Coastal Engineering* **54**(9), 657–679.

de Almeida, E., Hofland, B. & Jonkman, S. N. (2019), 'Wave impact pressure-impulse on vertical structures with overhangs', *Coastal Structures Conference 2019* .

Elger, D., Williams, B., Crowe, C. & Roberson, J. (2012), *Engineering Fluid Mechanics*, Wiley.

Engsig-Karup, A., Bingham, H. & Lindberg, O. (2009), 'An efficient flexible-order model for 3d nonlinear water waves', *Journal of Computational Physics* **228**(6), 2100–2118.

Gaeta, M. G., Martinelli, L. & Lamberti, A. (2012), 'Uplift forces on wave exposed jetties: Scale comparison and effect of venting', *Coastal Engineering Proceedings* **1**(33), 34.

Gelders Staalstraal- en Schildersbedrijf B.V. (2019), 'Sluiscomplex Terneuzen'.
URL: *https://www.gsb.nl/project/sluiscomplex-terneuzen/*

Ghadirian, A. & Bredmose, H. (2019), 'Pressure impulse theory for a slamming wave on a vertical circular cylinder', *Journal of Fluid Mechanics* **867**.

Goda, Y. (1974), 'New wave pressure formulae for composite breakwaters', *Coastal Engineering Proceedings* **1**(14).

Goda, Y. (2000), *Random Seas and Design of Maritime Structures*, World Scientific.

Hayatdavoodi, M. & Ertekin, R. C. (2016), 'Review of wave loads on coastal bridge decks', *Applied Mechanics Reviews* **68**(3), 030802.

Hirt, C. & Nichols, B. (1981), 'Volume of fluid (VOF) method for the dynamics of free boundaries', *Journal of Computational Physics* **39**(1), 201–225.

Hofland, B., Kaminski, M. & Wolters, G. (2011), 'Large scale wave impacts on a vertical wall', *Coastal Engineering Proceedings* **1**.

Hofland, B., Passos, M. & de Almeida, E. (2019), 'Effect of venting holes to relieve wave impact pressures on flood gates with overhangs', *Coastal Structures 2019* .

Holthuijsen, L. H. (2009), *Waves in Oceanic and Coastal Waters*, Cambridge University Press.

Holzmann, T. (2016), *Mathematics, Numerics, Derivations and OpenFOAM®*, Holzmann CFD.

Hu, Z. Z., Greaves, D. & Raby, A. (2016), 'Numerical wave tank study of extreme waves and wave-structure interaction using OpenFoam®', *Ocean Engineering* **126**, 329–342.

Huang, M., Kennedy, A., Tomiczek, T. & Westerink, J. (2018), 'Solitary wave impacts on vertical and overhanging near-coast structures', *Coastal Engineering Journal* **60**(3), 356–370.

Hull, P. & Müller, G. (2002), 'An investigation of breaker heights, shapes and pressures', *Ocean Engineering* **29**(1), 59–79.

Jacobsen, N. G., Fuhrman, D. R. & Fredsøe, J. (2011), 'A wave generation toolbox for the open-source CFD library: OpenFoam®', *International Journal for Numerical Methods in Fluids* **70**(9), 1073–1088.

Jongman, B., Ward, P. J. & Aerts, J. C. (2012), 'Global exposure to river and coastal flooding: Long term trends and changes', *Global Environmental Change* **22**(4), 823–835.

Kaplan, P. (1992), Wave impact forces on offshore structures: Re-examination and new interpretations, *in* 'Offshore Technology Conference', Offshore Technology Conference.

Kirkgöz, M. S. (1991), 'Impact pressure of breaking waves on vertical and sloping walls', *Ocean Engineering* **18**(1-2), 45–59.

Kisacik, D. (2012), Loading conditions due to violent wave impacts on coastal structures with cantilever surfaces, PhD thesis, Ghent University.

Kisacik, D., Troch, P. & Bogaert, P. V. (2012), 'Description of loading conditions due to violent wave impacts on a vertical structure with an overhanging horizontal cantilever slab', *Coastal Engineering* **60**, 201–226.

Kisacik, D., Troch, P., Bogaert, P. V. & Caspeele, R. (2014), 'Investigation of uplift impact forces on a vertical wall with an overhanging horizontal cantilever slab', *Coastal Engineering* **90**, 12–22.

Kortenhaus, A. & Oumeraci, H. (1998), 'Classification of wave loading on monolithic coastal structures', *Coastal Engineering Proceedings* **1**(26).
URL: *https://icce-ojs-tamu.tdl.org/icce/index.php/icce/article/view/5654*

Mao, Y. (2019), Wave loads on vertical structure with overhang considering air influence, Master's thesis, Delft University of Technology.

McConnell, K., Allsop, W. & Cruickshank, I. (2004), *Piers, Jetties and Related Structures Exposed to Waves - Guidelines for Hydraulic Loading*, Thomas Telford Ltd.

Neumann, B., Vafeidis, A. T., Zimmermann, J. & Nicholls, R. J. (2015), 'Future coastal population growth and exposure to sea-level rise and coastal flooding - a global assessment', *PLOS ONE* **10**(3), e0118571.

Nicholls, R. J., Brown, S., Goodwin, P., Wahl, T., Lowe, J., Solan, M., Godbold, J. A., Haigh, I. D., Lincke, D., Hinkel, J., Wolff, C. & Merkens, J.-L. (2018), 'Stabilization of global temperature at 1.5°c and 2.0°c: implications for coastal areas', *Philosophical Transactions of the Royal Society A: Mathematical, Physical and Engineering Sciences* **376**(2119), 20160448.

Onabid, M. A. (2012), 'Solving three-dimensional (3D) Laplace equations by successive over-relaxation method', *African Journal of Mathematics and Computer Science Research* **5**(13), 204–208.

Oumeraci, H. (1994), 'Review and analysis of vertical breakwater failures — lessons learned', *Coastal Engineering* **22**(1-2), 3–29.

Oumeraci, H., Allsop, W., B. De Groot, M., S. Crouch, R. & Vrijling, J. (2001), *Proverbs: Probabilistic Design Tools for Vertical Breakwaters*, CRC Press.

Oumeraci, H., Klammer, P. & Partenscky, H. W. (1993), 'Classification of breaking wave loads on vertical structures', *Journal of Waterway, Port, Coastal, and Ocean Engineering* **119**(4), 381–397.

Partenscky, H.-W. (1989), Dynamic forces due to waves breaking at vertical coastal structures, *in* 'Coastal Engineering 1988', American Society of Civil Engineers.

Renzi, E., Wei, Y. & Dias, F. (2018), 'The pressure impulse of wave slamming on an oscillating wave energy converter', *Journal of Fluids and Structures* **82**, 258–271.

Rijkswaterstaat (2015), Masterplan Beeldkwaliteit Afsluitdijk, Technical report, Paul de Ruiter.

Robertson, I. N., Paczkowski, K., Riggs, H. R. & Mohamed, A. (2013), 'Experimental investigation of tsunami bore forces on vertical walls', *Journal of Offshore Mechanics and Arctic Engineering* **135**(2), 021601.

Robertson, I. N., Riggs, H. R., Yim, S. C. & Young, Y. L. (2007), 'Lessons from hurricane katrina storm surge on bridges and buildings', *Journal of Waterway, Port, Coastal, and Ocean Engineering* **133**(6), 463–483.

Rundgren, L. (1958), *Water wave forces: a theoretical and laboratory study*, Bulletin of the Division of Hydraulics at the Royal Institute of Technology, Stockholm, Sweden, Kungl. Tekniska Högskolan.

Sainflou, M. (1928), 'Essai sur les digues maritimes verticales', *Annales des Ponts et Chaussees* .

Schiereck, G. J. (1996), *Introduction to bed, bank and shore protection*, TU Delft, Department Hydraulic Engineering.

Seiffert, B. R., Ertekin, R. C. & Robertson, I. N. (2015), 'Wave loads on a coastal bridge deck and the role of entrapped air', *Applied Ocean Research* **53**, 91–106.

Shih, R. W. K. & Anastasiou, K. (1992), 'A laboratory study of the wave-induced vertical loading on platform decks.', *Proceedings of the ICE - Water Maritime and Energy* **96**(1), 19–33.

Sobey, R. J. (2009), 'Analytical solutions for steep standing waves', *Proceedings of the Institution of Civil Engineers - Engineering and Computational Mechanics* **162**(4), 185–197.

Stevenson, T. (1874), *The Design and Construction of Harbours*, Cambridge University Press.

Tadjbakhsh, I. & Keller, J. B. (1960), 'Standing surface waves of finite amplitude', *Journal of Fluid Mechanics* **8**(03), 442.

Takahashi, S. & Hosoyamada, S., eds (1994), *Hydrodynamic characteristics of sloping top caissons*, Proceedings of International Conference on HydroTechnical Engineering for Port and Harbor Construction, Port and Harbour Research Institute: Tokyo.

Takahashi, S., Tanimoto, K. & Miyanaga, S. (1985), 'Uplift wave forces due to compression of enclosed air layer and their similitude law', *Coastal Engineering in Japan* **28**(1), 191–206.

van der Meer, J. W., Allsop, N. H., Bruce, T., Rouck, J. D., Kortenhaus, A., Pullen, T., Schüttrumpf, H., Troch, P. & Zanuttigh, B. (2018), 'Manual on wave overtopping of sea defences and related structures', *Manual EurOtop* .

Walkden, M., Wood, D., Bruce, T. & Peregrine, D. (2001), 'Impulsive seaward loads induced by wave overtopping on caisson breakwaters', *Coastal Engineering* **42**(3), 257–276.

Wilde, P., Szmidt, K. & Sobierajski, E. (1998), 'Phenomena in standing wave impact on a horizontal plate', *Coastal Engineering Proceedings* **1**(26).
URL: *https://icce-ojs-tamu.tdl.org/icce/index.php/icce/article/view/5700*

Wood, D. J. (1997), Pressure-impulse impact problems and plunging wave jet impact, PhD thesis, The University of Bristol.

Wood, D. J., Peregrine, D. H. & Bruce, T. (2000), 'Wave Impact on a Wall Using Pressure-Impulse Theory. I: Trapped Air', *Journal of Waterway, Port, Coastal, and Ocean Engineering* **126**(4), 182–190.

Wood, D. & Peregrine, D. (1996), Wave impact beneath a horizontal surface, *in* 'Coastal Engineering 1996', American Society of Civil Engineers.

Wood, D. & Peregrine, D. (1998), 'Two and three-dimensional pressure-impulse models of wave impact on structures', *Coastal Engineering Proceedings* **1**(26).
URL: *https://journals.tdl.org/icce/index.php/icce/article/view/5701*

Xiao, S. & Guo, A. (2018), 'Effects of air relief openings on the mitigation of solitary wave forces on bridge decks', *Journal of Hydrodynamics* **31**(3), 594–602.

List of Figures

List of Tables

A

Parametric analysis results

Variation of geometric parameters

Table A.1: Maximum pressure-impulse and total impulse at wall as a function of wall height.

L_y	P_{max}	I	L_y	P_{max}	I	L_y	P_{max}	I
0.2	2.55	0.51	1.8	1.06	1.08	3.4	1.02	1.35
0.3	2.13	0.62	1.9	1.05	1.10	3.5	1.02	1.37
0.4	1.79	0.67	2.0	1.05	1.12	3.6	1.02	1.38
0.5	1.57	0.70	2.1	1.05	1.14	3.7	1.01	1.39
0.6	1.43	0.74	2.2	1.04	1.16	3.8	1.01	1.41
0.7	1.33	0.77	2.3	1.04	1.18	3.9	1.01	1.42
0.8	1.27	0.81	2.4	1.03	1.20	4.0	1.01	1.43
0.9	1.22	0.84	2.5	1.03	1.22	4.1	1.01	1.44
1.0	1.18	0.87	2.6	1.03	1.23	4.2	1.01	1.45
1.1	1.15	0.90	2.7	1.03	1.25	4.3	1.01	1.46
1.2	1.13	0.93	2.8	1.03	1.27	4.4	1.01	1.48
1.3	1.11	0.96	2.9	1.02	1.28	4.5	1.01	1.49
1.4	1.10	0.98	3.0	1.02	1.30	4.6	1.01	1.50
1.5	1.09	1.01	3.1	1.02	1.31	4.7	1.01	1.51
1.6	1.08	1.03	3.2	1.02	1.33	4.8	1.01	1.52
1.7	1.07	1.06	3.3	1.02	1.34	4.9	1.01	1.53
						5.0	1.01	1.54

Variation of ventilation parameters

Table A.2: Maximum pressure-impulse and total impulse at wall as a function of the venting geometry for $L_y = 1.0$, $P_{max,0} = 1.18$ and $I_0 = 0.87$.

S	L_h	W_h	A_h	P_{max}	R_P	I	R_I
1.00	0.10	0.10	0.01	0.94	20%	0.68	22%
1.00	0.10	0.30	0.03	0.63	47%	0.46	47%
1.00	0.10	0.50	0.05	0.35	71%	0.31	65%
1.00	0.30	0.10	0.03	0.71	40%	0.49	44%
1.00	0.30	0.30	0.09	0.37	69%	0.25	72%
1.00	0.30	0.50	0.15	0.16	87%	0.13	86%
1.00	0.50	0.10	0.05	0.60	49%	0.39	55%
1.00	0.50	0.30	0.15	0.28	76%	0.15	82%
1.00	0.50	0.50	0.25	0.07	94%	0.05	94%
2.00	0.10	0.30	0.03	0.98	17%	0.69	21%
2.00	0.10	0.50	0.05	0.86	27%	0.59	33%
2.00	0.30	0.10	0.03	1.00	16%	0.70	20%
2.00	0.30	0.30	0.09	0.83	30%	0.54	38%
2.00	0.30	0.50	0.15	0.67	43%	0.41	53%
2.00	0.50	0.10	0.05	0.93	21%	0.63	27%
2.00	0.50	0.30	0.15	0.74	37%	0.46	47%
2.00	0.50	0.50	0.25	0.57	52%	0.32	63%
3.00	0.10	0.30	0.03	1.09	8%	0.78	11%
3.00	0.10	0.50	0.05	1.03	13%	0.72	17%
3.00	0.30	0.10	0.03	1.10	7%	0.78	10%
3.00	0.30	0.30	0.09	1.00	15%	0.70	20%
3.00	0.30	0.50	0.15	0.92	22%	0.62	29%
3.00	0.50	0.10	0.05	1.06	10%	0.75	14%
3.00	0.50	0.30	0.15	0.95	19%	0.64	26%
3.00	0.50	0.50	0.25	0.86	27%	0.55	37%
4.00	0.10	0.50	0.05	1.11	6%	0.79	9%
4.00	0.30	0.30	0.09	1.09	8%	0.78	11%
4.00	0.30	0.50	0.15	1.04	12%	0.73	16%
4.00	0.50	0.10	0.05	1.12	5%	0.81	7%
4.00	0.50	0.30	0.15	1.06	10%	0.75	14%
4.00	0.50	0.50	0.25	1.01	15%	0.69	21%
5.00	0.10	0.50	0.05	1.15	3%	0.83	5%
5.00	0.30	0.30	0.09	1.14	4%	0.82	6%
5.00	0.30	0.50	0.15	1.11	6%	0.80	9%
5.00	0.50	0.10	0.05	1.15	2%	0.84	4%
5.00	0.50	0.30	0.15	1.12	5%	0.80	8%
5.00	0.50	0.50	0.25	1.09	8%	0.77	11%
6.00	0.30	0.30	0.09	1.16	2%	0.85	3%
6.00	0.30	0.50	0.15	1.15	3%	0.83	4%
6.00	0.50	0.30	0.15	1.15	3%	0.84	4%
6.00	0.50	0.50	0.25	1.13	4%	0.82	6%

Table A.3: Maximum pressure-impulse and total impulse at wall as a function of the venting geometry for $L_y = 2.0$, $P_{max,0} = 1.05$ and $I_0 = 1.12$.

S	L_h	W_h	A_h	P_{max}	R_P	I	R_I
1.00	0.10	0.10	0.01	0.86	19%	0.90	20%
1.00	0.10	0.30	0.03	0.58	44%	0.64	43%
1.00	0.10	0.50	0.05	0.30	71%	0.47	58%
1.00	0.30	0.10	0.03	0.67	37%	0.67	40%
1.00	0.30	0.30	0.09	0.35	66%	0.36	68%
1.00	0.30	0.50	0.15	0.13	88%	0.22	81%
1.00	0.50	0.10	0.05	0.57	46%	0.54	52%
1.00	0.50	0.30	0.15	0.27	74%	0.23	80%
1.00	0.50	0.50	0.25	0.06	95%	0.10	91%
2.00	0.10	0.30	0.03	0.90	15%	0.90	20%
2.00	0.10	0.50	0.05	0.80	24%	0.78	31%
2.00	0.30	0.10	0.03	0.91	13%	0.91	19%
2.00	0.30	0.30	0.09	0.77	26%	0.72	36%
2.00	0.30	0.50	0.15	0.63	40%	0.55	51%
2.00	0.50	0.10	0.05	0.86	18%	0.83	26%
2.00	0.50	0.30	0.15	0.70	33%	0.60	46%
2.00	0.50	0.50	0.25	0.55	48%	0.43	62%
3.00	0.10	0.30	0.03	0.98	6%	1.00	11%
3.00	0.10	0.50	0.05	0.94	11%	0.93	17%
3.00	0.30	0.10	0.03	0.99	6%	1.01	10%
3.00	0.30	0.30	0.09	0.92	12%	0.89	21%
3.00	0.30	0.50	0.15	0.85	19%	0.79	30%
3.00	0.50	0.10	0.05	0.96	9%	0.96	15%
3.00	0.50	0.30	0.15	0.88	16%	0.82	27%
3.00	0.50	0.50	0.25	0.80	24%	0.70	38%
4.00	0.10	0.50	0.05	1.00	5%	1.01	10%
4.00	0.30	0.30	0.09	0.98	6%	0.98	12%
4.00	0.30	0.50	0.15	0.95	10%	0.92	18%
4.00	0.50	0.10	0.05	1.00	4%	1.02	9%
4.00	0.50	0.30	0.15	0.96	9%	0.94	17%
4.00	0.50	0.50	0.25	0.92	13%	0.86	23%
5.00	0.10	0.50	0.05	1.02	3%	1.05	6%
5.00	0.30	0.30	0.09	1.01	3%	1.04	8%
5.00	0.30	0.50	0.15	0.99	5%	1.00	11%
5.00	0.50	0.10	0.05	1.03	2%	1.06	5%
5.00	0.50	0.30	0.15	1.00	5%	1.01	10%
5.00	0.50	0.50	0.25	0.97	7%	0.96	15%
6.00	0.30	0.30	0.09	1.03	2%	1.07	5%
6.00	0.30	0.50	0.15	1.02	3%	1.04	7%
6.00	0.50	0.30	0.15	1.02	3%	1.05	6%
6.00	0.50	0.50	0.25	1.01	4%	1.02	9%

Table A.4: Maximum pressure-impulse and total impulse at wall as a function of the venting geometry for $L_y = 3.0$, $P_{max,0} = 1.02$ and $I_0 = 1.30$.

S	L_h	W_h	A_h	P_{max}	R_P	I	R_I
1.00	0.10	0.10	0.01	0.84	18%	1.05	19%
1.00	0.10	0.30	0.03	0.57	44%	0.76	41%
1.00	0.10	0.50	0.05	0.30	71%	0.57	56%
1.00	0.30	0.10	0.03	0.66	36%	0.79	39%
1.00	0.30	0.30	0.09	0.35	66%	0.44	66%
1.00	0.30	0.50	0.15	0.13	88%	0.27	79%
1.00	0.50	0.10	0.05	0.56	45%	0.63	51%
1.00	0.50	0.30	0.15	0.27	73%	0.28	79%
1.00	0.50	0.50	0.25	0.05	95%	0.13	90%
2.00	0.10	0.30	0.03	0.88	14%	1.04	20%
2.00	0.10	0.50	0.05	0.78	23%	0.91	30%
2.00	0.30	0.10	0.03	0.89	13%	1.05	19%
2.00	0.30	0.30	0.09	0.76	25%	0.83	36%
2.00	0.30	0.50	0.15	0.63	39%	0.65	50%
2.00	0.50	0.10	0.05	0.84	17%	0.96	26%
2.00	0.50	0.30	0.15	0.69	32%	0.70	46%
2.00	0.50	0.50	0.25	0.55	46%	0.50	62%
3.00	0.10	0.30	0.03	0.96	6%	1.16	11%
3.00	0.10	0.50	0.05	0.92	10%	1.08	17%

Table A.5: Maximum pressure-impulse and total impulse at wall as a function of the venting geometry for $L_y = 6.0$, $P_{max,0} = 1.00$ and $I_0 = 1.62$.

S	L_h	W_h	A_h	P_{max}	R_P	I	R_I
1.00	0.10	0.10	0.01	0.83	17%	1.33	18%
1.00	0.10	0.30	0.03	0.57	43%	0.98	39%
1.00	0.10	0.50	0.05	0.29	71%	0.76	53%
1.00	0.30	0.10	0.03	0.65	35%	1.01	38%
1.00	0.30	0.30	0.09	0.35	65%	0.58	64%
1.00	0.30	0.50	0.15	0.12	88%	0.39	76%
1.00	0.50	0.10	0.05	0.56	44%	0.81	50%
1.00	0.50	0.30	0.15	0.27	73%	0.38	77%
1.00	0.50	0.50	0.25	0.05	95%	0.19	88%

B

Correlation between parameters

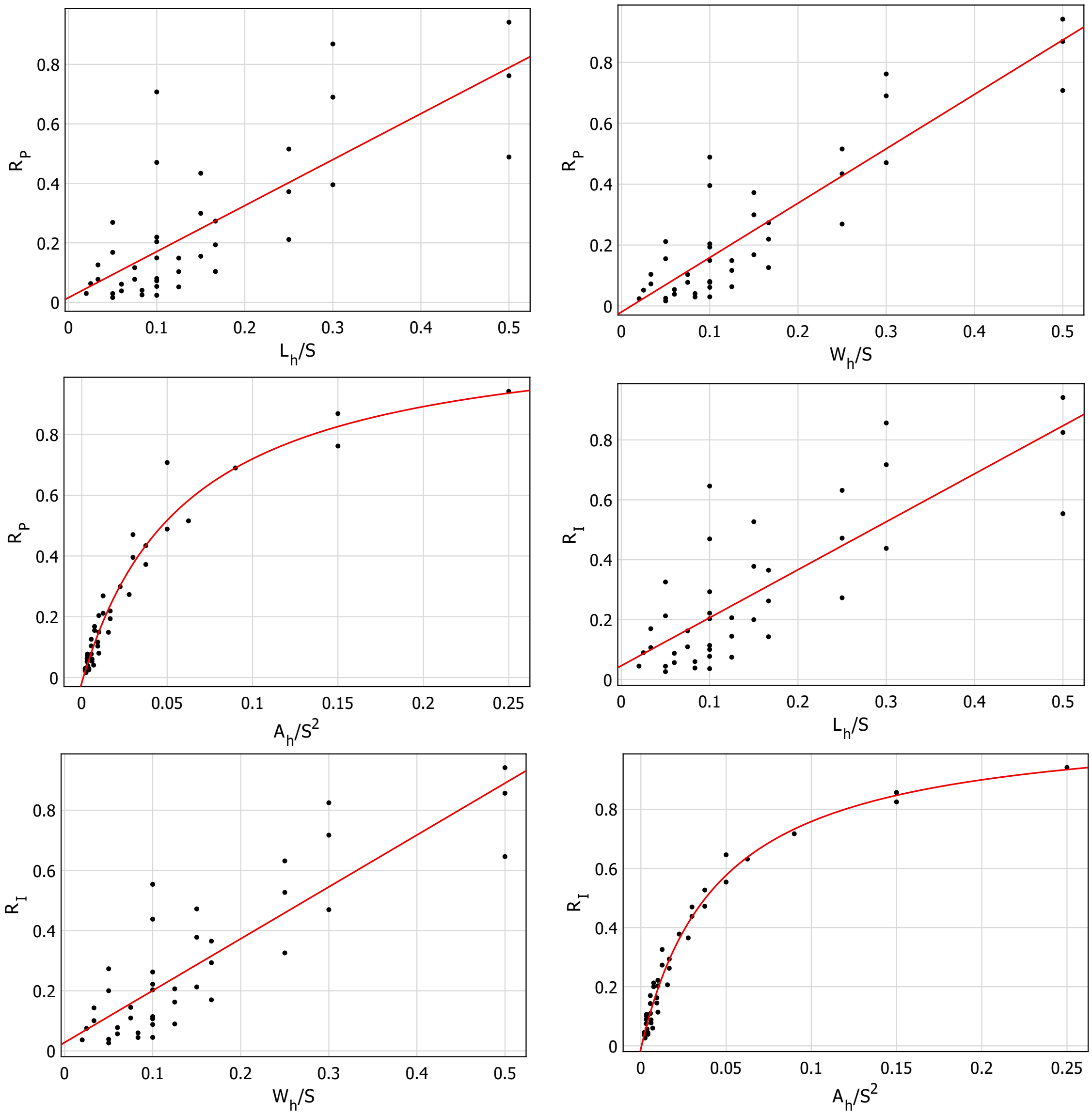

Figure B.1: Correlation between R_P, R_I and ventilation parameters for $L_y = 1.0$.

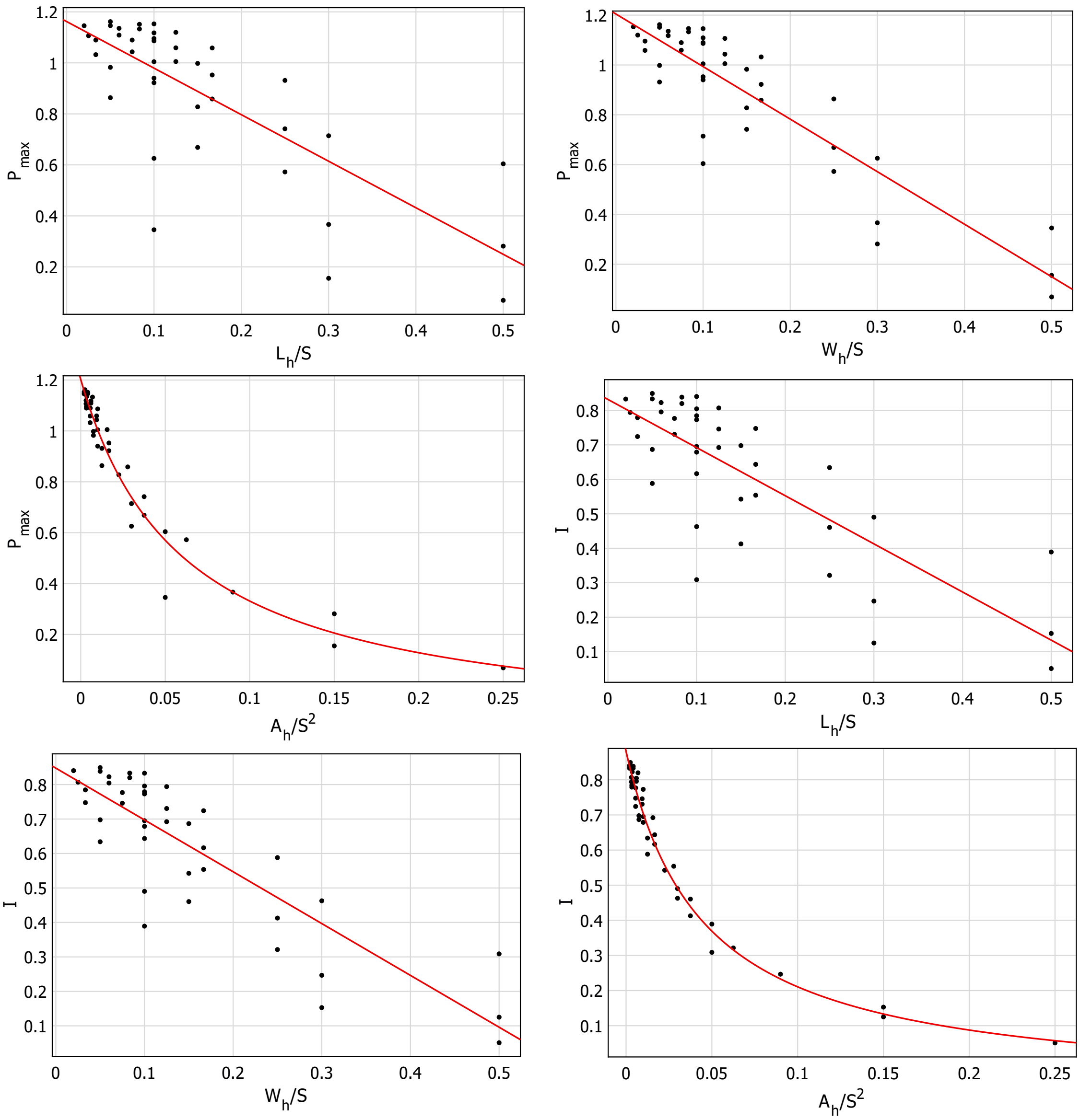

Figure B.2: Correlation between P_{max}, I and ventilation parameters for $L_y = 1.0$.

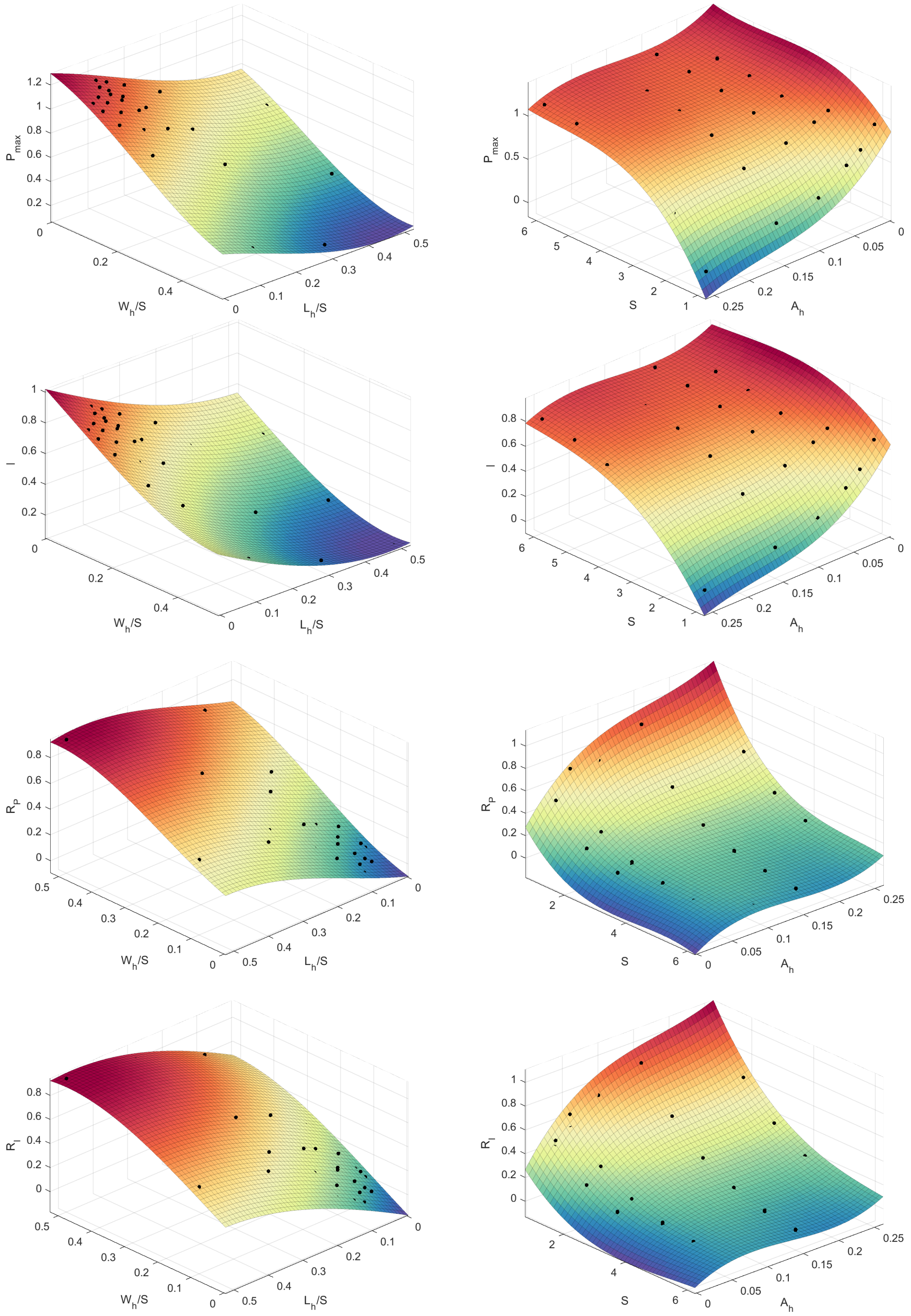

Figure B.3: Surfaces relating P_{max}, I, R_P, R_I and ventilation parameters for $L_y = 1.0$.

C

Surface elevation snapshots

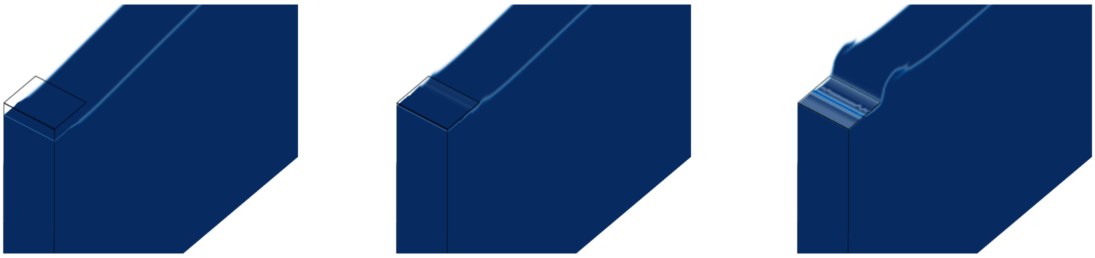

(a) $t = 40.40\ s$ (b) $t = 40.50\ s$ (c) $t = 40.60\ s$

Figure C.1: Surface elevation before (left), during (middle) and after (right) the first impact, for the case of vertical structure with overhang 10 *cm* long and no venting.

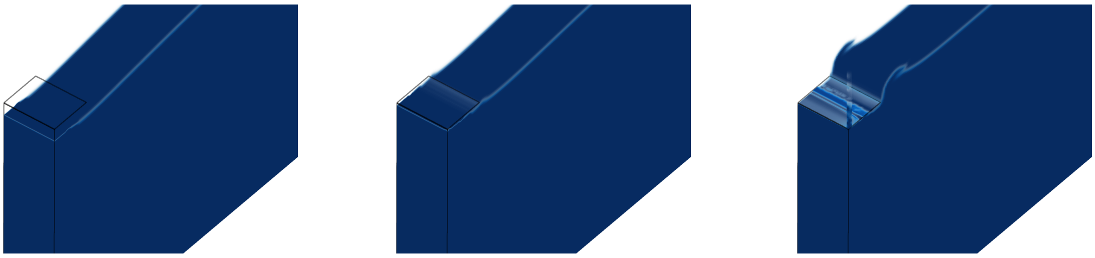

(a) $t = 40.40\ s$ (b) $t = 40.50\ s$ (c) $t = 40.60\ s$

Figure C.2: Surface elevation before (left), during (middle) and after (right) the first impact, for the case of vertical structure with overhang 10 *cm* long and 1 *cm* of venting width.

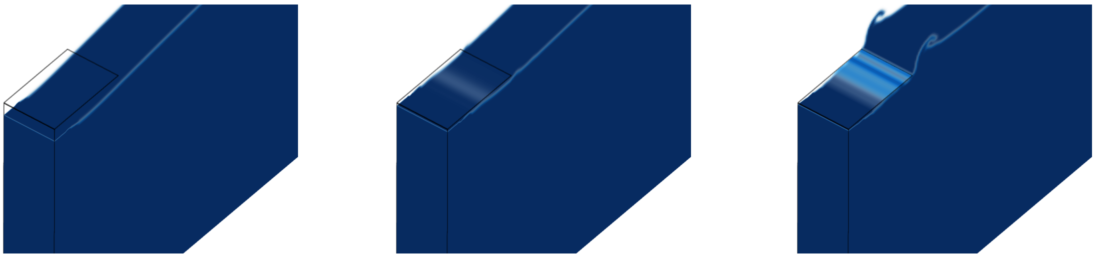

(a) $t = 40.40\ s$ (b) $t = 40.50\ s$ (c) $t = 40.60\ s$

Figure C.3: Surface elevation before (left), during (middle) and after (right) the first impact, for the case of vertical structure with overhang 20 *cm* long and no venting.

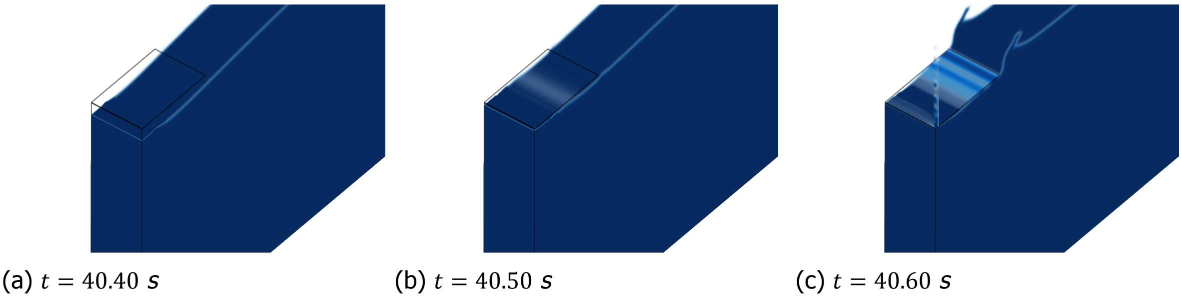

(a) $t = 40.40\ s$ (b) $t = 40.50\ s$ (c) $t = 40.60\ s$

Figure C.4: Surface elevation before (left), during (middle) and after (right) the first impact, for the case of vertical structure with overhang 20 *cm* long and 1 *cm* of venting width.

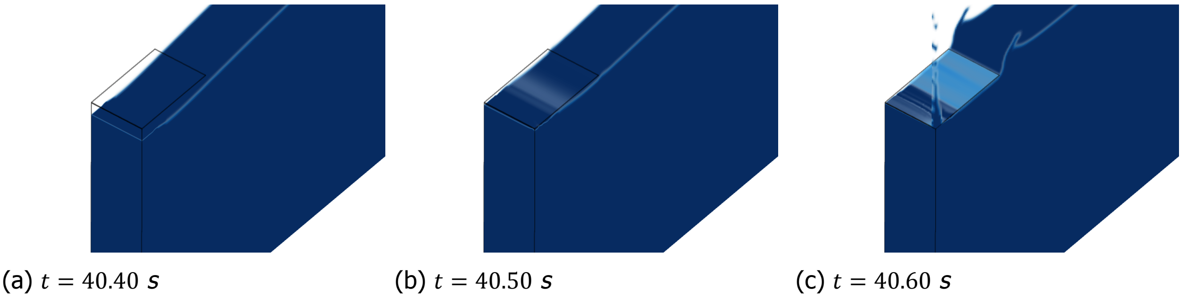

(a) $t = 40.40\ s$ (b) $t = 40.50\ s$ (c) $t = 40.60\ s$

Figure C.5: Surface elevation before (left), during (middle) and after (right) the first impact, for the case of vertical structure with overhang 20 *cm* long and 2 *cm* of venting width.

D

Impact impulse separation

Experimental data

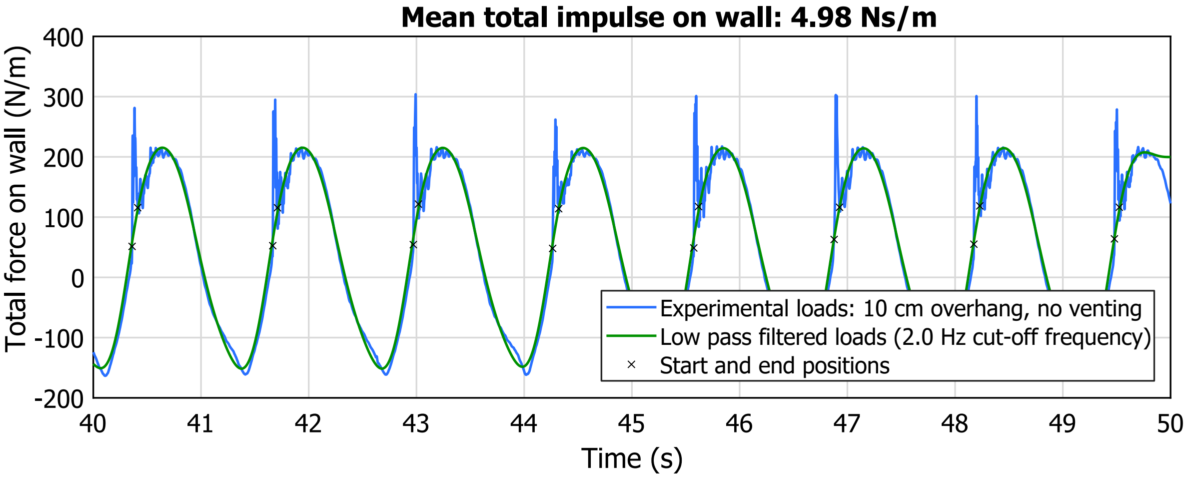

Figure D.1: Derivation of impact impulses using Butterworth filters with 2.0 *Hz* cut-off frequencies for experimental Case 1a, with $L_o = 10$ *cm*, $L_h = W_h = 0$ *cm* and $S = 25$ *cm*.

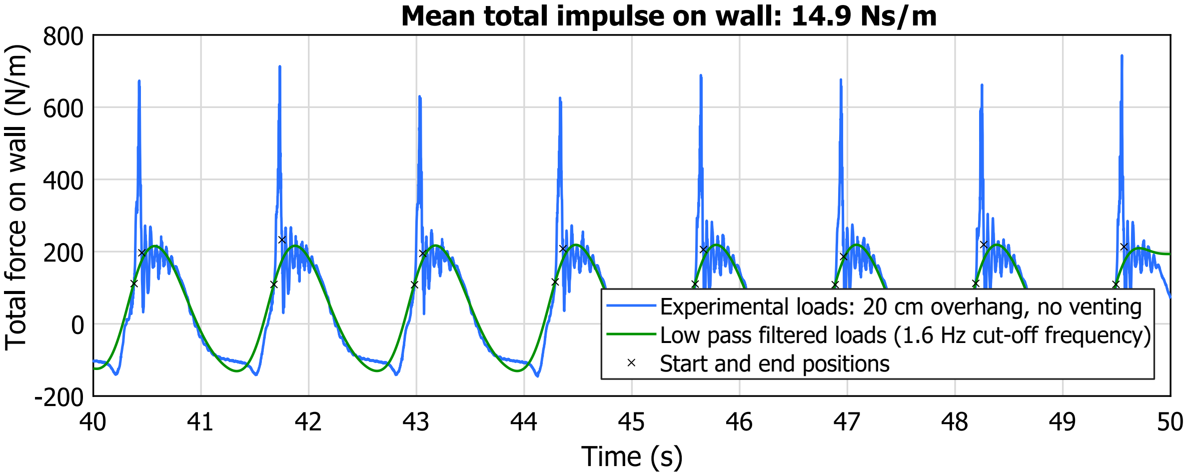

Figure D.2: Derivation of impact impulses using Butterworth filters with 1.6 *Hz* cut-off frequencies for experimental Case 2a, with $L_o = 20$ *cm*, $L_h = W_h = 0$ *cm* and $S = 25$ *cm*.

Simulated data: 8 impacts

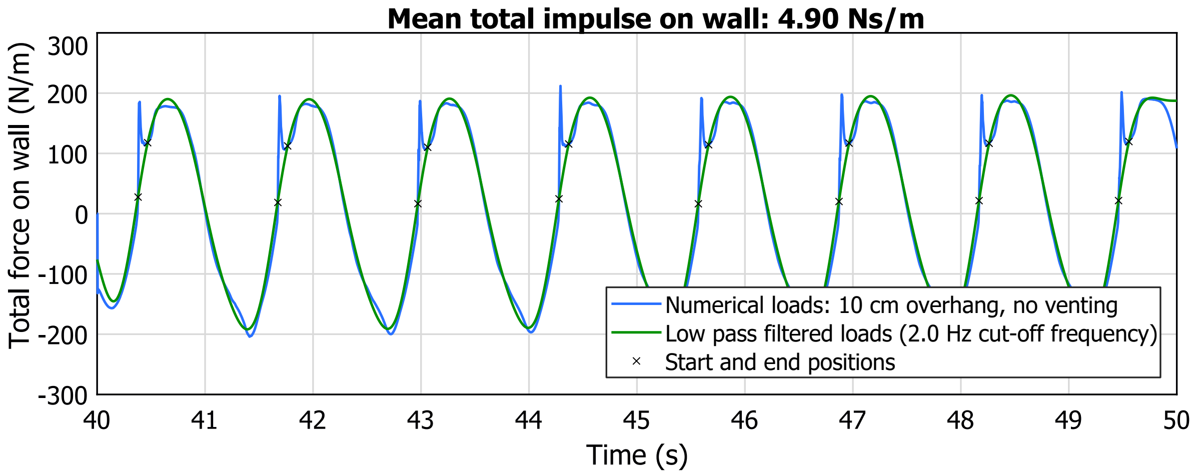

Figure D.3: Derivation of impact impulses using Butterworth filters with 2.0 *Hz* cut-off frequencies for simulated Case 1a, with $L_o = 10$ *cm*, $L_h = W_h = 0$ *cm* and $S = 25$ *cm*.

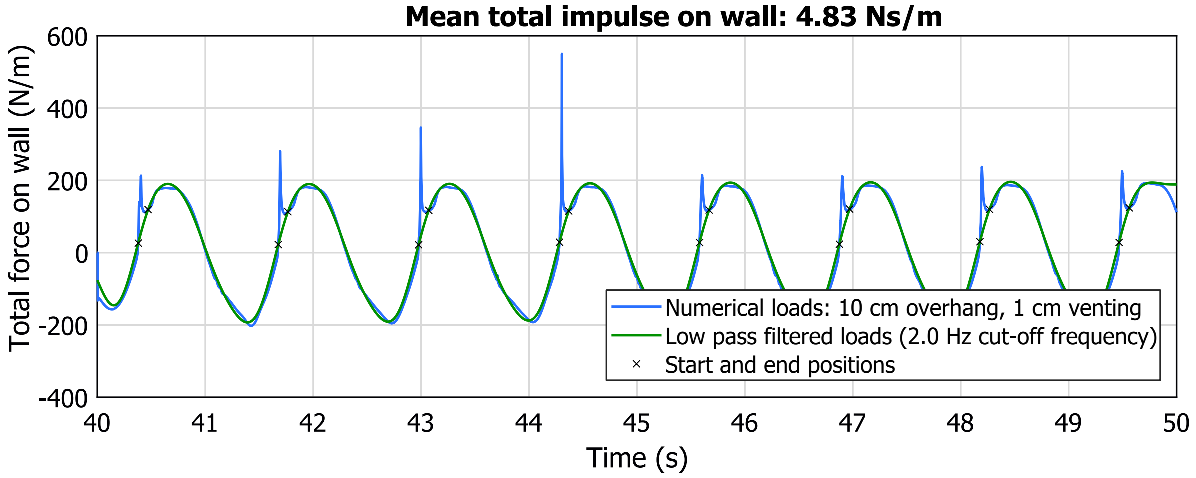

Figure D.4: Derivation of impact impulses using Butterworth filters with 2.0 *Hz* cut-off frequencies for simulated Case 1b, with $L_o = 10$ *cm*, $L_h = W_h = 1$ *cm* (section through hole) and $S = 25$ *cm*.

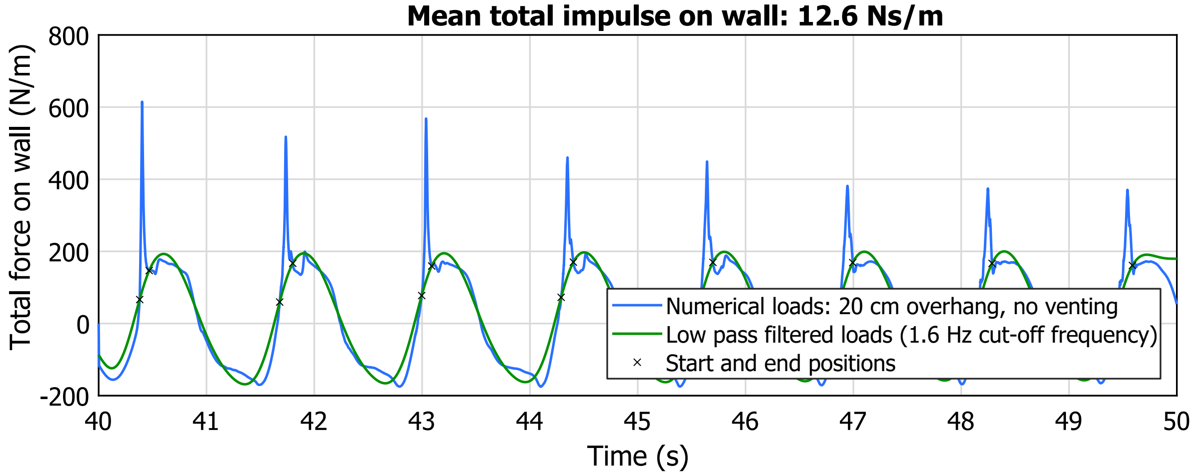

Figure D.5: Derivation of impact impulses using Butterworth filters with 1.6 *Hz* cut-off frequencies for simulated Case 2a, with $L_o = 20$ *cm*, $L_h = W_h = 0$ *cm* and $S = 25$ *cm*.

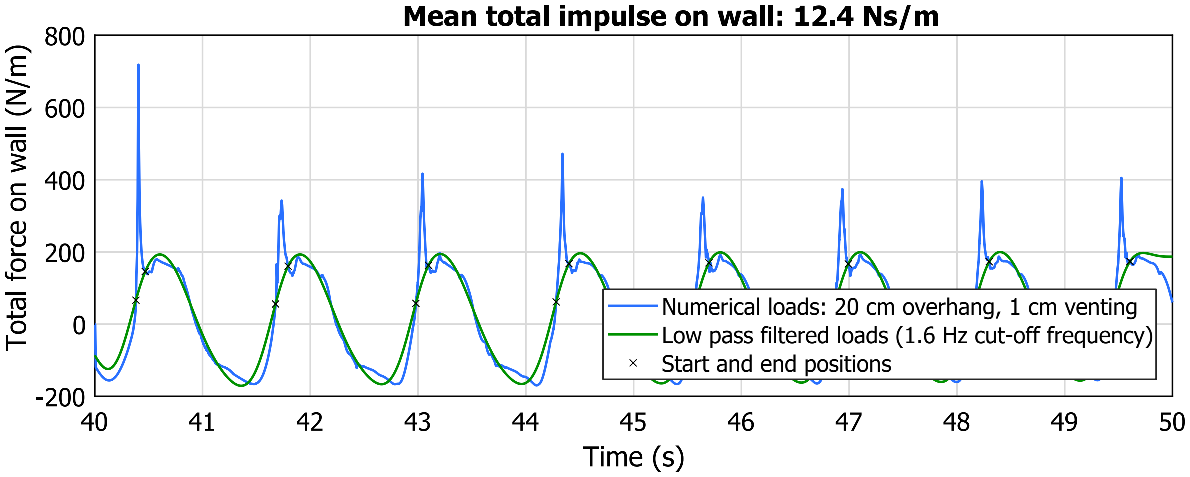

Figure D.6: Derivation of impact impulses using Butterworth filters with 1.6 *Hz* cut-off frequencies for simulated Case 2b, with $L_o = 20$ *cm*, $L_h = W_h = 1$ *cm* (section through hole) and $S = 25$ *cm*.

Simulated data: first impact

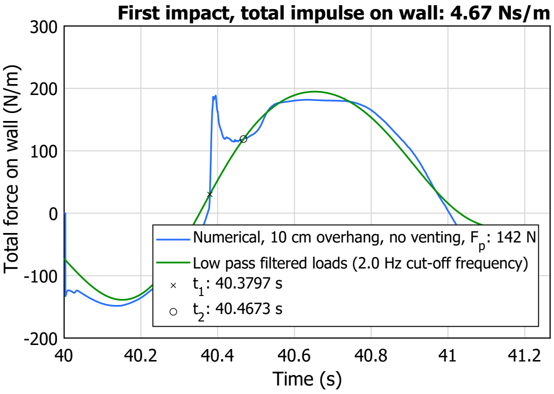

Figure D.7: Total impulses, initial and final impact instants and force peaks for simulated Case 1a.

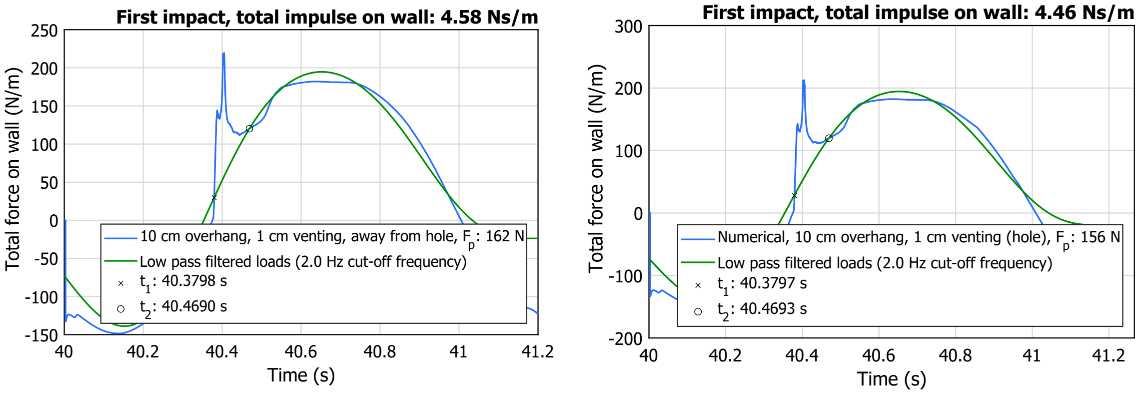

Figure D.8: Total impulses, initial and final impact instants and force peaks for simulated Case 1b, section away from hole (left) and section through hole (right).

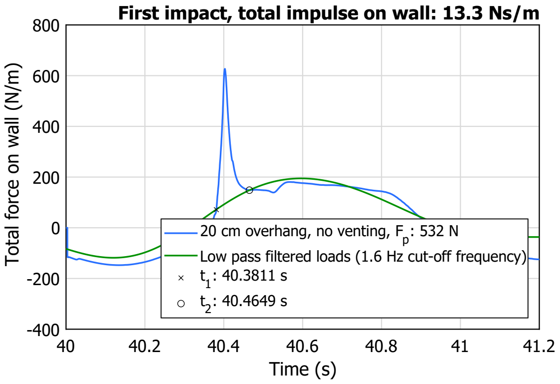

Figure D.9: Total impulses, initial and final impact instants and force peaks for simulated Case 2a.

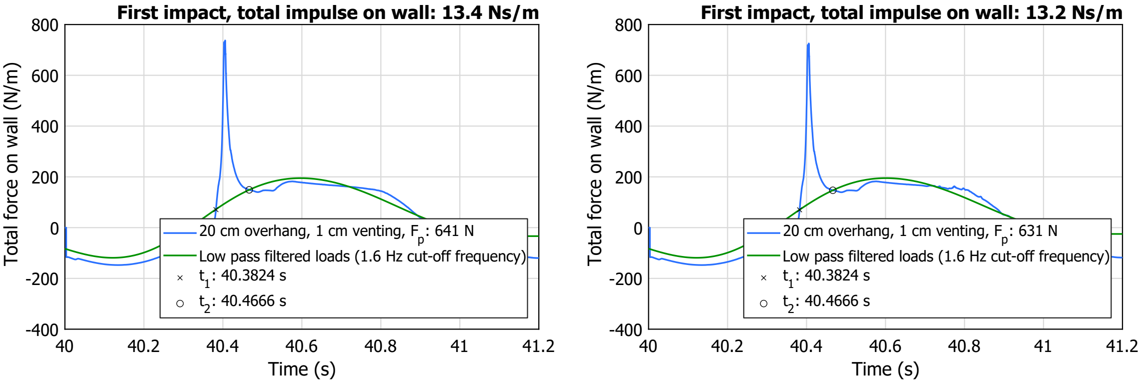

Figure D.10: Total impulses, initial and final impact instants and force peaks for simulated Case 2b, section away from hole (left) and section through hole (right).

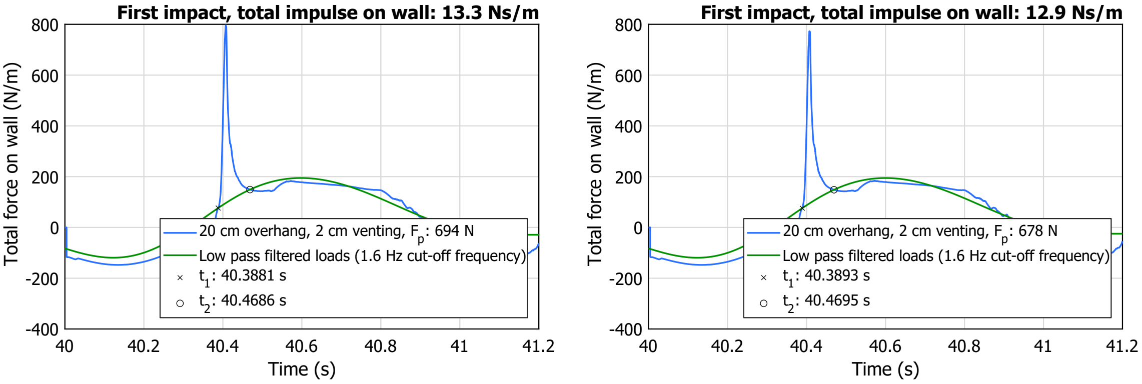

Figure D.11: Total impulses, initial and final impact instants and force peaks for simulated Case 2c, section away from hole (left) and section through hole (right).

E

Velocity fields

Velocity fields at time $t = 40$ s

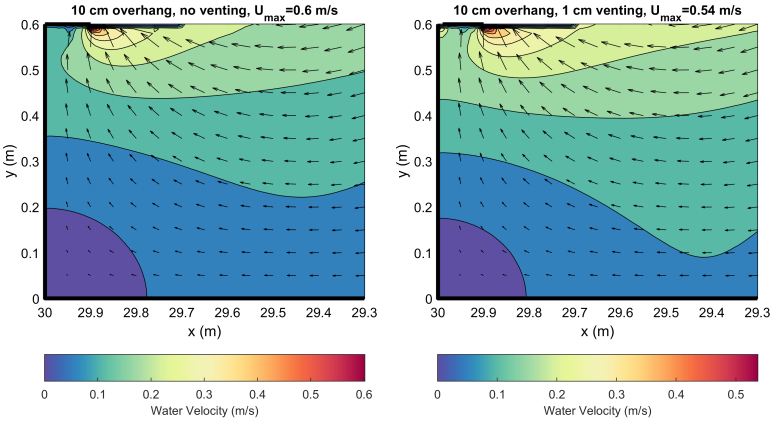

Figure E.1: Side view of velocity fields in Cases 1a (left) and 1b (right).

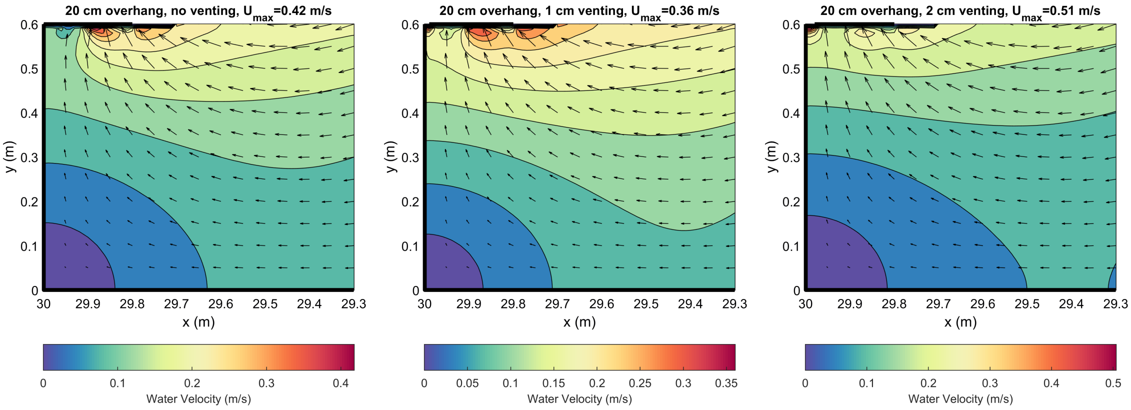

Figure E.2: Side view of velocity fields in Cases 2a (left), 2b (middle) and 2c (right).

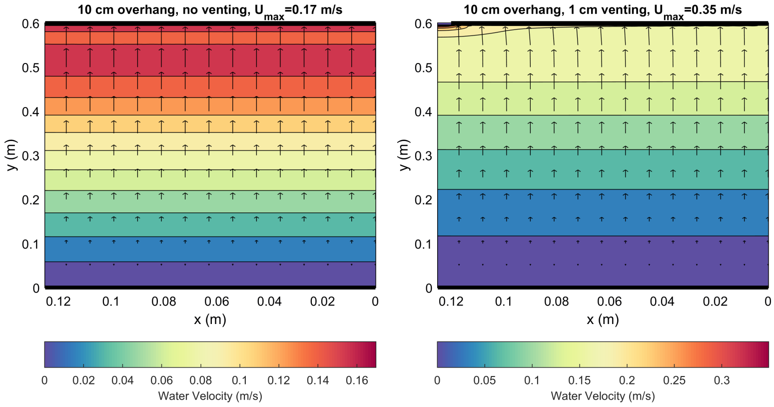

Figure E.3: Front view of velocity fields in Cases 1a (left) and 1b (right).

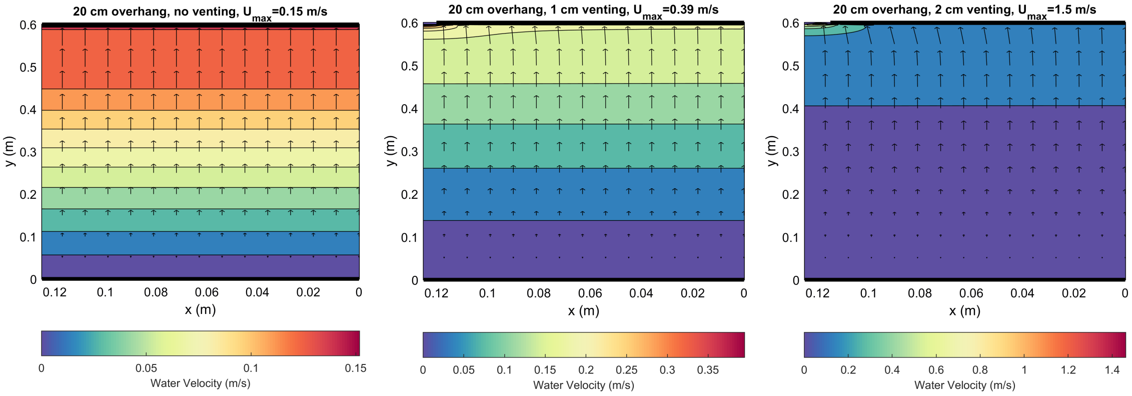

Figure E.4: Front view of velocity fields in Cases 2a (left), 2b (middle) and 2c (right).

F

Vertical impact velocities

Measured velocities

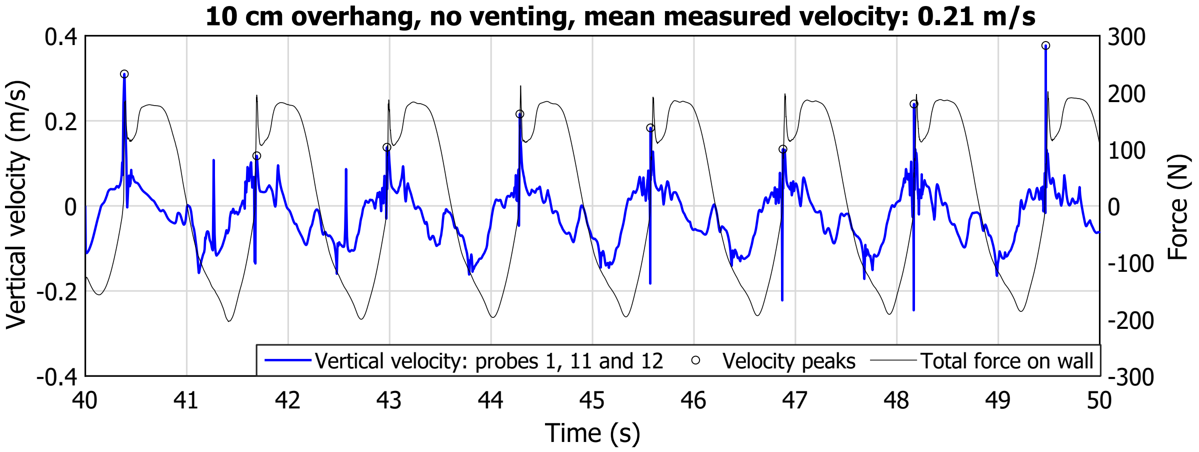

Figure F.1: Measured vertical impact velocity U_M from Probes 1, 11 and 12 (Case 1a).

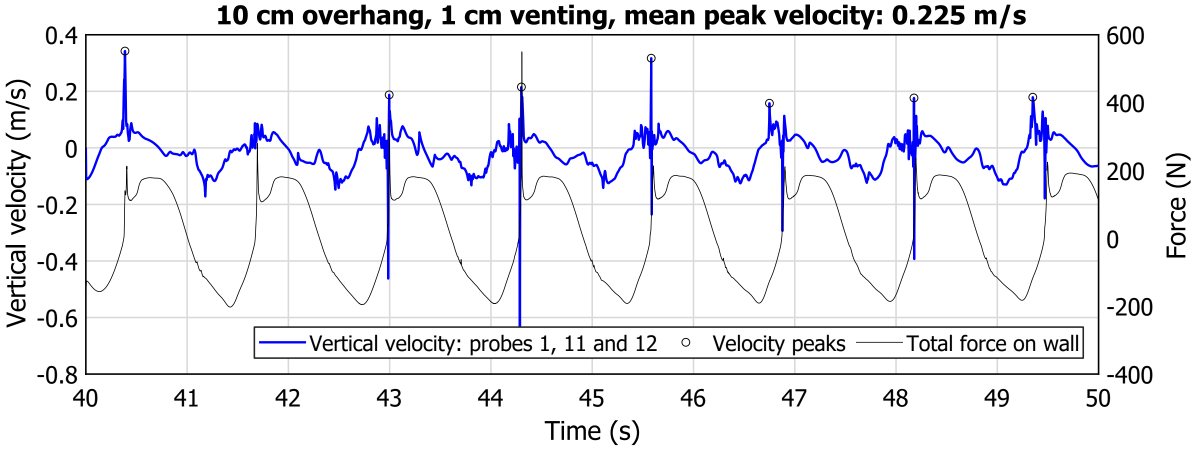

Figure F.2: Measured vertical impact velocity U_M from Probes 1, 11 and 12 (Case 1b).

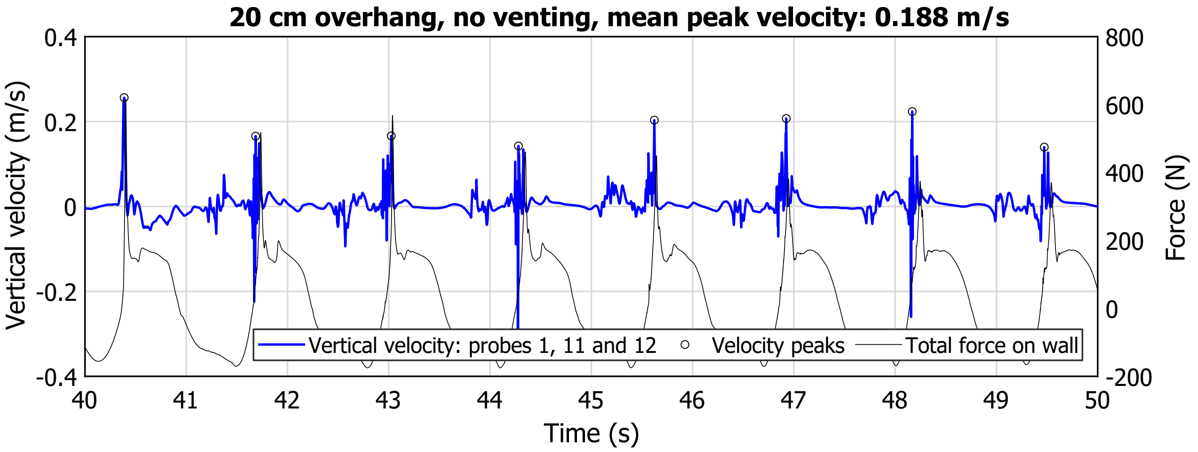

Figure F.3: Measured vertical impact velocity U_M from Probes 1, 11 and 12 (Case 2a).

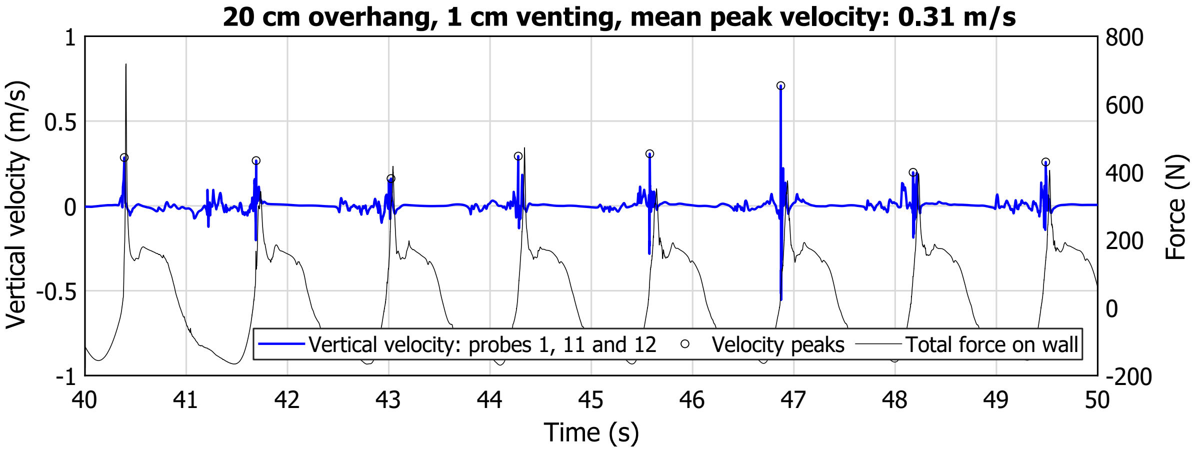

Figure F.4: Measured vertical impact velocity U_M from Probes 1, 11 and 12 (Case 2b).

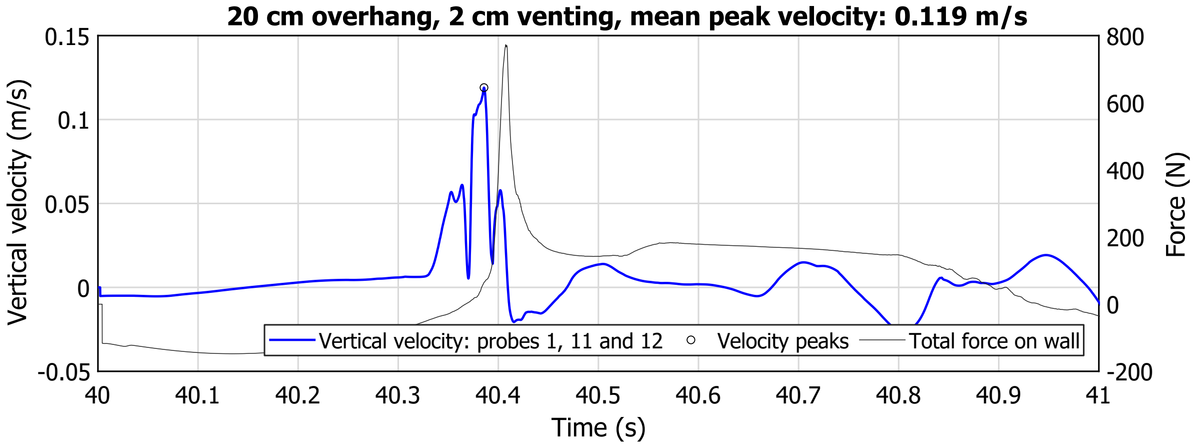

Figure F.5: Measured vertical impact velocity U_M from Probes 1, 11 and 12 (Case 2c).

Derived velocities

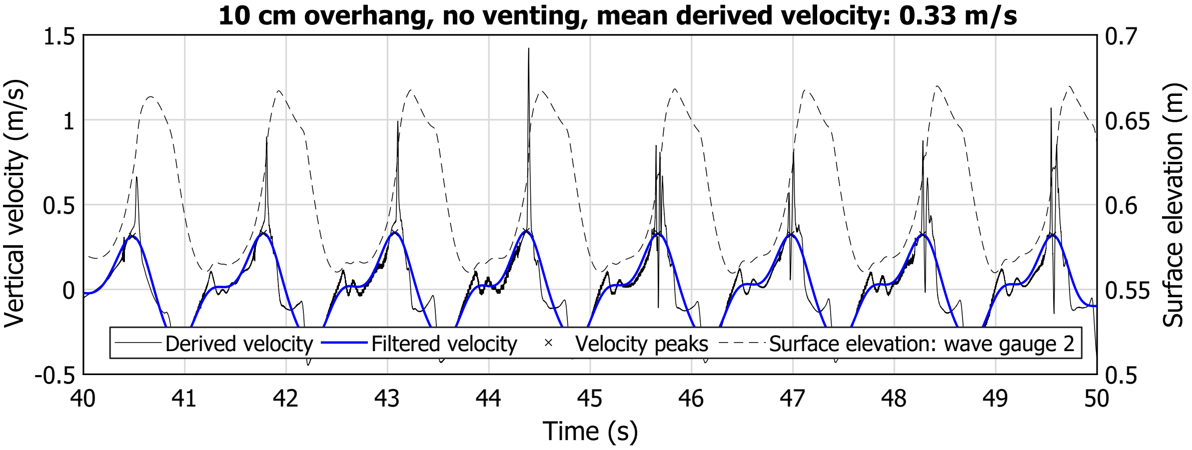

Figure F.6: Derived vertical impact velocity U_D from Wave gauge 2 (Case 1a).

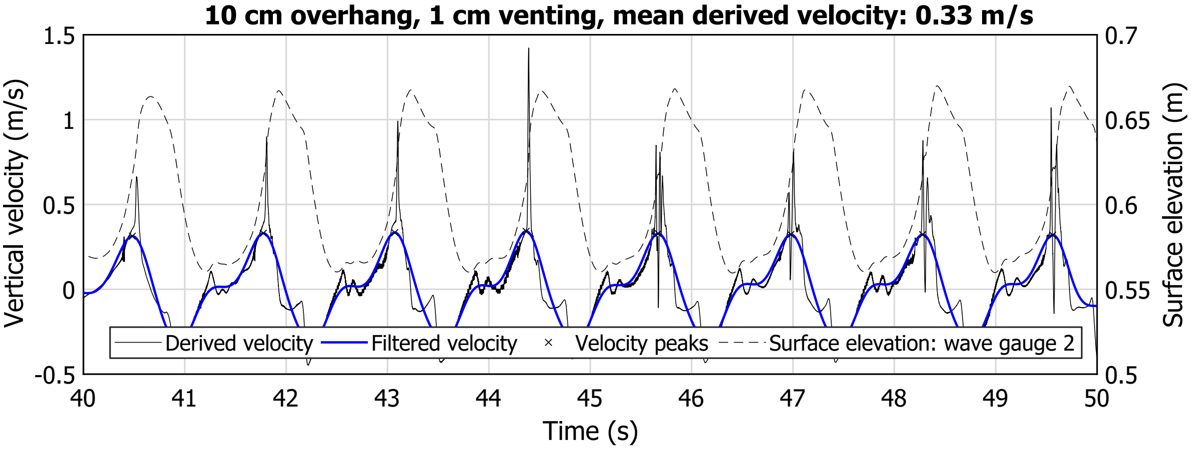

Figure F.7: Derived vertical impact velocity U_D from Wave gauge 2 (Case 1b).

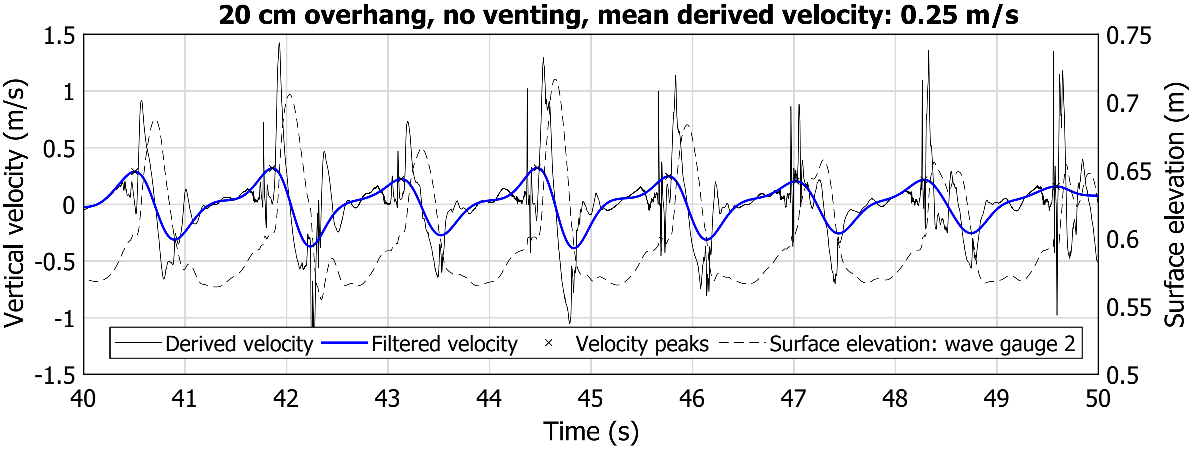

Figure F.8: Derived vertical impact velocity U_D from Wave gauge 2 (Case 2a).

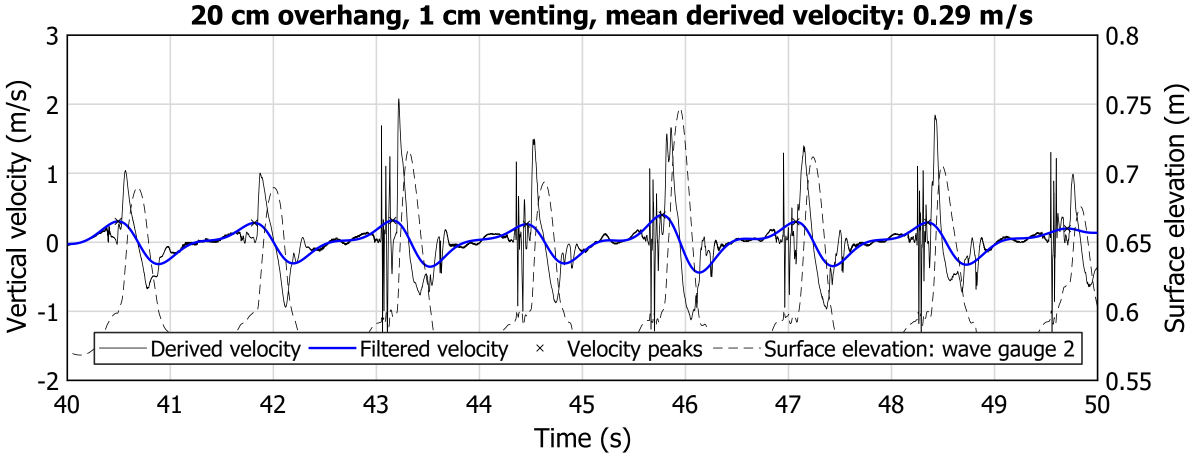

Figure F.9: Derived vertical impact velocity U_D from Wave gauge 2 (Case 2b).

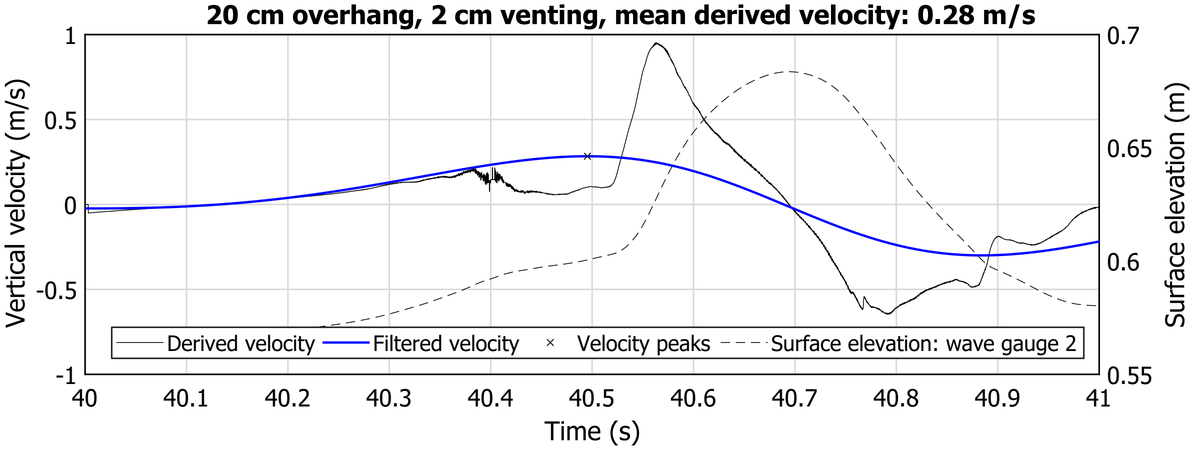

Figure F.10: Derived vertical impact velocity U_D from Wave gauge 2 (Case 2c).

G

Pressure-impulses

Comparison between CFD and pressure-impulse theory: first impact only

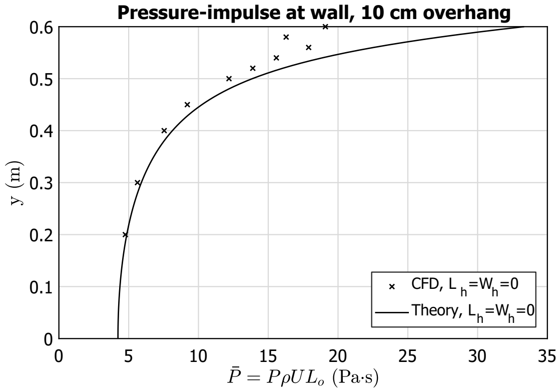

Figure G.1: Validation of simulated and theoretical pressure-impulses along the wall for Case 1a.

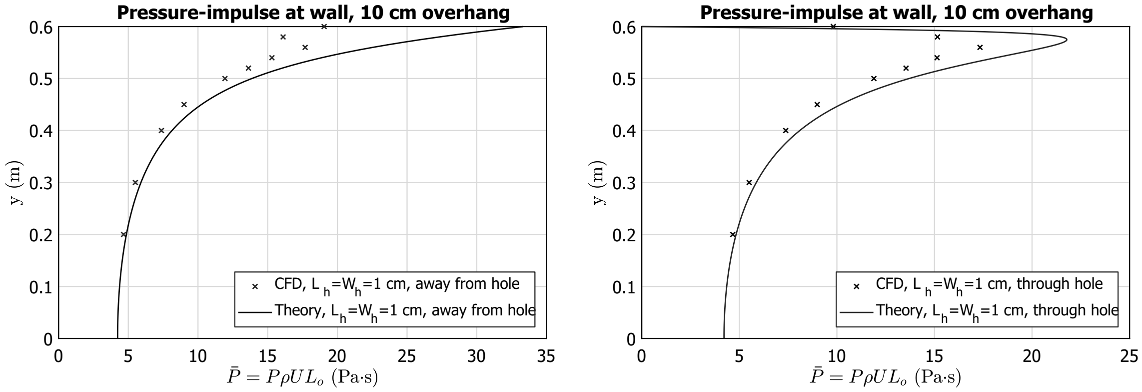

Figure G.2: Validation of simulated and theoretical pressure-impulses along the wall for Case 1b, section away from hole (left) and section through hole (right).

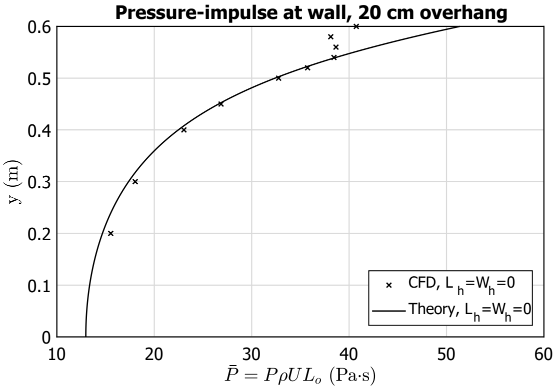

Figure G.3: Validation of simulated and theoretical pressure-impulses along the wall for Case 2a.

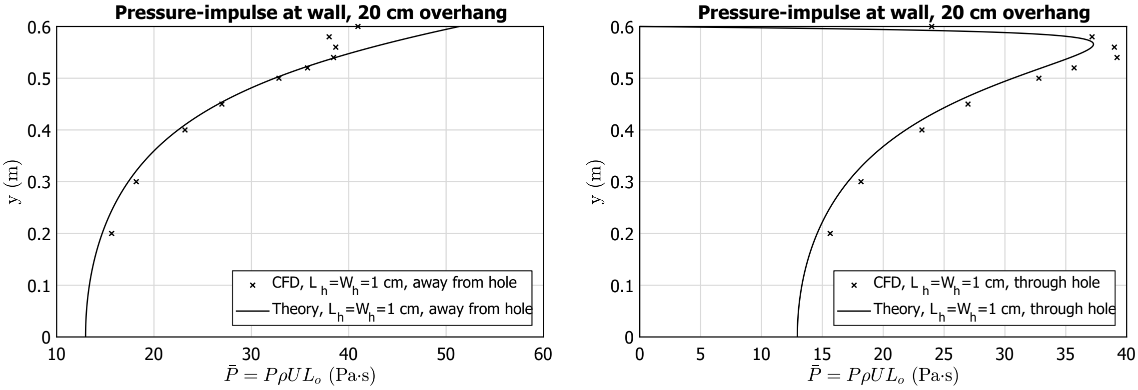

Figure G.4: Validation of simulated and theoretical pressure-impulses along the wall for Case 2b, section away from hole (left) and section through hole (right).

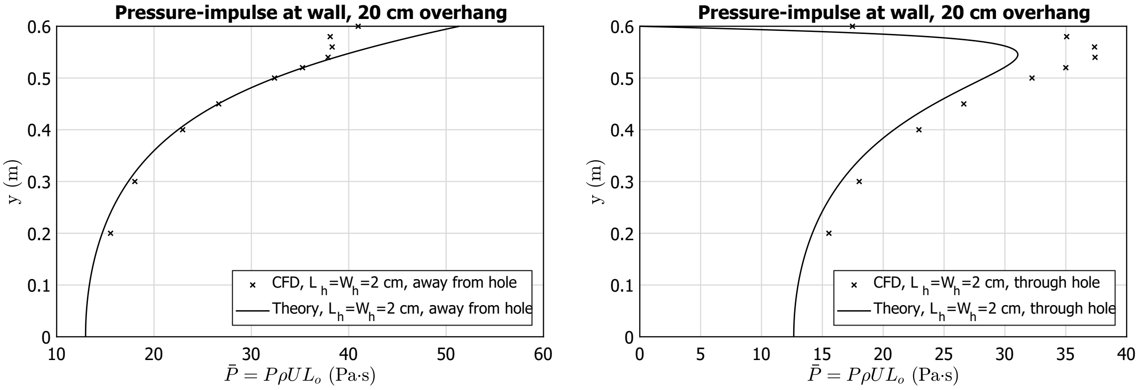

Figure G.5: Validation of simulated and theoretical pressure-impulses along the wall for Case 2c, section away from hole (left) and section through hole (right).

Comparison between CFD and pressure-impulse theory: average of 8 impacts

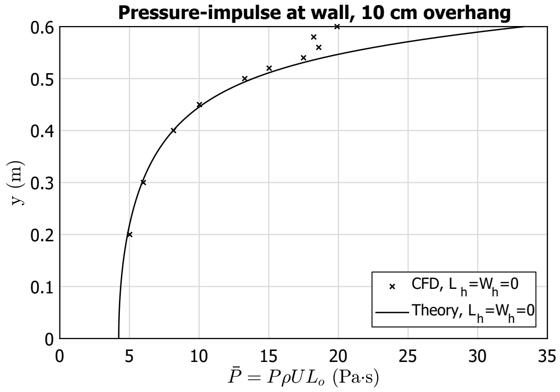

Figure G.6: Validation of simulated and theoretical pressure-impulses along the wall for Case 1a.

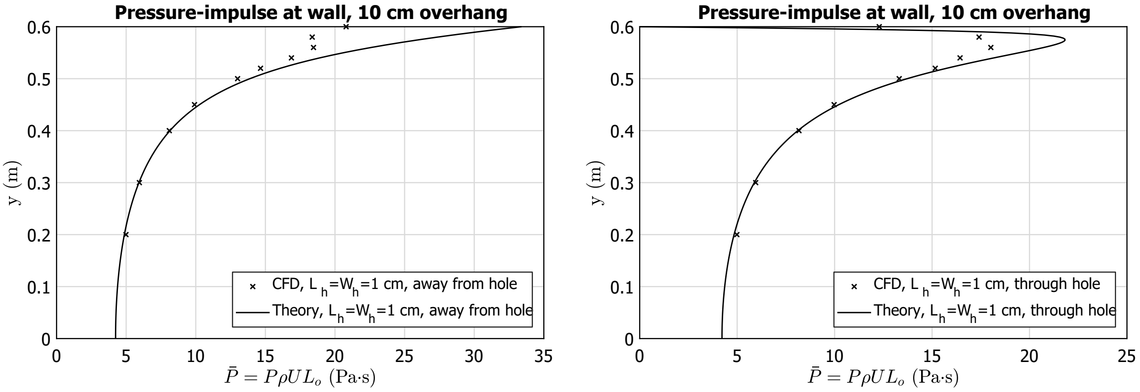

Figure G.7: Validation of simulated and theoretical pressure-impulses along the wall for Case 1b, section away from hole (left) and section through hole (right).

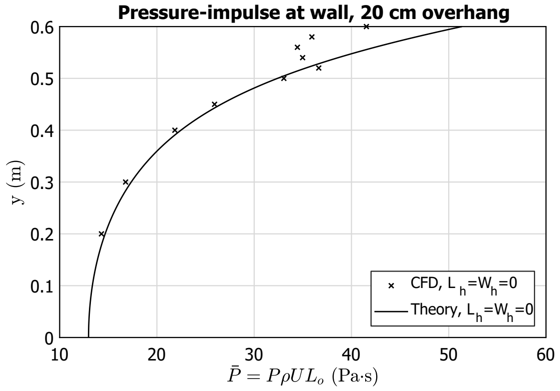

Figure G.8: Validation of simulated and theoretical pressure-impulses along the wall for Case 2a.

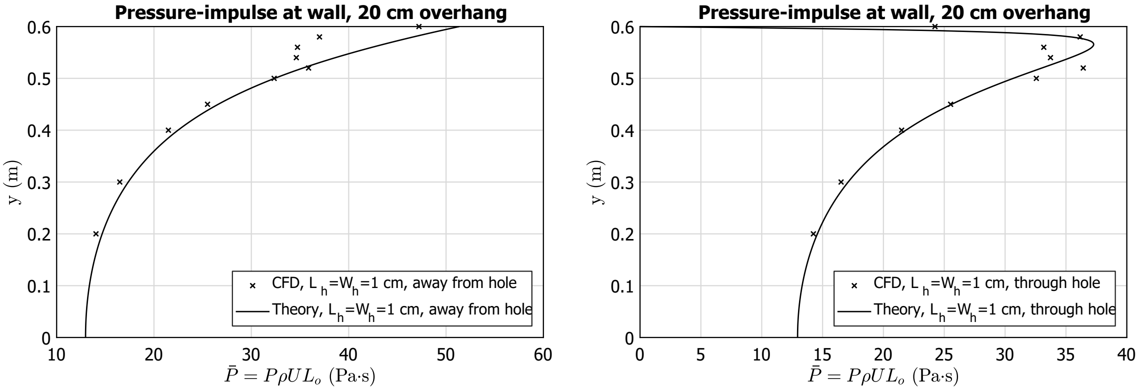

Figure G.9: Validation of simulated and theoretical pressure-impulses along the wall for Case 2b, section away from hole (left) and section through hole (right).